

SURFACE COLOR ESTIMATION OF LARGE SCALE  
DIFFUSE OBJECTS IN AN OUTDOOR ENVIRONMENT

屋外環境下における大規模拡散反射物体の表面色推定

BY

REI KAWAKAMI

A DOCTORAL DISSERTATION

SUBMITTED TO THE GRADUATE SCHOOL OF  
THE UNIVERSITY OF TOKYO



IN PARTIAL FULFILLMENT OF THE REQUIREMENTS  
FOR THE DEGREE OF  
DOCTOR OF INFORMATION SCIENCE AND TECHNOLOGY

DECEMBER 2007



© Copyright by Rei Kawakami 2008  
All Rights Reserved



Committee:

Hiroshi HARASHIMA (Chair)

Mitsuru ISHIZUKA

Kiyoharu AIZAWA

Yoichi SATO

Takeshi NAEMURA

Supervisor:

Katsushi IKEUCHI

## ABSTRACT

Digital three-dimensional models created by computer vision and graphics techniques are becoming widely used for a variety of purposes. Specifically, modeling cultural heritage objects has attracted considerable attention, since such objects are worth preserving, and the data can be utilized for restoration when an object faces the crisis of collapse. Automation for creating 3D models has therefore attracted much interest, since most models are currently created by manual operation, adding significantly to the cost.

Creating an accurate model of an object requires knowledge of the object's shape and surface reflectance. Acquiring shape information is facilitated by the development of sensors and the progress of data processing algorithms, but acquiring surface reflectance properties remains a challenge, specifically with outdoor objects.

This paper targets large-scale objects such as architectural structures in an outdoor environment. The size of target objects may be as much as  $100\text{ m} \times 100\text{ m} \times 50\text{ m}$ . Measuring the surface properties of such huge objects is a challenge. The appearance of an object can be modeled by mapping image textures to the known shape of the object. However, to achieve consistent colors among image textures, the effect of illumination has to be removed before mapping these textures by using surface color estimation and surface reflectance estimation techniques.

Two methods that calculate a surface color by a pixel-based operation are presented. Most previous methods assume uniform illumination in a scene, but this is not always true in images with shadows or with curved objects. The proposed methods enable pixel-based operation by utilizing illumination change. Two models of illumination colors that we introduce enable a surface color to be uniquely determined from two pixel values. First, the paper proposes a method that uses blackbody radiation and analyzes the stability and practicality of the method. Then, a more practical method is proposed that can perform robust estimation using a statistical model derived from outdoor illumination data. Robust estimation is achieved by introducing the plausible range of outdoor illumination colors.

In practical situation, surface reflectance would be required for relighting purposes. A method is presented to estimate surface reflectance from spherical images with known shape information. Spherical images have nearly a 360-degree field of view; they capture target objects and surrounding illumination at one shot. Therefore they do not require specific apparatus or calibration of exposure times, apertures, and camera gain factors. Furthermore, geometric calibration between an image and shape information

becomes robust owing to the characteristic of a spherical camera. Measurement and data-processing cost will be decreased by the method compared to previous methods that need elaborate procedures. This is critical specifically for large-scale objects.

The main contribution of this thesis is that the author has proposed three methods that estimate surface properties of an object. It can be summarized by the three following points: First, the research provides insights into the stability and practicality of pixel-based surface color estimation. Second, a pixel-based method for surface color estimation has been developed that is robust and accurate even for real outdoor objects. None of the conventional methods can perform a pixel-based operation with higher accuracy than the proposed method. Third, an efficient method has been developed that estimates surface reflectance of large-scale objects under outdoor environment. The proposed techniques form the foundation for developing a system that models the appearance of a large-scale object in an outdoor environment.

## 論文要旨

近年、コンピュータグラフィクスによるコンテンツは産業、文化、教育、エンタテインメントの多分野にわたり、至る所で利用されている。とりわけ、文化財のモデル化が注目を集めている。文化財はそれ自身が高価で、データを保存することに価値がある上、崩壊の危機にある場合、修復に役立てられる。現在、モデルの作成は人手により行われており、効率の低下を招いている。この自動化が可能となれば、大きな経費削減が図れる。そこで、物体の三次元モデル化技術への期待が高まっている。

実物体を計算機上で完全に再現するには、物体の幾何情報、および、光学情報が必要となる。幾何情報の取得技術は、レンジセンサに代表される形状取得センサの発達に加え、データ統合・処理アルゴリズムの進歩により実用に近づいている。その一方で、光学情報（反射率）の取得は、特に屋外の物体について課題となっている。

本論文で対象とする物体は、屋外にある建造物のような大規模な物体である。対象物の大きさは、およそ100m×100m×50m程度までである。このような大きな物体の場合、物体表面の反射特性をどのように計測するかは重要な問題となる。物体の見えは、既知の三次元形状に画像をテクスチャマッピングすることによりモデル化できる。しかしながら、テクスチャ間で統一的な色を再現するためには、事前に光源の影響を除く必要がある。このために、表面色推定、及び、表面反射率推定の手法を提案する。

本稿では、ピクセル単位で表面色推定を行う手法を二つ提案する。既存の表面色推定手法（色恒常性手法とも呼ばれる）は、シーン内で一定の照明光を仮定するが、これは影や曲面を含むような画像では、一般に成り立たない。提案手法は、光源色の変化を用いることにより、ピクセル単位の処理を可能にした。二つの手法は、それぞれ光源色のモデルを利用することで、二つの画素値から表面色を一意に決定することができる。まずはじめに、本稿は黒体放射を光源色のモデルとした手法を提案する。また、手法の安定性と実用性について述べる。次に、より実用的な手法を提案する。ここでは、モデルは屋外光源色の統計的なデータを基にしている。光源色の範囲を用いることで、ロバストな推定が可能となる。

任意の光源環境下での見えを合成するには、物体の反射率が必要とされる。ここでは、全周画像と既知の形状を用いて、物体の反射率を推定する手法を提案する。全周画像は、ほぼ360度の画角を持つため、対象物の輝度と周囲の光源環境の輝度を一度に撮影することができる。このお陰で、推定に特殊な光学機器の必要がなく、またカメラの露光時間や絞り、ゲインなどの情報が無くても、推定を行うことができる。さらには、全周画像の特長として、幾何形状との較正がロバストに行えるという利点がある。提案手法により、計測およびデータ処理にかかるコストを大きく削減できる。多くの手間を必要とする従来手法と比較したとき、大型の物体に関して、これは大きな利点となる。

以上の研究に関して、本論文の主要な貢献は、物体表面の反射特性を推定する三つの手

法を提案したことにある．具体的には，次の三点にまとめられる．第一に，ピクセル単位の表面色推定における安定性と実用性に関して，物理学的な側面から知見を得た．第二に，屋外のシーンに対してもロバストでかつ正確な計算が可能な，ピクセル単位の表面色推定の手法を開発した．既存の手法の中には，ピクセル単位の推定を提案手法以上の精度で推定できるものは，筆者の知る限り存在しない．第三に，屋外環境下にある大規模物体に対して，表面反射率推定を行うのための，効率的な手法を開発した．本論文による提案手法は，屋外における大規模物体の見えるモデル化システムを開発する際の基礎的な手法として実用化できる．

## Acknowledgements

First and foremost, I would like to express my gratitude to my advisor, Prof. Katsushi Ikeuchi. Not only has he advised me to pursue my Ph.D., he has offered me an open door and an open mind, encouraging me and providing me with countless ideas through discussions. A favorite memory is the time when he spent hours with me revising my paper line by line. I can never forget the effort he made to teach me how to act as a researcher.

I would also like to thank my committee members, Hiroshi Harashima, Mitsuru Ishizuka, Kiyoharu Aizawa, Yoichi Sato, and Takeshi Naemura, for giving valuable advice on this thesis.

Many thanks go to the people that I have been working with, the current and former members of the Computer Vision Laboratory at the University of Tokyo. Special thanks go to Robby T. Tan and Jun Takamatsu, who gave me a many ideas and held important discussions with me throughout my work, to Sonoko Okura for helping me with experiments and writing a paper, to Daisuke Miyazaki, Imari Sato, Takeshi Oishi, Atsuhiko Banno, Shunsuke Kudoh, Shintaro Ono, Akifumi Ikari, Hiroki Unten, and Koichi Ogawara, who instructed me in the earlier years of my study. I would like to thank Tetsuya Kakuta, Tetsuro Morimoto, and Tomoaki Higo, for having interesting and fruitful discussions with me regarding the field of physics-based vision, and to Miti Ruchanurucks, Yasuhide Okamoto, and Mawo Kamakura, for making my lab-time enjoyable. I am also indebted to Masataka Kagesawa, Kiminori Hasegawa, Keiko Motoki, Yoshiko Matsuura, and Kaoru Kikuchi for their constant and warm support.

I would like to thank Dr. Joan Knapp for spending considerable time proofreading my English manuscripts. She kindly improved my writing and gave me many appropriate suggestions.

Many friends helped me relax and made my student life delightful. Special thanks go to Maki Hayashida, Maki Murofushi, and Kumiko Yumoto for their longstanding support since our junior high school years. I also want to express my genuine gratitude to Yoichi Katayama, who motivated me and made me smile throughout my university life.

Last but not least, I would like to thank my family, Katsura, Keiko and Hiromu, for always being patient and supporting me during my twenty-two-year student life. It has been a long effort but worth doing, and I could not finish it without all of your support. I dedicate this dissertation to my family.

December 2007

# Contents

<b>Abstract</b>	<b>i</b>
<b>論文要旨</b>	<b>iii</b>
<b>Acknowledgements</b>	<b>v</b>
<b>List of Figures</b>	<b>ix</b>
<b>List of Tables</b>	<b>xvii</b>
<b>1 Introduction</b>	<b>1</b>
1.1 Background . . . . .	1
1.1.1 Color Constancy . . . . .	5
1.1.2 Albedo Estimation . . . . .	7
1.2 Research Objective . . . . .	9
1.3 Thesis overview . . . . .	10
<b>2 Estimating Surface Chromaticity from Blackbody Illumination</b>	<b>13</b>
2.1 Introduction . . . . .	13
2.1.1 Related Work . . . . .	14
2.1.2 Blackbody Illumination . . . . .	18
2.2 General Problem Formulation . . . . .	20
2.3 Illumination Chromaticity Formulation . . . . .	21
2.4 Our Problem Formulation . . . . .	22
2.5 Solutions . . . . .	23
2.6 Experiments . . . . .	29
2.6.1 Simulation Data . . . . .	29
2.6.2 Real Data . . . . .	30
2.7 Discussion . . . . .	39
2.8 Summary . . . . .	40

<b>3</b>	<b>Robust Framework to Estimate Surface Chromaticity from Illumination Changes</b>	<b>43</b>
3.1	Introduction . . . . .	44
3.2	Assumptions and Definitions . . . . .	45
3.3	Surface Color Estimation . . . . .	46
3.4	The Effect of Input Errors . . . . .	47
3.4.1	Input errors . . . . .	49
3.4.2	The effect of input errors on surface color estimation . . . . .	55
3.4.3	Decreasing the effect of input errors . . . . .	56
3.5	Proposed method I: Robust Framework . . . . .	60
3.5.1	Finite range of outdoor illumination . . . . .	60
3.5.2	Detecting the Estimation error . . . . .	61
3.5.3	Correcting the Error of Input Image Chromaticity . . . . .	63
3.5.4	Selecting the Input Image Chromaticity to be Corrected . . . . .	63
3.5.5	Experiments . . . . .	64
3.6	Proposed method II: Using Shadows . . . . .	81
3.6.1	Shadowed and Non-shadowed Region . . . . .	82
3.6.2	Illumination Invariant . . . . .	87
3.6.3	Implementation for Extracting Two Colors . . . . .	88
3.6.4	Experiments . . . . .	88
3.7	Summary . . . . .	93
<b>4</b>	<b>Estimating Surface Reflectance Using Spherical Images</b>	<b>99</b>
4.1	Introduction . . . . .	99
4.1.1	Related work . . . . .	100
4.2	Scene Radiance Acquisition with a Spherical Camera . . . . .	101
4.2.1	Illumination radiance . . . . .	102
4.2.2	Surface radiance . . . . .	103
4.3	Reflectance Estimation from Scene Radiance and Object's Shape . . . . .	105
4.3.1	Surface irradiance . . . . .	105
4.3.2	Surface reflectance estimation . . . . .	106
4.4	Experiment . . . . .	106
4.4.1	Measurement of the scene radiance . . . . .	106
4.4.2	Vignetting rectification . . . . .	107
4.4.3	Generating an HDR image . . . . .	110
4.4.4	Measurement of the object's shape . . . . .	110

4.4.5	Estimation of the surface reflectance . . . . .	110
4.4.6	Evaluation . . . . .	110
4.5	Discussion . . . . .	112
4.6	Summary . . . . .	114
<b>5</b>	<b>Conclusions</b>	<b>115</b>
5.1	Summary . . . . .	115
5.1.1	Estimating surface chromaticity from Blackbody illumination . .	115
5.1.2	Robust framework to estimate surface chromaticity from illumina- tion changes . . . . .	116
5.1.3	Estimating surface reflectance using spherical images . . . . .	116
5.2	Contributions . . . . .	117
5.3	Future Directions . . . . .	117
5.3.1	Applying surface color estimation for plausible texture generation	118
5.3.2	Surface color estimation using photo-sharing site . . . . .	118
5.3.3	Shadow extraction . . . . .	118
5.3.4	Development of high-performance spherical camera . . . . .	118
5.3.5	Surface reflectance estimation of specular objects . . . . .	119
5.3.6	Illumination recovery from partially acquired albedo . . . . .	119
	<b>References</b>	<b>120</b>
	<b>List of Publications</b>	<b>133</b>



# List of Figures

1.1	An example of a large-scale 3D model. A 3D model of the Bayon Temple, a stone heritage object in Angkor, Cambodia. . . . .	3
1.2	Textured 3D model of the south side of the Bayon Temple in Cambodia. The color of the textures is different depending on illumination at the time they were taken. The objective of this research is to remove the effect of illumination color from those textures. . . . .	4
1.3	Color constancy. The top image is taken at dusk, and the bottom image is the result of color constancy. . . . .	6
1.4	The object's appearance is determined by its shape, surrounding illumination, and surface reflectance (albedo.) . . . . .	8
2.1	The goal of this work; to estimate surface color, the object's color under white illumination, from the object's colors under arbitrary colored illumination. Blackbody radiation is regarded as the illumination spectra. . . . .	15
2.2	The comparison between the state-of-the-art color constancy algorithms [vdWGG07]: the Gray-World, the general Gray-World, and the Gray-Edge algorithms. The gray spheres exhibit the ground truths of the illumination color. The angular error between the estimated and the ground truth is indicated by the number in the right bottom corner. They still have difficulties when the scene includes few surface colors, or the scene is dominated by a single color. . . . .	16
2.3	Daylight spectra plotted in the 1931 CIE chromaticity diagram, obtained in the following: (a) America, England and Canada [JMW64], (b) Canada [NW63], (c) South Africa [WBKT66] and (d) Australia [Dix78]. The red dotted curves indicate the locus of chromaticities implied by Planck's blackbody radiation law. The Planckian locus could approximate daylight colors well in most places of the world. . . . .	19

2.4	Daylight spectra obtained with a narrow field-of-view apparatus, plotted in the 1931 CIE chromaticity diagram: (a) India [SD68], (b) Spain [HARN01]. The red dotted curves indicate the Planckian locus. . . . .	20
2.5	Illustration of notations. Color temperatures $T_1$ and $T_2$ are estimated from image chromaticities $i_1$ and $i_2$ taken under two blackbody illumination. Consequently, surface chromaticity $s$ can be calculated. . . . .	23
2.6	The shape of the evaluation function $\Theta_r$ , given an arbitrary $T'_1$ . $T'_2$ that gives $\Theta_r = 0$ always exists and can be calculated by bracketing. We let the initial value of $t'_2$ be one side of the brackets, and find the other side by going up or down the slope until the sign of $\Theta_r$ changes. . . . .	25
2.7	The shape of $T'_{2r} - T'_{2g}$ around the true solution. If $T'_1$ increases/decreases, $T'_{2r} - T'_{2g}$ increases/decreases. Therefore, the solution can be calculated by bracketing. . . . .	27
2.8	Ideal data used in the experiments; (a) seven kinds of blackbody illuminants; corresponding color temperatures are 2500, 3500, 4500, 5500, 6500, 7500, and 10000 in Kelvin. (b) Six reflectance patches of GretagMacbeth ColorChecker used in the experiments. (c) Ideal camera sensitivity. . . . .	31
2.9	Real data used in the experiments; (a) eight illuminants' spectra: A, B, C of CIE standard illuminants and Judd daylight phases D48, D55, D65, D75 and D100. Note the difference between the data shown in Figure 2.8(a). (b) Six reflectance patches. (c) Camera sensitivities. They are the sensitivities of band-pass filters: MellesGriot 03FIV119, 03FIV111, 03FIV004. . . . .	34
2.10	The plots of estimation error against the violation of the blackbody assumption; " $\Delta T1$ " and " $\Delta T2$ " express the estimation error. The JND chromaticity difference (5.5 mired) is also shown. In order to limit the estimation error to be lower than 5.5 mired, the violation should be under about 0.1 %. . . . .	35
2.11	Virtual camera sensitivities. The standard deviation of Gaussian functions are changed from 1 nm to 20 nm. . . . .	37
2.12	Reflectance data used in the fourth set of experiments; three reflectances are "Dark skin," "Light skin," and "Green" of the Macbeth ColorChecker. "Dark skin" varies linearly around wavelengths of a camera sensitivity compared to "Light skin" and "Green." . . . . .	37

2.13	The plot of estimation error against the violation of the narrow-band sensitivity assumption. The more the bandwidth of a camera sensitivity (the standard deviation $\sigma$ of a Gaussian function) grows, the larger the estimation error becomes. Three reflectances “dark skin,” “light skin,” and “green” were tested. The speed of the error growth depends on reflectance. . . . .	38
3.1	(a) Typical daylight data roughly form a line in an inverse-chromaticity space. Crosses: Daylight data (CIE standards and Judd et al.’s daylight phases). Line: Finlayson et al.’s illumination line obtained by the least-square fitting. The Planckian locus is also shown for comparison. (b) The sensitivity of SONY-DXC9000. Each chromaticity in (a) was calculated in the color space of it. . . . .	48
3.2	Simulated image chromaticities under illumination change: Actual (crosses) and ideal (lines) chromaticities in inverse-chromaticity space according to (a) Blue, (b) Green, (c) Red, (d) Yellow, (e) Magenta, and (f) Cyan reflectances with various illuminations; the details of data used for this simulation are shown in Table 3.1. Most actual image chromaticities ( $i_r, i_g$ ) include a small error ( $\Delta i_r, \Delta i_g$ ) from ideal values ( $\hat{i}_r, \hat{i}_g$ ) due to the straight-line and the narrowband assumptions. While it is difficult to predict an error value from an input value. . . . .	51
3.3	Other examples of simulated image chromaticities under illumination change: Actual (crosses) and ideal (lines) chromaticities according to (a) Dark skin, (b) Light skin, (c) Blue sky, (d) Foliage, (e) Blue flower and (f) Bluish green. . . . .	52
3.4	Other examples of simulated image chromaticities under illumination change: Actual (crosses) and ideal (lines) chromaticities according to (a) Orange, (b) Purplish blue, (c) Moderate red, (d) Purple, (e) Yellow green, and (f) Orange yellow. . . . .	53
3.5	The distribution of the sum of the input error values, $D^{\text{input}}$ . The average value was 0.0496, and the mode was 0.027. We also tested the distributions with Nikon D1 and SONY ICX204AK, and the averages were 0.0491 and 0.0664, respectively. The numbers predict that SONY DXC-9000 and Nikon D1 will produce similar algorithm performance. . . . .	54

3.6	We simulated the actual value of $W$ , which affects the surface chromaticity estimation. $W$ is always larger than 1.0, and thus, it magnifies the input error for the estimation. The sensitivity shown in Figure 3.1(b) was used to calculate the illumination chromaticity in this simulation. . . . .	56
3.7	The estimation error values in CIE LAB color space against $D^{\text{input}}W$ . The estimation error increases approximately linearly as $D^{\text{input}}W$ increases. The value of $D^{\text{input}}W$ needs to be less than 0.2 to suppress the estimation error value under 10 CIE LAB errors. Consequently, the preferable color temperature difference between two illumination colors will be more than 100 mired ( $W \leq 4$ in Figure 3.6), since the average value of $D^{\text{input}}$ is about 0.05. . . . .	58
3.8	CIE LAB color examples. The value of $L^*$ is uniform in the figure. From the figure, we decided that the error in surface/illumination estimation should be less than 10.0 in CIE LAB color space. . . . .	59
3.9	Lines 1 and 2 are generated by $i^1$ and $i^2$ . When the intersection $s$ divides Line 1 in $p : 1 - p$ , the light color $e^1$ divides the Illumination line in $p : 1 - p$ .	62
3.10	(a) The case of adjusting $i_g^1$ . (b) The case of adjusting $i_g^2$ . The ratio $p$ does not change in either case. . . . .	65
3.11	Images of the Macbeth ColorChecker taken under different outdoor illuminants (L1 to L6). Illuminant's color gradually changes from (a) to (f). Eighteen surface colors (colors surrounded by the red dotted line) were used in the experiments. . . . .	66
3.12	(a) Six illuminants which are plotted in the inverse-chromaticity space. (b) The spectral distribution of L6 is shown as an example. The spectrum also shown is the blackbody radiation curve of 7083 K. . . . .	67
3.13	The figure shows the results of using (a) Red, and (b) Dark skin, of the Macbeth chart. Each row shows a pair of input images, estimated chromaticities (of two illuminants and a surface) obtained by the proposed method, the ground truth, and the previous method [FFB95]. L1 to L6 are the outdoor illuminants that are used; there are ${}_6C_2 = 15$ rows for each surface color. The bottom row shows the average of the estimated surface colors by each method. . . . .	69
3.14	The figure shows the results of using (a) Orange, and (b) Moderate red, of the Macbeth chart. . . . .	70

3.15	The figure shows the results of using (a) Purple, and (b) Magenta, of the Macbeth chart. . . . .	71
3.16	The figure shows the results of using (a) Purplish blue, and (b) Blue, of the Macbeth chart. . . . .	72
3.17	The figure shows the results of using (a) Orange yellow, and (b) Yellow, of the Macbeth chart. . . . .	73
3.18	The figure shows the results of using (a) Foliage, and (b) Bluish green, of the Macbeth chart. . . . .	74
3.19	The figure shows the results of using (a) Green, and (b) Yellow green, of the Macbeth chart. . . . .	75
3.20	The figure shows the results of using (a) Blue sky, and (b) Cyan, of the Macbeth chart. . . . .	76
3.21	The figure shows the results of using (a) Light skin, and (b) Blue flower, of the Macbeth chart. . . . .	77
3.22	Histograms of estimation errors of the illuminant 1; $e^1$ (top), illuminant 2; $e^2$ (middle), and surface; $s$ (bottom). The estimation error is defined as the Euclidean distance between the estimated and true chromaticities in CIE LAB color space. The averages of the proposed method were 8.6 (redder illuminants $e^1$ ), 8.7 (bluer illuminants $e^2$ ) and 8.0 (surface $s$ ). Those of the previous method [FFB95] were 104.2 (redder illuminants $e^1$ ), 98.6 (bluer illuminants $e^2$ ) and 74.2 (surface $s$ ). . . . .	78
3.23	The estimated illumination chromaticities' distribution in an inverse-chromaticity space. Estimated values are restrained on the defined line segment. In (c) and (d), the estimated values were more widely spread compared to (a) and (b), due to the less color difference of illuminations.	79
3.24	Comparison results between our proposed method and Finlayson et al.'s method. . . . .	82
3.25	(a) One of the two input scene, illuminated by cloudy daylight at 18:05. (b) The other input, illuminated by cloudy daylight at 15:05. . . . .	83
3.26	(a) The estimated scene actual color of the image shown in Fig. 3.25(a), computed using our proposed method. (b) The estimated scene actual color using the standard white reference. . . . .	84
3.27	(a) One of the two input scene, illuminated by cloudy daylight at 18:05. (b) The other input, illuminated by cloudy daylight at 15:05. . . . .	85

3.28	(a) The estimated scene actual color of the image shown in (a), computed using our proposed method. (b) The estimated scene actual color using the standard white reference. . . . .	86
3.29	Experimental setup and obtained input images: (a) We placed the target object and light sources so that each surface of the object is illuminated by different illuminants. (b) - (e) Obtained images of blue, yellow, green, and red objects. . . . .	90
3.30	Experimental Results of four objects. (a) Input image chromaticities. (b) Estimated surface chromaticity by the proposed method. (c) Results of the previous method [FFB95]. (d) Ground truths of the top row. (e) Used pixels for our estimation. . . . .	92
3.31	Results of fitting the Gaussian mixture model to the input image's distributions. The image used was Figure 3.30(c). The left is the Gaussian fitted to the histogram of $\log(F)$ values of the input image, and the right is that of $\log(r)$ values that have the selected $F$ value. The distributions fit the Gaussians well in $\log(F)$ and $\log(r)$ spaces, and therefore two colors from shadowed and non-shadowed regions can be extracted successfully.	93
3.32	An example of applying the proposed method to an outdoor image. . .	94
3.33	Details of our method's processes. . . . .	95
3.34	Another example of applying the method to an outdoor image. Two chromaticities in (b) are unified in (d). . . . .	96
3.35	Details of our method's processes. . . . .	97
4.1	A camera Ladybug2 [Lad]. . . . .	102
4.2	An image taken by Ladybug2. . . . .	103
4.3	Illustration of our notations. The spherical camera at camera center $C$ acquires radiance distribution of illumination environment $L(\lambda, \theta, \phi)$ as well as the radiance of the surface $A$ . $\theta$ and $\phi$ are the polar and zenith angles. . . . .	104
4.4	(a) The direction $(\theta_i, \phi_i)$ of incident light rays to the surface $A$ . (b) The solid angle at the direction $(\theta_i, \phi_i)$ . . . . .	105
4.5	Ladybug2 with an ND filter. . . . .	107
4.6	A set of images taken on a sunny day. The unit of shutter speeds is micro second. Normally, about twenty and ten images were taken on sunny and cloudy days, respectively. . . . .	108

4.7	(a) an image with vignette-like effect. See the upper right of the image. The reduction of image is highly visible. (b) the estimated vignette-like effect. (c) an image rectified. Image brightness is recovered. . . . .	109
4.8	The captured images at (a) 14:35, illuminated by cloudy daylight, (b) 17:52, illuminated by twilight, (c) 11:50, illuminated by sunny daylight, are shown. The rendered images of the object's shape, (d) on cloudy day, (e) at dusk, and (f) on a sunny day, are shown in the middle row. Images in the bottom row are the estimated surface reflectance. (g) was derived from the images (a) and (d), (h) was from the images (b) and (e), and (i) was from (c) and (f). . . . .	111
4.9	Zoomed images of estimated surface reflectance, shown in Fig. (g), (h) and (i). . . . .	112
4.10	An inaccurate HDR image. . . . .	113



# List of Tables

2.1	The average estimation error in 126 experiments using simulation data. The estimation error by the previous method [FFB95] is also shown for reference. . . . .	30
2.2	The average and the standard deviation of estimation errors in 500 experiments with different initial values. . . . .	32
2.3	The average estimation error in 168 experiments using real data. The estimation error by the previous method [FFB95] is also shown for reference. 18 results of the previous method were excluded from the average CIE LAB error calculation, since those estimates include negative values. . . . .	33
2.4	Difference between blackbody and real spectra. $\Delta e_r$ and $\Delta e_g$ are the error percentage of the illuminant's color to the nearest blackbody color. Note that the difference is defined in the color space of the sensitivity used in this experiment. . . . .	36
2.5	Difference between real illumination colors and colors calculated from the straight line illumination model. $\Delta e_r$ and $\Delta e_g$ are the error percentage of the illuminant's color to the straight line color model. Note that the difference is defined in the color space of the sensitivity used in Table 2.4. . . . .	40
3.1	Data used to simulate actual and ideal image chromaticities. . . . .	50
3.2	The values of estimation error rate when the inputs include errors. . . . .	55
3.3	Details of six illuminants used in the evaluation experiments. . . . .	68
3.4	Details of illuminants used in the evaluation experiments. . . . .	89
3.5	Estimated and true chromaticities of illumination colors. . . . .	91



# Chapter 1

## Introduction

### 1.1 Background

Digital three-dimensional models created by computer vision and graphics techniques are widely used in a variety of workplaces, such as mechanical and architectural industries, and for a variety of purposes, such as visualization in the fields of research, education, and entertainment. Specifically, modeling cultural heritage objects has attracted considerable attention [IOT\*07], since such objects are worth preserving and the data can be utilized for restoration when an object faces the crisis of collapse. The data can be linked to geometrical information [Gooa] via communication network and can be broadcasted to people to view and enjoy remotely. The data could also be utilized for virtual space [Sec] and a virtual museum, and for driving simulators, movies, and games. Thus, digital three-dimensional models offer substantial commercial possibilities.

Automation for creating 3D models has also attracted much interest as the need for such models has increased. Currently, most models are created by manual operation [Aut, Goob], causing a significant increase in cost, and therefore more sophisticated techniques for modeling a real world object are demanded for supplying 3D data at lower cost. Such techniques could also be used for automation in industries and for robotic vision.

To simulate the accurate appearance of an object, we have to know the object's shape and surface reflectance properties. Acquiring shape information has been facilitated by the development of sensors and the progress of data processing algorithms [IOT\*07].

Meanwhile, a number of methods that reconstruct 3D shapes from images with multiple views have been intensively studied, such as stereo techniques [DM76, DA89], visual hull [Lau94, MBR\*00], voxel coloring, and space carving [SD97, KS00], and these methods have achieved highly convincing results. However, to re-render the object's color under novel lighting conditions, the object's surface reflectance properties are required. The recovered colors from the methods cited above only represent a specific appearance under one lighting condition.

Acquiring surface reflectance properties remains a challenge, specifically with outdoor objects. In the late 1990s, several modeling methods with range sensors were proposed [PCD\*97, NK99, LHS00, WKSS01, BMR01]; however, those methods created surface textures by simply blending images taken from multiple views. Meanwhile, physics-based reflectance estimation methods [TW89a, KSK90, NIK91, ON51, DvGNK97, SWI97, LL99, NZI01, MYT03, YXA07], photometric stereo techniques [Ike81, Hor86, BJ01, ZBK02, HS05, GCHS05, CGS06], and image-based rendering techniques [LH96, GGSC96, KBK01, RH02, SOSI03, WMTG05] have been proposed to create more physically correct object appearances than those created in the early 1990s. Physics-based reflectance estimation is based on physical reflection models [CT81, ON51] and estimates the parameters of the models by fitting the data to them. The methods have achieved highly accurate re-renderings, yet they need accurately calibrated illuminants and cameras. Some of those methods [DvGNK97, SWI97, NZI01, MYT03, YXA07] require around 100 images for an accurate estimation. Photometric stereo is a method that captures images under three different lighting conditions and estimates the surface reflectance and the surface normal of the shape. Generally, it assumes a known distant point light source, and therefore it is unsuitable for outdoor conditions. Image-based rendering is a technique that samples appearances under a number of different lighting conditions, and re-renders the appearance by interpolating the images. For instance, diffuse objects would require about 30 images, and more than 100 images are needed for specular objects [SOSI03]. Creating such a number of different illumination conditions is impractical for an outdoor environment, and so it is difficult to be applied to outdoor objects. In other words, an appearance of a small object, without complex reflection (transparent, layered, or metallic), can be accurately modeled by calibrating illumination and sampling a number of images.

This paper attempts to handle a large-scale object such as an architectural structure in an outdoor environment. Figure 1.1 shows an example, a 3D model of Bayon Temple,



Figure 1.1: An example of a large-scale 3D model. A 3D model of the Bayon Temple, a stone heritage object in Angkor, Cambodia.

a stone heritage object in Angkor, Cambodia. The size of Bayon Temple is around  $100\text{ m} \times 100\text{ m} \times 50\text{ m}$ . For such a huge object, measuring the surface reflectance properties becomes a challenge. Figure 1.2 shows the result of directly mapping the acquired images by texture mapping [Hec86, DW80] to the model of Bayon Temple. As Figure 1.2 shows, the color of the object varies from left to right, due to the difference of time at which the images are taken. The aforementioned methods cannot be applied to this object because of the difficulty in controlling the lighting condition, and therefore an alternative is required to remove the color difference due to the illumination change.

This paper models the appearance of an object by mapping the image textures to the known shape of the object. To avoid the discontinuity in textures (Figure 1.2) and arrive at consistent colors, we analyze the images and remove the effect of illumination before mapping them by using the surface chromaticity estimation and surface reflectance estimation techniques. Chromaticity is a concept that represents color information; it is a color value normalized by its intensity value. Surface chromaticity estimation,

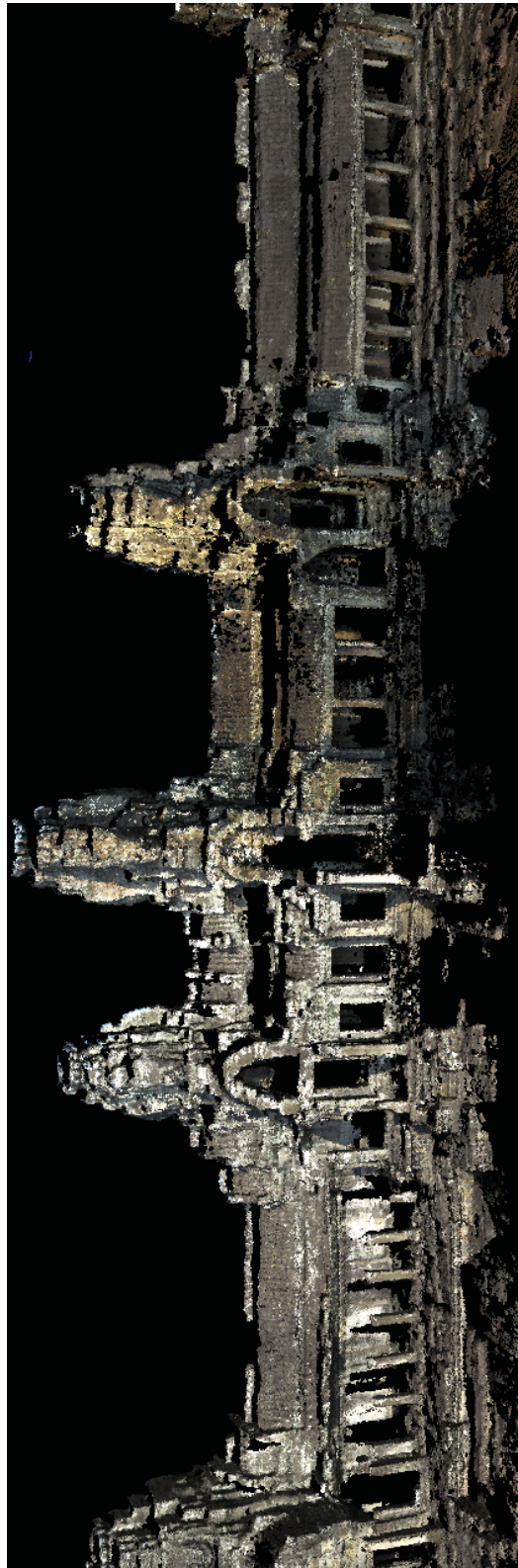


Figure 1.2: Textured 3D model of the south side of the Bayon Temple in Cambodia. The color of the textures is different depending on illumination at the time they were taken. The objective of this research is to remove the effect of illumination color from those textures.

so-called color constancy, has been intensively studied in the computer vision research field. Surface reflectance estimation has been studied in terms of albedo estimation. The paper will show that the color appearance of an object can be modeled by using those techniques. The following section surveys methods that have been proposed related to those research topics.

### 1.1.1 Color Constancy

The simplest way to remove the effect of illumination and to acquire the object's surface color is white balance, a method widely used by professional photographers. White balance is a method that balances RGB values by attaching color filters in front of the lens, so that a reference white board looks white in the image. In the case of large-scale objects, a white board may not be able to capture the identical illumination over the target object. Hence, a method to achieve an automatic white balance would be of great benefit.

Human perception has this kind of ability, automatic white balance, which is specifically called color constancy. Color constancy has been studied in the field of computer vision, where it is regarded as the same as surface chromaticity estimation. Color is converted by scaling original RGB values. At this point, the ratio of the scaling factors between RGB channels is important, since there is a scale ambiguity in the absolute illumination/surface reflectance relation. Therefore, not the absolute surface color but the surface chromaticity (color normalized by its intensity) is estimated. This color conversion is physically correct for diffuse planar objects, except for approximating the spectral conversion by the RGB conversion. Figure 1.3 shows an example of the results of color constancy. We can see that this technique is fundamental for acquiring an object's surface property.

Many color-constancy methods have been proposed, while none of them can perform perfect color constancy. Methods that use the presence of highlighting [DL86, Lee86, TW89b, Lee90, FS01, TNI04], are accurate though less applicable for large outdoor objects such as the Bayon Temple. Methods that can handle diffuse objects are categorized into two groups [Hor06]: algorithms that use information from a learning phase [For90, NS92, Fin96, BF97, RHT01, FHH01, TEW01, TW02, FHM05, FHT06] and those based on low-level image features [Buc80, Lan77, FT04, vdWGG07, GG07]. Both methods have difficulties when the scene includes few surface colors, and usually assume a scene lit by a uniformly colored illumination, which is not the case for curved



(a) Original image.



(b) Result of color constancy.

Figure 1.3: Color constancy. The top image is taken at dusk, and the bottom image is the result of color constancy.

objects or objects with shadows, under outdoor environment.

### 1.1.2 Albedo Estimation

With respect to diffuse objects of arbitrary shape, we need to estimate not only the surface chromaticity but also the absolute surface reflectance, so-called *surface albedo*, for recovering the appearance of the object under a novel illumination condition. Albedo is the ratio of reflected light to the incident electromagnetic radiation, i.e., how much light a material will reflect regarding the incident light. This paper defines the albedo on each RGB channel; the maximum albedo (no absorption) is (1.0, 1.0, 1.0) for ( $R$ ,  $G$ ,  $B$ ). Albedo estimation calculates the absolute scale on each sensor channel, while color constancy allows the scale ambiguity. Figure 1.4 shows an example of surface albedo. We can clearly see that the surface albedo is the most essential component in terms of the object's surface property. However, we have to take the shape information into account.

Albedo has been an important concept in climatology and astronomy for environmental monitoring and predicting the properties of far objects that cannot be resolved by telescopes. In terms of climatology, the earth's surface albedo has been regularly estimated via remote sensors such as NASA's ASTER, MISR, and MODIS devices on the Terra and Aqua satellites. The collected data indicate materials that constitute the surface of the earth. In those cases, a mathematical model of the BRDF is used to translate a sample set of satellite reflectance measurements into estimates of the set of reflectance. Different models from those in computer vision and graphics research fields have been used because of the difference in resolution and the effect of atmospheric absorption.

In computer vision and graphics research fields, several methods that handle outdoor images have been proposed. A few are using images of monitoring cameras placed outdoors. Weiss [Wei01] derived intrinsic images, which are images representing surface albedo, by assuming that the sudden change caused by reflectance remains constant in the image sequence, while that caused by illumination varies depending on the time. Therefore, by taking the median of derivative filter outputs of input images, the reflectance image can be estimated. Matsushita et al. extended the idea so that it can handle non-Lambertian surfaces, and proposed an illumination normalization scheme utilizing the illumination eigen space and a shadow interpolation method based on shadow hulls [MNIS04].

For directly calculating surface reflectance properties, one would need three com-



(a) Appearance.



(b) Shape and illumination.



(c) Surface albedo.

Figure 1.4: The object's appearance is determined by its shape, surrounding illumination, and surface reflectance (albedo.)

ponents: the shape of a target object, the actual appearance of the object, and the illumination environment. Shape information and actual appearance can be obtained by range and image sensors, respectively.

Two methods, as far as we know, that recovered outdoor objects' surface reflectance, measured the listed three components. Yu et al., the first who handled outdoor objects, according to the author's knowledge, took photographs of the sun and sky to measure their radiance distribution [YM98]. As they used a normal camera, they included landmarks in each photograph so that they could use them to recover the camera pose later. Debevec et al., the second and the latest to tackle the outdoor problem, used a specific apparatus to measure the outside illumination [DTG\*04]. They used a mirrored sphere to image the sky and clouds, a shiny black sphere to indicate the position of the sun, and a diffuse grey sphere to indirectly measure the intensity of the sun. Those methods need elaborate procedures and therefore the size of the objects they handled was rather small compared with our target objects.

## 1.2 Research Objective

This dissertation describes two research objectives: one is to estimate surface chromaticity from images and the other is to estimate surface albedo from an image with known shape information. Estimating surface chromaticity is important for modeling the appearance of an object. In general color constancy methods we have to assume a uniform illumination in the scene. However, this is not always the case; suppose that shadows are presented in an image. Shadowed regions outdoors are usually illuminated by sky light, while non-shadowed regions are illuminated by the combination of sky light and sunlight. Thus, this paper proposes methods that can calculate the surface color by a pixel-based operation.

Our methods enable a pixel-based operation by utilizing the change of the illumination. The change of the illumination can be a key for estimating surface colors from image values. Outdoor illumination is well known to be modeled by blackbody radiation, which is the spectra that are emitted from a black body (graphite, etc.) when it is heated. By introducing this model for illumination colors, a surface color is uniquely determined from two image values taken under different illumination. First we propose a method that utilizes the blackbody radiation formula, and analyze the stability and practicality of this problem from the physical perspective. Then, we propose a more practical method that can perform robust estimation by using another model

for illumination colors derived from statistical outdoor illumination data. The robust estimation is realized by introducing the plausible range of outdoor illumination colors.

In a practical situation, estimating surface albedo would be the principal goal for acquiring the surface properties of diffuse objects, since surface chromaticity represents the surface property up to a scale, while surface albedo is the absolute value. The methods of surface color estimation are adequate for planar objects; however, objects with an arbitrary shape will cause an undesirable effect, due to the variation in surface normals. This will need further processing of images, which should involve the estimation of surface normals and illumination distributions.

In our approach, we assume that the shape information is already acquired, and attempt to estimate surface albedos from spherical images. With respect to surface albedo estimation, there are a few methods that handle outdoor scenes, and previously proposed methods need elaborate procedures such as photometrical calibration of measuring devices and geometrical calibration between the acquired illumination distribution and the shape information. We propose a novel method that utilizes spherical images with shape information. Spherical images have a nearly 360-degree field of view. Thus, geometric calibration between the image and shape information becomes robust. Furthermore, we do not need to know the camera gain factor, exposure time, and aperture, since all those factors are shared in both illumination and surface radiance distributions. Spherical images capture both illumination distribution and surface radiance distribution at one shot, which is a great advantage for estimating surface albedos. Measurement and data-processing cost will be greatly decreased by this method.

### 1.3 Thesis overview

Chapter 2 describes a method that estimates surface colors by assuming that the blackbody radiation approximates the outdoor illumination colors. The chapter provides a theoretical analysis that a surface color can be uniquely determined from two image values taken under two sets of illumination. After briefly reviewing the previous works and the blackbody radiation model, the chapter explains a formulation of estimating surface colors and of blackbody illumination colors in a chromaticity space. Chromaticity is a color ratio between RGB values, and is an important concept in most color constancy methods. Then, a novel approach to calculate surface colors is pre-

sented, and experimental results on both synthetic and real data are provided. Having discussed the robustness of the proposed method, the chapter summarizes the method.

Chapter 3 proposes a method that stabilizes illumination-color estimation by using the statistical model of illumination colors and the idea of a finite illumination color space. We first describe the objective and novelty of the method, and then explain the assumptions and definitions that are used in the method. The solution for estimating surface color is presented, and the effect of input errors on this solution is investigated thoroughly. A method for robust estimation is presented and experimental evaluation is provided. Subsequently, an extension of the method to a single image using the shadowed and non-shadowed regions is described. We explain an algorithm to extract two representative colors from those regions and provide experimental results on both toy objects and large-scale objects in an outdoor environment. Finally, we summarize the method.

Chapter 4 proposes a new, efficient method to estimate surface reflectance (albedo) of diffuse outdoor objects from only one measurement with a spherical camera. After reviewing the previous works, we explain the mathematical formulation of the scene's radiance acquisition. Both illumination radiance and surface radiance can be captured by the spherical camera that we used. Then, a method for estimating surface reflectance is described. Surface irradiance can be calculated from captured illumination irradiance, and the surface reflectance is calculated by dividing the surface radiance by its irradiance. After explaining techniques for practically applying the method to outdoor scenes, we evaluate the method with experiments. Finally, we provide discussions and a summary.

Chapter 5 concludes this dissertation by summarizing this research and contributions, and discussing possible future research directions.



## Chapter 2

# Estimating Surface Chromaticity from Blackbody Illumination

From two colors of a surface taken under two illuminations, the surface chromaticity is determined uniquely, if the illumination colors are both equal to ideal blackbody radiation. This chapter provides a theoretical analysis of this fact, and proposes a surface-chromaticity estimation method based on it. The novelty of the method is that it uses the direct mathematical model of blackbody radiation, Planck's formula, as the illumination color model. Aside from Planck's formula, we have also assumed that the bandwidth of camera-sensor sensitivity is sufficiently narrow.

Differing from what we expected, the experimental results showed that although this method is a perfect vehicle for simulation data, it produces significant errors with real data. From a thorough investigation of the cause of errors, we can learn how important the assumptions on both blackbody radiation and narrow-band camera sensitivities are to the method. Finally, we discuss the robustness of our method, and the limitation of estimating surface color using the illumination color constraint.

### 2.1 Introduction

Acquiring an object's inherent color is important when modeling a real-world object. Since color appearance is significantly influenced by the illumination color, a method to remove it and to estimate the actual color of the object's surface, its "color constancy"<sup>1</sup> in computer vision, is required. It is the goal of this work to estimate surface color, the

object's color under white illumination, from the object's colors under arbitrary colored illumination. In general, surface color estimation is achieved by capturing the object's color under a known illuminant, and dividing it by the illumination color. We cannot, however, apply this method when the target objects are huge and are located outdoors, because the illumination condition is not either controllable or known. It would be of great benefit to achieve color constancy only from colors received by sensors.

In this chapter, we propose a new method for surface color (chromaticity) estimation that inputs two colors taken under different illumination and estimates each illumination color numerically by regarding the blackbody radiation as the illumination spectra (Fig.2.1). Blackbody radiation accurately models the light from heated metals. Moreover, several researchers reported that it can predict the general shape of daylight illuminations [FS01, JMW64].

In addition to the blackbody illumination assumption, our method assumes that the bandwidth of camera-sensor sensitivity is sufficiently narrow [FFB95, BFF97, MO00]. The method uses three sensor values at each wavelength, since it is designed to use image values. However, any wavelength can be chosen for the algorithm, which means that the algorithm can be applied to a spectral separation method without any loss of generality.

### 2.1.1 Related Work

A number of methods to estimate surface/illumination colors have been proposed by researchers. We can categorize them into two groups: dichromatic-based methods and diffuse-based methods. Dichromatic-based methods [DL86, Lee86, TW89b, Lee90, FS01, TNI04], though they are accurate, require the presence of highlighting, and are therefore less applicable for large outdoor objects such as the Bayon Temple <sup>2</sup>, or the Kamakura Buddha <sup>3</sup>.

Most diffuse-based methods use a single input image of objects lit by a uniformly colored illumination. According to the recent survey by Hordley [Hor06], diffuse-based methods can be divided into two groups: algorithms that use information from a learning phase and those based on low-level image features. The former methods

<sup>1</sup> "Color constancy" often implies recovering an object's actual surface color in the field of computer vision. Note that, to be precise, it is a psychological term meaning the ability to perceive a color as constant under varying illumination.

<sup>2</sup>A stone heritage object in Angkor, Cambodia.

<sup>3</sup>A large statue of Buddha in Kamakura, Japan.

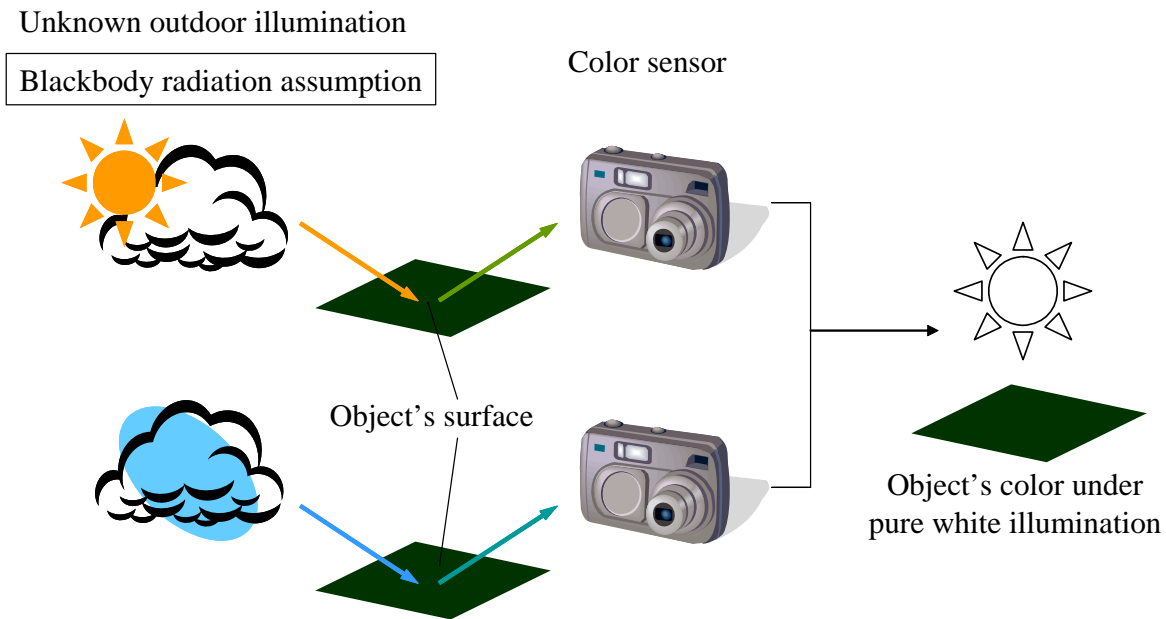


Figure 2.1: The goal of this work; to estimate surface color, the object's color under white illumination, from the object's colors under arbitrary colored illumination. Blackbody radiation is regarded as the illumination spectra.

[For90, NS92, Fin96, BF97, LMHK99, RHT01, FHH01, TEW01, TW02, FHM05, FHT06] use color-distribution bias in an image; by comparing the bias to the previously acquired color distribution, they estimate the illumination color. Therefore, they usually require strong constraints in surface color domain, and cannot accurately handle images with few surface colors [TW02].

The latter is represented by the Gray-World [Buc80] and the White-Patch [Lan77] algorithms. The Gray-World algorithm assumes that the average reflectance color is gray. The White-Patch algorithm assumes that the brightest patch in the image is white. A method that uses Minkowski-norm to generalize low-level feature methods is proposed by Finlayson et al., which is referred to as the general Gray-World algorithm [FT04]. Van de Weijer et al. extended the idea regarding that the average of the reflectance differences in a scene is gray (the Gray-Edge algorithm) [vdWGG07]. They tested those algorithms on an image data set [CF03]; the experimental results are shown in Figure 2.2. The general Gray-World algorithm perform the best in the image of the top row, while the Gray-Edge does in the middle, and so does the 2nd-Order Gray-Edge in the bottom row. Gisenij et al. [GG07] adaptively used those algorithms with respect to the natural image statistics. The Weibull distribution is used to parameterize

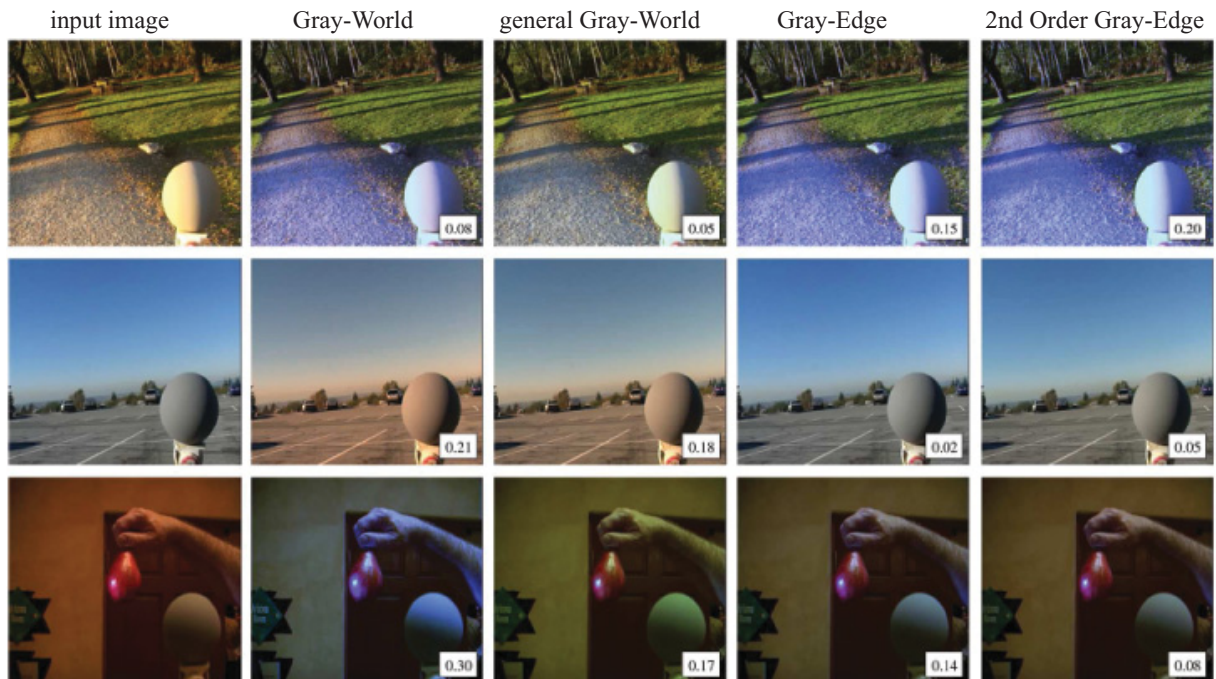


Figure 2.2: The comparison between the state-of-the-art color constancy algorithms [vdWGG07]: the Gray-World, the general Gray-World, and the Gray-Edge algorithms. The gray spheres exhibit the ground truths of the illumination color. The angular error between the estimated and the ground truth is indicated by the number in the right bottom corner. They still have difficulties when the scene includes few surface colors, or the scene is dominated by a single color.

the image and decide which algorithm to use. Those methods [Buc80, Lan77, FT04, vdWGG07, GG07] are simple and easy to implement, though they still have difficulties when the scene includes few surface colors, or the scene is dominated by a single color.

Several methods are proposed that calculate illumination invariant values. Illumination invariant is the key idea for color constancy itself, so that the methods can be applied to object recognition under varying illumination conditions. Land et al. [LM71] first introduced an idea to use reflectance edges for invariant features. Researchers such as Nayar et al. [NB93] and Geusebroek et al. [GBSG02, GBSG03] utilized the idea for object recognition and color constancy. Independently, but at the same time, Finlayson et al. [FH01] and Marchant et al. [MO00, MO01, MO02] introduced an idea to calculate the invariant values by assuming that blackbody radiation approximates the illumination color. Blackbody radiation is the energy emitted from a heated blackbody. Those methods can calculate the invariant features of objects, though they cannot estimate

surface/illumination colors.

Surface/illumination color separation is also studied in the spectral imaging research area. Maloney and Wandell [MW92] proposed to use a small number of basis functions to approximate the spectral function. They revealed that with two-dimensional surface reflectance, we can calculate all the unknown parameters that characterize the spectral functions by sampling at different spatial locations with three-dimensional sensors. Normal RGB image sensors are supposed to be used in the work; however, they would produce large errors with real images since the two-dimensional reflectance model is too strict. However, the idea can be extended for spectral imaging that has numerous sensors; the dimension of reflectance and illumination can be increased. Thus, this elegant idea has been extended to many spectral imaging methods up to this time [D'Z92, OH94, CH04, DF07, CH07].

Methods based on a varying illumination color were introduced by a few researchers [D'Z92, OH94, FFB95, BFF97]. They considered that the change of illumination color could be a key to solving the color constancy problem. D'Zmura [D'Z92] proposed a method using approximated linear basis functions to form a closed-form equation. One drawback of the method is that it fails to provide robust estimations for real images, since many objects' reflectance cannot be expressed by the linear combination of a small number of basis functions. Ohta et al. [OH94] stabilized the estimation based on D'Zmura's assumption and CIE Daylight constraint.

Finlayson et al. [FFB95] used a single surface color illuminated by two different illumination colors and performed the estimation by assuming that the illumination colors form a line in an inverse-chromaticity space. Barnard et al. [BFF97] utilized the Retinex algorithm [LM71] to automatically obtain a surface color with different illumination colors, and then applied the aforementioned method of Finlayson et al. [FFB95] to estimate varying illumination colors in a scene.

To summarize those works, surface color estimation of diffuse objects still has room for improvement in terms of accuracy and robustness, especially for a single-colored object. To handle single-colored objects, it is straightforward to take multiple illumination colors into account for solving the problem. Assuming a specific illumination color model would make the problem easier and could make the estimation robust.

### 2.1.2 Blackbody Illumination

Several researchers reported that blackbody radiation can predict the general shape of daylight illumination [FS01, JMW64]. The author has reviewed studies of daylight spectra measured in several countries: America, England, Canada, South Africa, Australia, India and Spain. This paper concludes that blackbody radiation could be a good model representing daylight illumination colors around the world.

In the middle 1960s, Judd et al. [JMW64] collected 249 daylight spectral samples from Rochester, New York, 274 from Enfield, England, and 99 from Ottawa, Canada, to calculate the characteristics of daylight spectra. The collected data were plotted in the 1931 CIE chromaticity diagram, a color space that created by the International Commission on Illumination (CIE) in 1931. Judd et al.'s data are shown in Fig. 2.3 (a); Rochester, Enfield, and Ottawa are indicated by open circles, by crosses, and by solid circles. The horizontal and vertical axes correspond to  $X/(X + Y + Z)$  and  $Y/(X + Y + Z)$ , where  $X, Y, Z$  are tri-stimulus values which are roughly red, green and blue, based on human visual perception. The red dotted line is added by the author to emphasize the locus of chromaticities implied by Planck's blackbody radiation law. As Fig.2.3 (a) shows, daylight spectra clustered very closely around the locus.

Slightly before Judd et al., Nayatani and Wyszecki [NW63] measured the colors of daylight from a near-north sky at Ottawa, Canada. The measured colors plotted in the chromaticity diagram are shown in Fig. 2.3 (b). As in (a), daylight illumination colors make a cluster around the Planckian locus. Figs. 2.3 (c) and (d) present the data in South Africa and Australia obtained by Winch et al. [WBKT66] and Dixon [Dix78], respectively. In the Southern Hemisphere, daylight colors are even closer to the Planckian locus compared to that of the Northern Hemisphere.

Sasturi et al. [SD68] measured daylight spectra in Pretoria, India; their data are shown in Fig 2.4 (a). In this work, they measured the lights from the north sky that were reflected by an aluminized mirror. Usually, a magnesium oxide or barium sulfate surface is used instead of measuring a reflection of a mirror, since the light from a mirror covers very narrow field-of-view of the sky. This would be the reason why their data are so widely distributed. Hernandez-Andres et al. [HARN01] purposely measured narrow-field-of-view light in Granada, Spain, which is shown in Fig 2.4 (b). The colors are widely distributed, particularly in the bluer region. However, the colors are dominantly spread very close to the Planckian locus.

As can be observed, the Planckian locus could approximate daylight well in most places of the world, though there are slight variances. The variances may come from

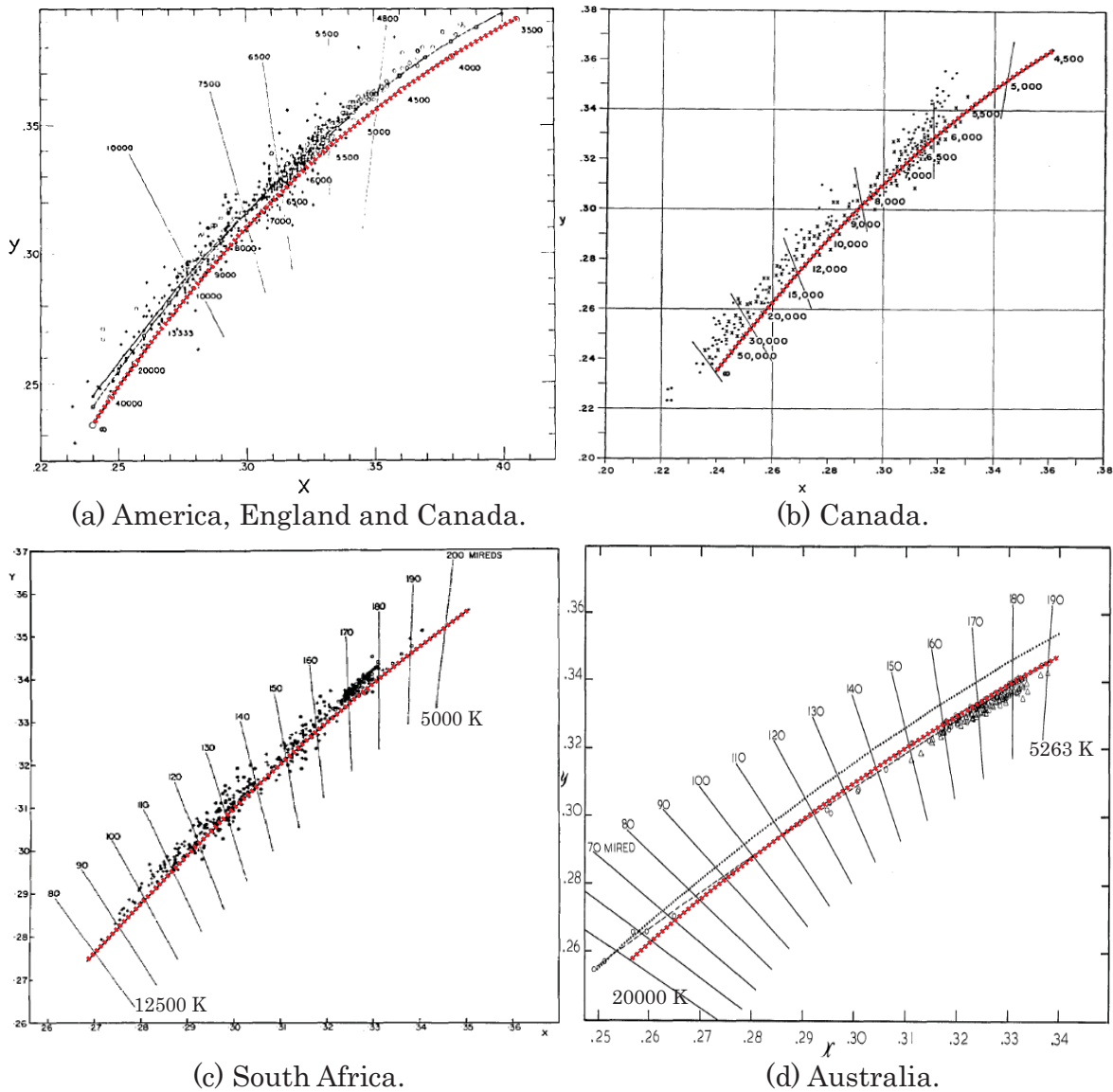


Figure 2.3: Daylight spectra plotted in the 1931 CIE chromaticity diagram, obtained in the following: (a) America, England and Canada [JMW64], (b) Canada [NW63], (c) South Africa [WBKT66] and (d) Australia [Dix78]. The red dotted curves indicate the locus of chromaticities implied by Planck's blackbody radiation law. The Planckian locus could approximate daylight colors well in most places of the world.

the different atmospheric condition, but also the region of the sky measured. An integrating sphere was used for Figs. 2.3 (c) and (d), a white plate was used for (a) and (b), while an aluminized mirror was used in Fig. 2.4 (a). Direct measurement within 3-degree fields of view was conducted in Fig. 2.4 (b). These findings mean that

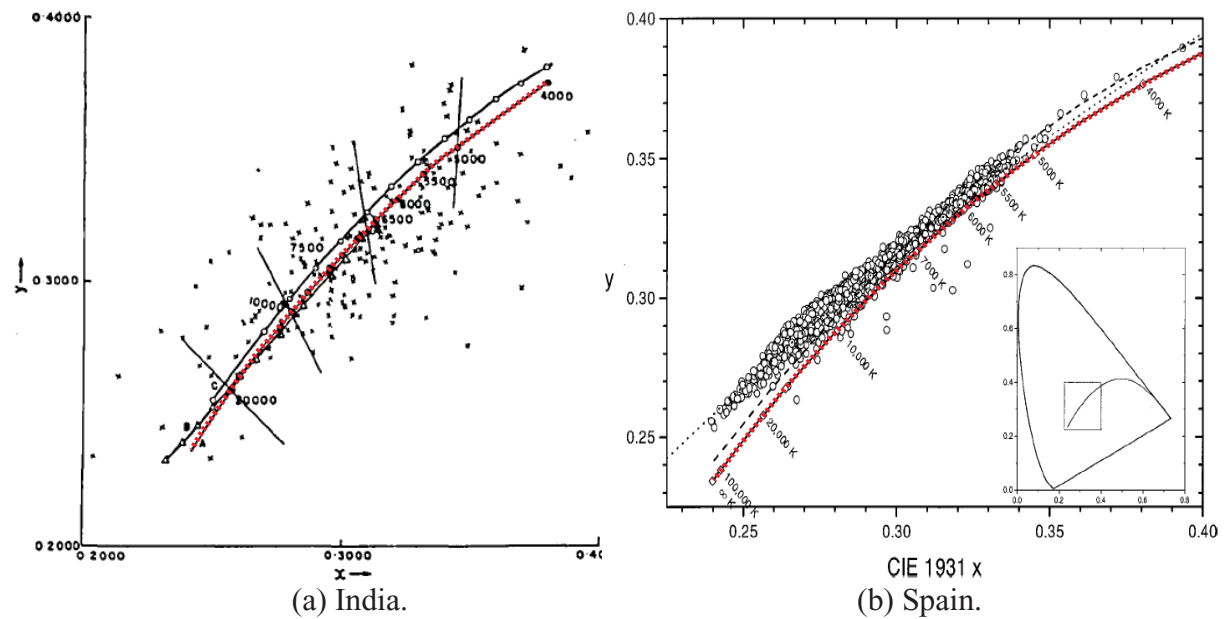


Figure 2.4: Daylight spectra obtained with a narrow field-of-view apparatus, plotted in the 1931 CIE chromaticity diagram: (a) India [SD68], (b) Spain [HARN01]. The red dotted curves indicate the Planckian locus.

lights from a specific part of the sky were measured in Figs. 2.4 (a), (b), 2.3 (a) and (b), while the lights that integrated in a sphere (lights that come from all directions) were measured in 2.3 (c) and (d). In terms of diffuse objects, the lights that come from all directions matter. Thus, Figs. 2.3 (c) and (d) are the data that attract our interest. In Figs. 2.3 (c) and (d), the Planckian locus describes the daylight colors very well. The apparatus difference also relates to the wide range of temperatures in Figs. 2.4 (a), (b), 2.3 (a) and (b), but not in 2.3 (c) and (d).

## 2.2 General Problem Formulation

Colors perceived by humans or camera sensors are light intensities that are emitted from a light source, reflected by an object surface, and filtered by color sensors. Surface color estimation is an inverse process of these, i.e., we estimate surface and illumination properties from a filtered color. This paper defines the problem as the separation of an image's chromaticity  $i_c$  into surface and illumination chromaticities  $s_c$  and  $e_c$ , using the following equation;

$$i_c = s_c e_c \quad c = \{r, g\}. \quad (2.1)$$

Chromaticity is defined as a ratio of  $R$  and  $G$  values to  $B$  value;

$$i_r = \frac{I_R}{I_B}, \quad i_g = \frac{I_G}{I_B}. \quad (2.2)$$

Eq. (2.1) holds by using this definition. We use the notation  $r, g$  for chromaticities and  $R, G, B$  for intensities to distinguish them simply.

Eq. (2.1) is derived by assuming a narrow-band camera model and converting intensities into chromaticities defined by Eq. (2.2). Details are as follows. Image intensities of diffuse objects taken by a digital color camera can be described as Eq. (2.3);

$$I_c = \tau \int_{\Omega} S(\lambda)E(\lambda)q_c(\lambda)d\lambda \quad c = \{R, G, B\} \quad (2.3)$$

$$\simeq \tau S_c E_c \quad (S_c = S(\lambda_c), E_c = E(\lambda_c)) \quad (2.4)$$

where  $S(\lambda)$  is a surface spectral reflectance and  $E(\lambda)$  is an illumination spectral power distribution.  $q_c(\lambda)$  is a camera-sensor sensitivity, where index  $c$  stands for the type of sensors ( $R, G$ , and  $B$ ). The integration is done over the visible spectrum ( $\Omega$ ).  $\tau$  is a gain determined by the aperture, the integration time, and the electronic amplification.

Then, we introduce a narrow-band camera model, which assumes that each color sensor has all its sensitivity concentrated on a single wavelength  $\lambda_c$ . That is, each sensitivity is approximated by a Dirac's delta function  $\delta(\cdot)$  whose center wavelength is  $\lambda_c$ . Therefore,  $q_c(\lambda) \simeq \delta(\lambda - \lambda_c)$  and we can subsequently obtain Eq. (2.4).  $\lambda_R, \lambda_G, \lambda_B$  are the wavelengths on which the sensitivities are concentrated.

Surface color estimation focuses on recovering chromaticities instead of intensities. This is because there is a scale ambiguity between surface spectral reflectance and illumination spectral power distribution. We cannot distinguish a dark surface with bright illumination from a bright surface with dark illumination. Thus, we convert the intensity space to the chromaticity space by substituting Eq. (2.4) into Eq. (2.2), and obtain Eq. (2.1). The surface chromaticity  $[S_R/S_B, S_G/S_B]^t$  is rewritten as  $[s_r, s_g]^t$ , and the same is true for the illumination chromaticity.

## 2.3 Illumination Chromaticity Formulation

This paper assumes that most illumination spectra can be approximated by blackbody radiation. The assumption is useful since an illumination chromaticity, that is a two-dimensional vector, becomes a function of a single scalar, temperature  $T$ . The scalar  $T$  is often called color temperature for representing the color.

In a mathematical form, an illumination chromaticity can be expressed as:

$$e_r(T) = \frac{M(\lambda_R, T)}{M(\lambda_B, T)}, \quad e_g(T) = \frac{M(\lambda_G, T)}{M(\lambda_B, T)} \quad (2.5)$$

where  $e = [e_r(T), e_g(T)]^t$  is an illumination chromaticity,  $M(\lambda_*, T)$  is the spectral power of the blackbody radiation,  $T$  is temperature in kelvin, and  $\lambda_R, \lambda_G, \lambda_B$  are the center wavelengths of a camera sensitivity. The narrow-band assumption and the chromaticity definition of Eq. (2.2) are used to derive the last equation.

From Planck's formula,  $M(\lambda, T)$  is:

$$M(\lambda, T) = c_1 \lambda^{-5} [\exp(c_2/\lambda T) - 1]^{-1} \quad (2.6)$$

where  $c_1$  is  $3.7418 \times 10^{-16}$  ( $\text{Wm}^2$ ),  $c_2$  is  $1.4388 \times 10^{-2}$  (mK), and  $\lambda$  is the wavelength (m). Substituting Eq. (3.28) into Eq. (2.5), we obtain:

$$e_r(T') = k_r \frac{\Phi_B(T')}{\Phi_R(T')} \quad \left( k_r = \frac{\lambda_B^5}{\lambda_R^5} \right) \quad (2.7)$$

$$e_g(T') = k_g \frac{\Phi_B(T')}{\Phi_G(T')} \quad \left( k_g = \frac{\lambda_B^5}{\lambda_G^5} \right) \quad (2.8)$$

where  $T' = c_2/T$ , and  $\Phi_*(T')$  are defined as follows for simplicity.

$$\begin{aligned} \Phi_R(T') &= \exp(T'/\lambda_R) - 1 \\ \Phi_G(T') &= \exp(T'/\lambda_G) - 1 \\ \Phi_B(T') &= \exp(T'/\lambda_B) - 1 \end{aligned} \quad (2.9)$$

## 2.4 Our Problem Formulation

The difference between our approach and conventional approaches is using the exact blackbody radiation for the model of illumination colors. Consequently, the surface-color estimation problem becomes equivalent to estimating a color temperature  $T$ . Eq. (2.1) shows the interdependency between surface and illumination chromaticities. Also, an illumination chromaticity can be parameterized by the color temperature  $T$  as Eqs. (2.7) and (2.8) show. Thus, when the color temperature  $T$  is known, the illumination chromaticity and then the surface chromaticity can be calculated explicitly.

The equations to solve can be established as follows. When we observe a surface chromaticity  $s$  under two blackbody illuminations  $e(T_1)$  and  $e(T_2)$ , we can estimate each color temperature  $T_1$  and  $T_2$  from obtained colors  $i_1$  and  $i_2$  (Fig. 2.5). Let the two image

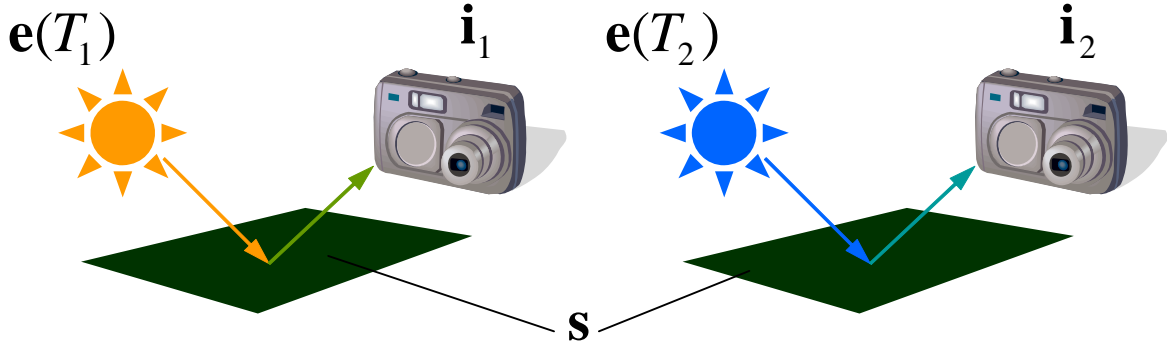


Figure 2.5: Illustration of notations. Color temperatures  $T_1$  and  $T_2$  are estimated from image chromaticities  $i_1$  and  $i_2$  taken under two blackbody illumination. Consequently, surface chromaticity  $s$  can be calculated.

chromaticities be  $i_1 = [i_{r1}, i_{g1}]^t$  and  $i_2 = [i_{r2}, i_{g2}]^t$ . We can derive the following equations, since the surface chromaticity is identical:

$$\Theta_r(T'_1, T'_2) = i_{r1}\Phi_R(T'_1)\Phi_B(T'_2) - i_{r2}\Phi_R(T'_2)\Phi_B(T'_1) = 0 \quad (2.10)$$

$$\Theta_g(T'_1, T'_2) = i_{g1}\Phi_G(T'_1)\Phi_B(T'_2) - i_{g2}\Phi_G(T'_2)\Phi_B(T'_1) = 0 \quad (2.11)$$

Surface-color estimation will be solved if  $T'_1$  and  $T'_2$  are specified from those equations.

Detailed derivations of Eqs. (2.10) and (2.11) are as follows. Since the surface chromaticity is identical, the following equations can be derived from Eq. (2.1):

$$i_{r1}/e_{r1} - i_{r2}/e_{r2} = 0 \quad (2.12)$$

$$i_{g1}/e_{g1} - i_{g2}/e_{g2} = 0 \quad (2.13)$$

while Eqs. (2.7) and (2.8) can be converted as follows:

$$1/e_r = \Phi_R(T')/k_r\Phi_B(T') \quad (2.14)$$

$$1/e_g = \Phi_G(T')/k_g\Phi_B(T') \quad (2.15)$$

By substituting Eqs. (2.14) and (2.15) into Eqs. (2.12) and (2.13), Eqs. (2.10) and (2.11) are obtained.

## 2.5 Solutions

We propose a stable method using bracketing [PFTV88], since Eqs. (2.10) and (2.11) are difficult to solve by minimizing the square sum of Eqs. (2.10) and (2.11). This is due

to the exponential character of the functions in those equations. The overview of the algorithm is as follows.

1. First, we select the initial values of  $T'_1$  and  $T'_2$ . We denote them as  $t'_1$  and  $t'_2$ .
2. Assuming that  $t'_1$  is correct, we solve Eqs. (2.10) and (2.11) independently using bracketing. Let the solutions be  $t'_{2r}$  and  $t'_{2g}$ .
3. If  $t'_{2r}$  and  $t'_{2g}$  are sufficiently similar to each other, we output  $t'_1$  and  $(t'_{2r} + t'_{2g})/2$ .
4. Otherwise, we modify  $t'_1$  so that the difference between  $t'_{2r}$  and  $t'_{2g}$  decreases. Again,  $t'_1$  can be found using bracketing.
5. Go back to 2.

In order to realize the above algorithm, we must clarify the two following points:

- How to solve Eqs. (2.10) and (2.11),
- How to determine  $t'_1$  that decreases the difference between  $t'_{2r}$  and  $t'_{2g}$ ,

using bracketing technique.

### Bracketing for Step2

The following shows how to solve Eq. (2.10). The same argument can be applied to Eq. (2.11). Given an arbitrary  $T'_1$ , Eq. (2.10) has a unique solution of  $T'_2$  on  $T'_2 > 0$  (under the condition described below.) The solutions can be calculated by bracketing. The initial brackets are automatically determined. They are derived from the shape of the evaluation function  $\Theta_r$ , which is illustrated in Figure 2.6. As the figure shows,  $\Theta_r$  is convex downward and has only one local minimum. It starts from zero and gradually approaches infinity. Therefore, a solution of  $T'_2$  always exists and can be calculated by bracketing. We can randomly select one side of the initial brackets, and find the other side by going up or down the slope until the sign of  $\Theta_r$  changes.

The shape of  $\Theta_*$  and the conditions for which those equations have solutions, are derived from the following propositions.

1. If  $T'_1$  is positive, the function  $\Theta_*$  is convex downward.
2.  $\Theta_*(T'_1, 0)$  is zero for any  $T'_1$ .

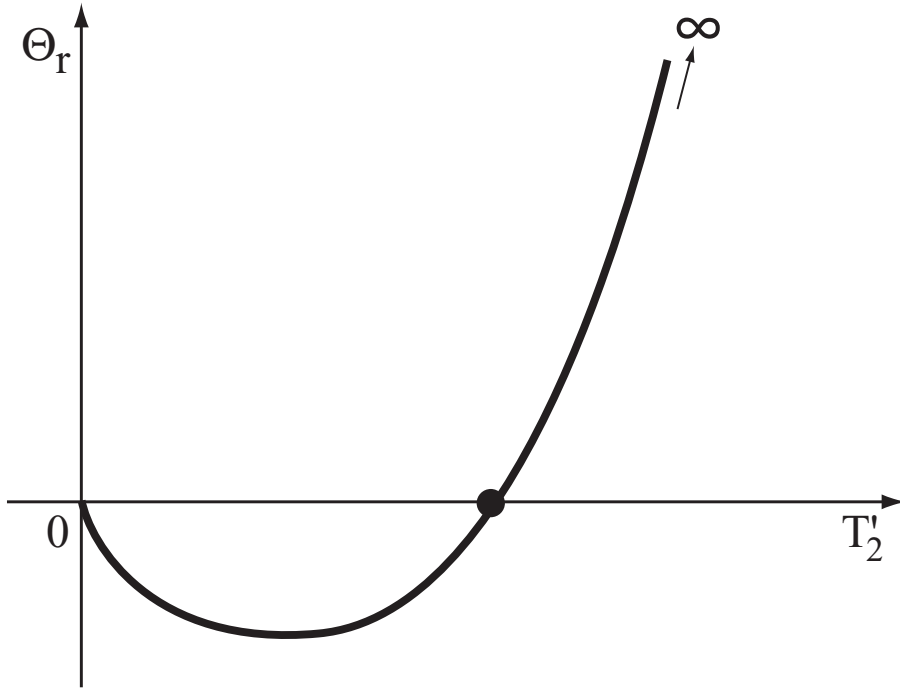


Figure 2.6: The shape of the evaluation function  $\Theta_r$ , given an arbitrary  $T'_1$ .  $T'_2$  that gives  $\Theta_r = 0$  always exists and can be calculated by bracketing. We let the initial value of  $t'_2$  be one side of the brackets, and find the other side by going up or down the slope until the sign of  $\Theta_r$  changes.

3. If  $T'_1$  is positive,  $\lim_{T'_2 \rightarrow \infty} \Theta_*(T'_1, T'_2) = +\infty$ .

4. If  $T'_1$  is positive,  $\Theta_r = 0$  has solutions on  $T'_2 > 0$ , if and only if

$$i_{r2}\Phi_B(T'_1)/\lambda_R - i_{r1}\Phi_R(T'_1)/\lambda_B > 0. \quad (2.16)$$

Similarly,  $\Theta_g = 0$  has solutions on  $T'_2 > 0$ , if and only if

$$i_{g2}\Phi_B(T'_1)/\lambda_G - i_{g1}\Phi_G(T'_1)/\lambda_B > 0.$$

Brief proofs of those propositions are as follows.

Proof of Proposition 1.

We show that the second derivative of  $\Theta_r$  is positive at the extremum?D We used  $\Theta_r$  for the proof, but the same argument can be done by using  $\Theta_g$ . We differentiate  $\Theta_r$  by  $T'_2$ .

$$\frac{\partial \Theta_r}{\partial T'_2} = \frac{i_{r1}}{\lambda_B} \Phi_R(T'_1) \exp(T'_2/\lambda_B) - \frac{i_{r2}}{\lambda_R} \exp(T'_2/\lambda_R) \Phi_B(T'_1)$$

From the last equation,  $T'_2$  which gives the extremum can be calculated.

$$T'_2 = \frac{\lambda_R \lambda_B}{\lambda_R - \lambda_B} \left( \log\left(\frac{i_{r2}}{\lambda_R} \Phi_B(T'_1)\right) - \log\left(\frac{i_{r1}}{\lambda_B} \Phi_R(T'_1)\right) \right) \quad (2.17)$$

According to the last equation,  $\Theta_r$  has a unique extremum. From the continuity of  $\Theta_r$  as well as  $\partial \Theta_r / \partial T'_2$ ,  $\Theta_r$  is convex upward or convex downward. We further differentiate  $\Theta_r$  by  $T'_2$ .

$$\frac{\partial^2 \Theta_r}{\partial T'^2_2} = \left( \frac{1}{\lambda_B} - \frac{1}{\lambda_R} \right) \frac{i_{r1}}{\lambda_B} \Phi_R(T'_1) \exp(T'_2/\lambda_B) + \frac{i_{r1}}{\lambda_B} \frac{\partial \Theta_r}{\partial T'_2}$$

Since  $\partial \Theta_r / \partial T'_2$  is zero at the extremum,

$$\frac{\partial^2 \Theta_r}{\partial T'^2_2} = \left( \frac{1}{\lambda_B} - \frac{1}{\lambda_R} \right) \frac{i_{r1}}{\lambda_B} \Phi_R(T'_1) \exp(T'_2/\lambda_B)$$

The last equation is positive because  $\lambda_B < \lambda_R$ . Thus,  $\Theta_r$  is convex downward. Q.E.D.

Proposition 2.

Trivial. Q.E.D.

Proposition 3.

Trivial. Q.E.D.

Proof of Proposition 4.

We prove only the former part, but the latter can be proved similarly. From Prop.1,  $\Theta_r$  is convex downward. That is, the equation possibly has two solutions at most. One of those solutions is zero because of Prop.2. Consequently, a solution on  $T'_2 > 0$  exists if the local minimum of  $\Theta_r$  exists on  $T'_2 > 0$ . Such a condition can be written as Eq. (2.16) from Eq. (2.17). A solution on  $T'_2 > 0$  certainly exists from Prop.3. Q.E.D.

### Bracketing for Step 4

Let us show how to determine  $t'_1$  that decreases the difference between  $t'_{2r}$  and  $t'_{2g}$ . If  $t'_1$  increases/decreases,  $t'_{2r} - t'_{2g}$  increases/decreases around the true solution as illustrated in Figure 2.7. Therefore, again we can calculate the solutions by bracketing. The facts are derived from the following proposition:

5. Let the true solutions be  $\hat{T}'_1$  and  $\hat{T}'_2$  for Eqs. (2.10) and (2.11). If  $T'_1$  increases/decreases around them,  $T'_{2r} - T'_{2g}$  increases/decreases as long as  $\hat{T}'_1 > \hat{T}'_2$ .

In order to automatically determine the initial brackets, we need to clarify the shape of the function where it crosses the zero point. The Taylor expansion of Eqs. (2.10) and (2.11) are used for this purpose. Detailed derivation of Proposition 5 is as follows.

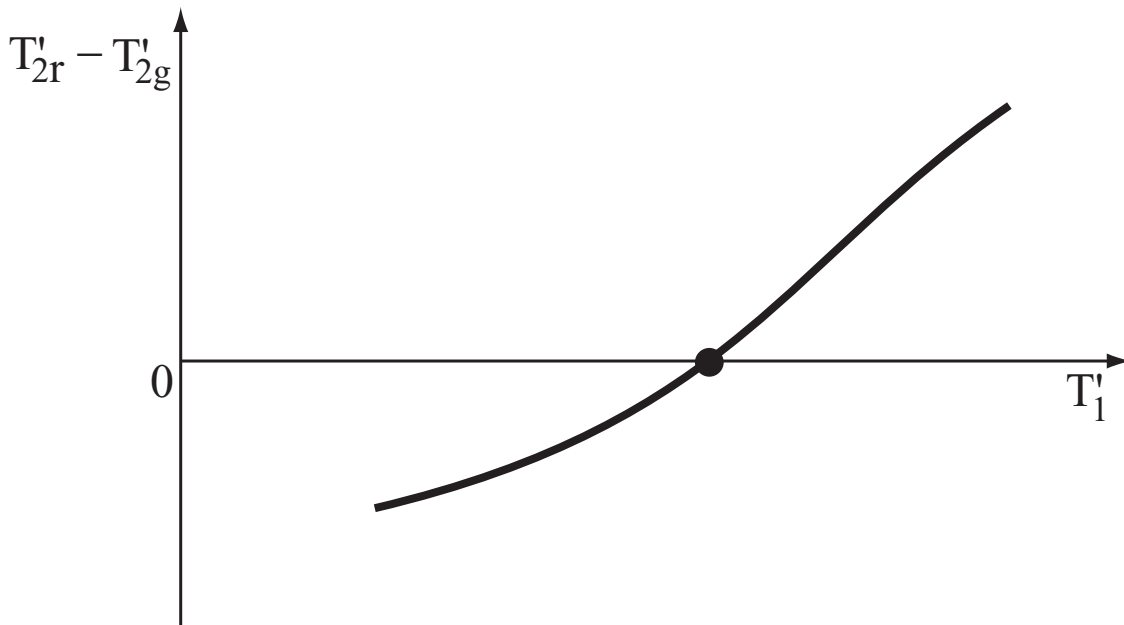


Figure 2.7: The shape of  $T'_{2r} - T'_{2g}$  around the true solution. If  $T'_1$  increases/decreases,  $T'_{2r} - T'_{2g}$  increases/decreases. Therefore, the solution can be calculated by bracketing.

Derivation of Proposition 5. We derive the Taylor series of  $\Theta_r$  about a point  $(t'_1, t'_{2r})$ ,

$$\Theta_r = \Theta_r(t'_1, t'_{2r}) + \left( \frac{i_{r1}\Phi_B(t'_{2r})}{\lambda_R} \exp\left(\frac{t'_1}{\lambda_R}\right) - \frac{i_{r2}\Phi_R(t'_{2r})}{\lambda_B} \exp\left(\frac{t'_1}{\lambda_B}\right) \right) \Delta t'_1 \\ + \left( \frac{i_{r1}\Phi_R(t'_1)}{\lambda_B} \exp\left(\frac{t'_{2r}}{\lambda_B}\right) - \frac{i_{r2}\Phi_B(t'_1)}{\lambda_R} \exp\left(\frac{t'_{2r}}{\lambda_R}\right) \right) \Delta t'_{2r}$$

where  $\Delta t'_1 = T'_1 - t'_1$ ,  $\Delta t'_{2r} = T'_{2r} - t'_{2r}$ . We can simplify the last equation using Eq. (2.10),

$$\Theta_r = i_{r1}\Phi_R(t'_1)\Phi_B(t'_{2r})(H_r(t'_1)\Delta t'_1 - H_r(t'_{2r})\Delta t'_{2r}) \quad (2.18)$$

where

$$H_r(t) = \frac{\exp(t/\lambda_R)}{\lambda_R\Phi_R(t)} - \frac{\exp(t/\lambda_B)}{\lambda_B\Phi_B(t)}.$$

In a similar way, we derive the Taylor series of  $\Theta_g$  about another point  $(t'_1, t'_{2g})$ .

$$\Theta_g = i_{g1}\Phi_G(t'_1)\Phi_B(t'_{2g})(H_g(t'_1)\Delta t'_1 - H_g(t'_{2g})\Delta t'_{2g}) \quad (2.19)$$

From the last two equations,  $T'_{2r} - T'_{2g}$  against  $\Delta t'_1$  can be expressed as:

$$T'_{2r} - T'_{2g} = \left( \frac{H_r(t'_1)}{H_r(t'_{2r})} - \frac{H_g(t'_1)}{H_g(t'_{2g})} \right) \Delta t'_1 + (t'_{2r} - t'_{2g})$$

Around the true solutions  $\hat{T}'_1, \hat{T}'_2$ , the last equation becomes

$$T'_{2r} - T'_{2g} = \left( \frac{H_r(\hat{T}'_1)}{H_r(\hat{T}'_2)} - \frac{H_g(\hat{T}'_1)}{H_g(\hat{T}'_2)} \right) \Delta t'_1. \quad (2.20)$$

The following function

$$I(T'_1, T'_2) = H_r(T'_1)H_g(T'_2) - H_g(T'_1)H_r(T'_2) \quad (2.21)$$

is obviously  $I(T'_1, T'_2) = -I(T'_2, T'_1)$ . We confirmed that  $I(T'_1, T'_2)$  is positive if  $T'_1$  is larger than  $T'_2$  by calculating every case from 2000K to 10000K with a 1K interval. Thus,  $T'_{2r} - T'_{2g}$  is positive/negative if  $\Delta t'_1$  is positive/negative as long as  $\hat{T}'_1 > \hat{T}'_2$ .

## 2.6 Experiments

Experiments with simulation and real data have been conducted to evaluate the effectiveness of the method. Differing from what we expected, the results showed that although this method is a perfect vehicle for simulation data, it produces significant errors with real data. Thorough investigation of the cause of errors indicates how important the assumptions on both blackbody illuminations and narrow-band camera sensitivities are to the method.

### 2.6.1 Simulation Data

The effectiveness of the proposed method is evaluated with simulation data. In particular, we checked the two following points: (1) Average estimation error using simulation data. (2) Dependency on initial values.

The error was defined as the difference between estimated and true reciprocal color temperatures. Reciprocal color temperatures were proposed by Judd [Jud33], in which differences correspond more closely to equal perceptual color differences than normal color temperatures. The unit is called “mired” ( $= 10^6 K^{-1}$ ), and is defined as  $T^{\text{rec}} = 10^6/T$ . Empirically, the Just Noticeably Different (JND) chromaticity difference is 5.5 mired [TW02, Jud33]. The range from 2500 K to 8500 K in color temperatures corresponds to from 400 to 118 mired in reciprocal color temperatures.

**(1) Estimation error with simulation data** *Methods* We calculated the average estimation error using seven kinds of blackbody illuminants and six reflectance patches.

Seven color temperatures were 2500, 3500, 4500, 5500, 6500, 7500, and 10000 in Kelvin, which are shown in Figure 2.8 (a). Six reflectance patches were, as shown in Figure 2.8 (b), “Blue,” “Green,” “Red,” “Yellow,” “Magenta,” and “Cyan” in the GretagMacbeth ColorChecker, hereafter referred to as “Macbeth.” All the reflectance data were obtained by measuring the spectrum of a color patch with a spectrometer (Photo Research PR-650) under a known illuminant.

The total combination was  ${}^7C_2 \times 6 = 126$ . A camera sensitivity which is 1 at a particular wavelength (red: 624 nm, green: 548 nm, blue: 480 nm), and is 0 at others was used (shown in Figure 2.8 (c).)

*Results* The average estimation error was  $1.64 \times 10^{-5}$  mired for  $T_1$ , and  $1.74 \times 10^{-5}$  mired for  $T_2$  as shown in Table 2.1. The estimation by the previous method [FFB95] is

also shown for reference. The error converges to zero in all cases by using the proposed method.

Table 2.1: The average estimation error in 126 experiments using simulation data. The estimation error by the previous method [FFB95] is also shown for reference.

Method	$T_1$ Error		$T_2$ Error	
	(mired)	(CIE LAB)	(mired)	(CIE LAB)
Proposed method	$1.64 \times 10^{-5}$	0	$1.74 \times 10^{-5}$	0
Previous method [FFB95]	$5.11 \times 10$	8.5	$5.52 \times 10$	9.2

**(2) Dependency on initial values** *Methods* We did our estimation 500 times with different initial values but the same reflectance and illuminants and calculated the average and the standard deviation of estimation error.

The color temperatures of illuminants were 3500 and 7500 in Kelvin. We used “Red” reflectance of the Macbeth ColorChecker.

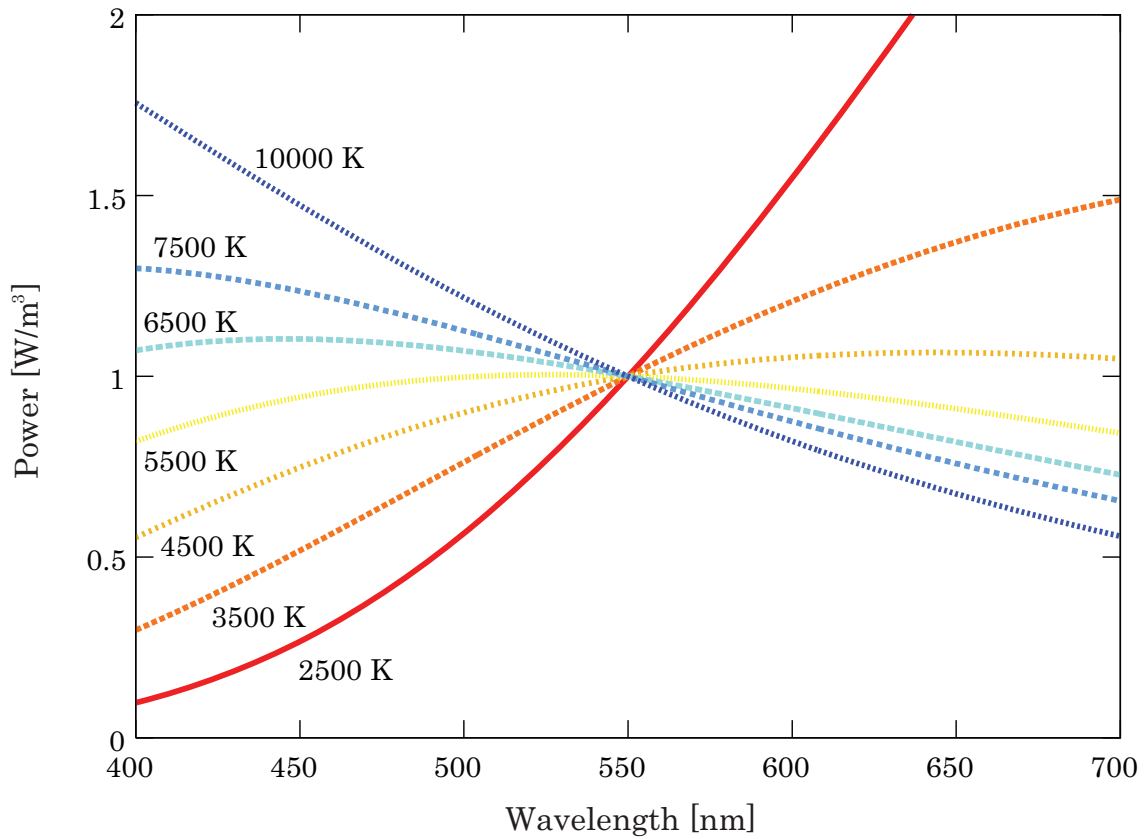
A camera sensitivity that is 1 at the wavelength (red: 624 nm, green: 548 nm, blue: 480 nm), and is 0 at others was used. Initial values were randomly and uniformly distributed over the range of the true temperature  $\pm 1000$  K.

*Results* The averages and the standard deviations of estimation error were  $3.53 \times 10^{-6}$  mired and  $2.18 \times 10^{-6}$  mired for  $T_1$ , and  $3.78 \times 10^{-6}$  mired and  $2.35 \times 10^{-6}$  mired for  $T_2$ , as shown in Table 2.2.

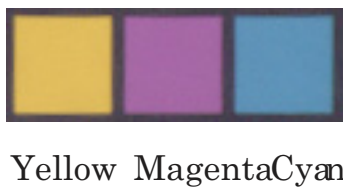
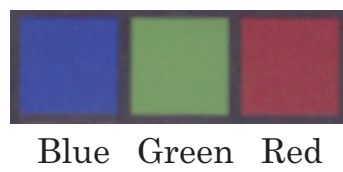
The standard deviation is nearly the estimation accuracy, which is about  $10^{-6}$  due to the machine accuracy. Therefore, we conclude that initial values do not affect the estimation. However, the result temperatures can be an impractical number such as 2 trillion Kelvin if the relation (for instance  $T_1 > T_2$ ) is reversed in the initial values ( $T_1 < T_2$ ). In other words, initial values can be any numbers if the relation between  $T_1$  and  $T_2$  is retained.

## 2.6.2 Real Data

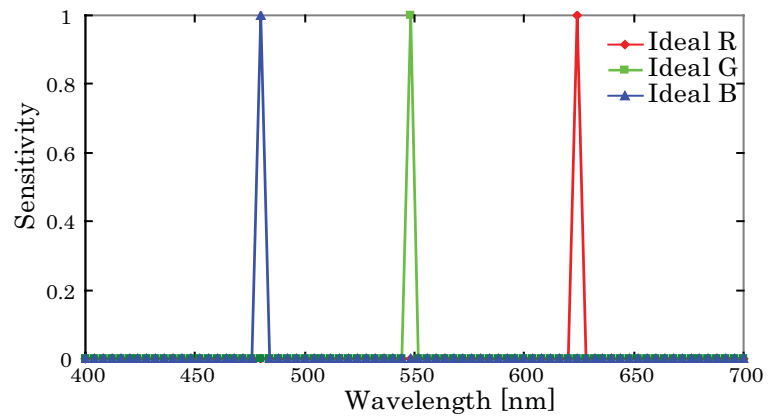
We conducted four sets of experiments to see if the method could work on real data. In the first set of experiments, we tested our algorithm with various kinds of natural illuminants and reflectances, and erroneous results were obtained.



(a) Spectra of ideal blackbody illuminants.



(b) Six reflectance patches.



(c) Ideal camera-sensor sensitivity.

Figure 2.8: Ideal data used in the experiments; (a) seven kinds of blackbody illuminants; corresponding color temperatures are 2500, 3500, 4500, 5500, 6500, 7500, and 10000 in Kelvin. (b) Six reflectance patches of GretagMacbeth ColorChecker used in the experiments. (c) Ideal camera sensitivity.

Table 2.2: The average and the standard deviation of estimation errors in 500 experiments with different initial values.

Parameter	$T_1$ Error (mired)	$T_2$ Error (mired)
Average	$3.53 \times 10^{-6}$	$3.78 \times 10^{-6}$
Std. dev	$2.18 \times 10^{-6}$	$2.35 \times 10^{-6}$

We presumed there are two causes of the error. One cause might have been the failure of the blackbody radiation to accurately portray the actual illuminants. To understand this problem, we conducted the second set of experiments and observed how the violation of the blackbody assumption affects the estimation. We also tested how different real spectra appear to blackbody radiations in the third set of experiments. The other cause of error must have been the violation of the narrow-band sensitivity assumption. We tested how it affects the estimation in the fourth set of experiments.

The following explains experiments that were conducted, and each focuses on: (1) Estimation error on experiments with real data. (2) Error caused by the assumption of blackbody illumination. (3) Difference between spectra of the blackbody radiation and real spectra. (4) Error caused by the assumption of narrow-band sensitivity.

**(1) Estimation error with real data** *Methods* We calculated the average estimation error using eight kinds of natural illuminants and six kinds of reflectance.

Eight illuminants were A, B, C of CIE standard illuminants and Judd daylight phases D48, D55, D65, D75 and D100 [JMW64]; they are shown in Figure 2.9 (a). Six reflectance were “Blue,” “Green,” “Red,” “Yellow,” “Magenta,” and “Cyan” of the Macbeth ColorChecker, which are shown in Figure 2.9 (b).

The total combination was  ${}_8C_2 \times 6 = 168$ . Band-pass filters, MellesGriot 03FIV119, 03FIV111, 03FIV004, were used for camera sensitivity. Their full-width at half-maximum was 10 nm, and their center wavelength were 620 nm, 532 nm, and 450 nm, for red, green and blue channels. They are shown in Figure 2.9 (c).

*Results* The average estimation error was  $3.67 \times 10^3$  mired for  $T_1$ , and  $1.17 \times 10^4$  mired for  $T_2$  as shown in Table 2.3. The erroneous results force us to think what the substantial causes of those errors are. As stated in the beginning of this subsection, there are two possible causes: the violations of the blackbody assumption and the

narrow-band sensitivity assumption. The following experiments investigate how the violations affect the estimation. We discuss the robustness of the method in Section 2.7.

Table 2.3: The average estimation error in 168 experiments using real data. The estimation error by the previous method [FFB95] is also shown for reference. 18 results of the previous method were excluded from the average CIE LAB error calculation, since those estimates include negative values.

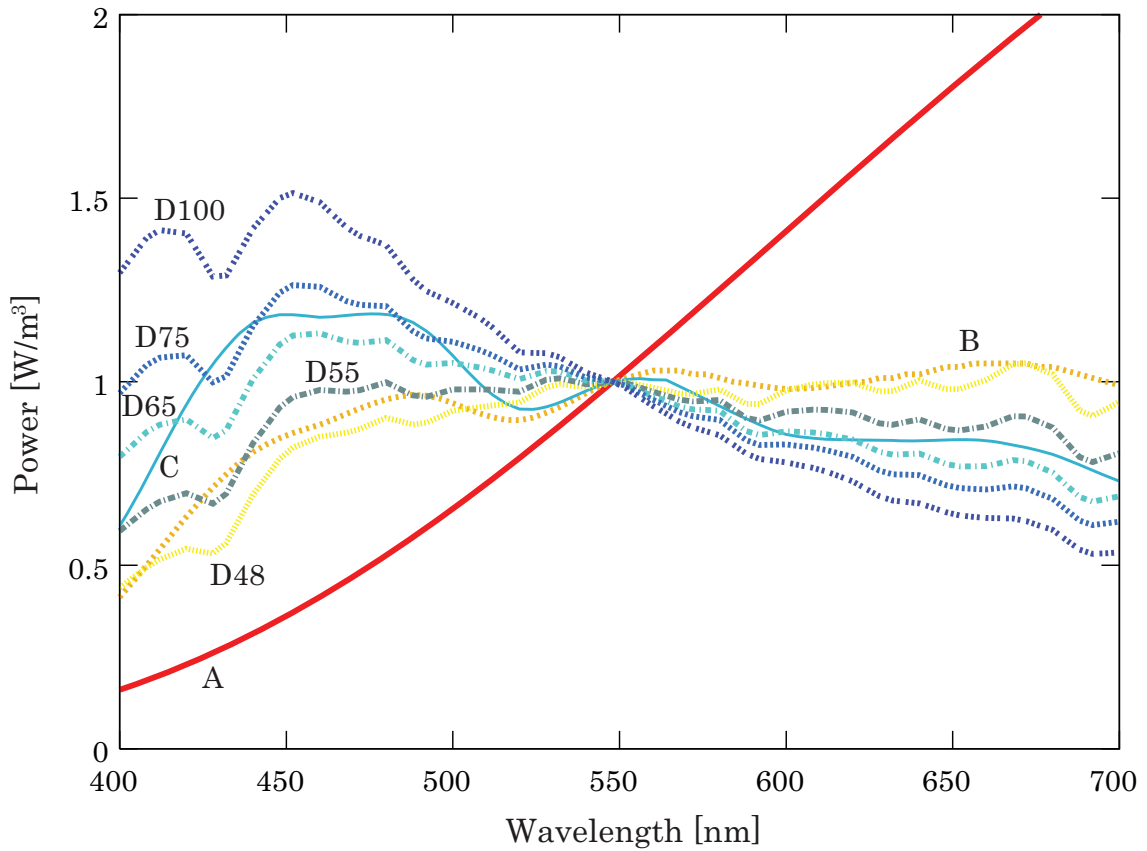
Method	$T_1$ Error		$T_2$ Error	
	(mired)	(CIE LAB)	(mired)	(CIE LAB)
Proposed method	$3.67 \times 10^3$	44.2	$1.17 \times 10^4$	42.0
Previous method [FFB95]	$7.97 \times 10$	17.0	$8.43 \times 10$	18.0

**(2) Error caused by the blackbody assumption** *Methods* We plotted the change of estimation error against the error on illumination chromaticity. Let  $\Delta e_r$  and  $\Delta e_g$  be the error on illumination chromaticity. One illumination chromaticity was chosen, and  $\Delta e_r$  and  $\Delta e_g$  were added to it.  $\Delta e_r$  and  $\Delta e_g$  were changed from 0 to 1 % by 0.1 %.

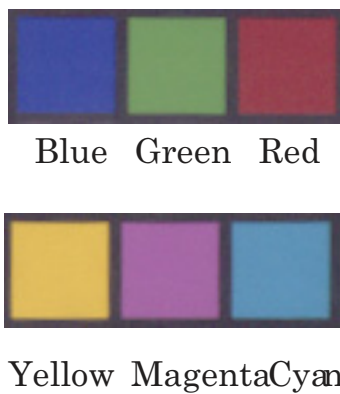
The illuminants' color temperatures were 3000 and 9000 in Kelvin. The reflectance used was "Dark skin," the top left brown reflectance of the Macbeth ColorChecker. Camera sensitivity is 1 at these wavelengths: red: 624 nm, green: 548 nm, blue: 480 nm, and is 0 at others.

*Results*  $\Delta T_1$  and  $\Delta T_2$  in Figure 2.10 show the estimation error  $\Delta T_1$  and  $\Delta T_2$  against the percentage of the modeling error  $\Delta e_r$  and  $\Delta e_g$  of illumination colors. The unit of the horizontal axis is %, and that of the vertical axis is mired. Figure 2.10 also shows the line of Just Noticeably Different chromaticity difference (5.5 mired). The figure shows that the modeling error should be under about 0.1% if we want the estimation error to be lower than 5.5 mired.

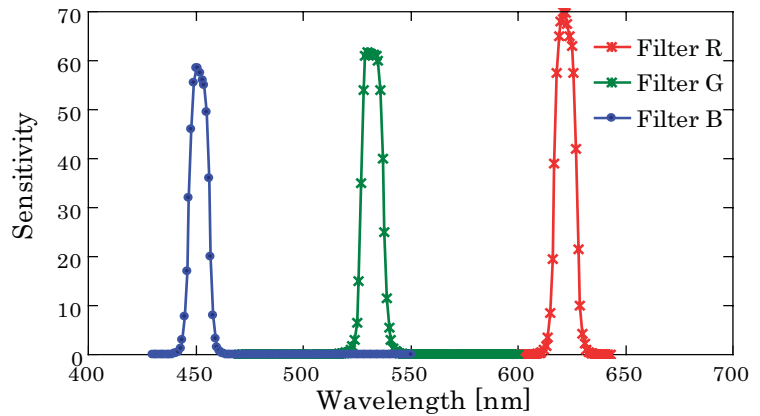
**(3) Difference between blackbody and real spectrum** *Methods* We calculated the difference between blackbody illuminants and spectra of the CIE standard illuminants (A,B,C) and Judd's daylight phases (D48, D55, D65, D75, D100). First, we searched the blackbody color temperature whose color is the nearest to the real illuminant. Then we calculated the color difference between the two. The value that represents the difference is defined as (chromaticity of the real illuminant – chromaticity of the searched color



(a) Spectra of real outdoor illuminants.

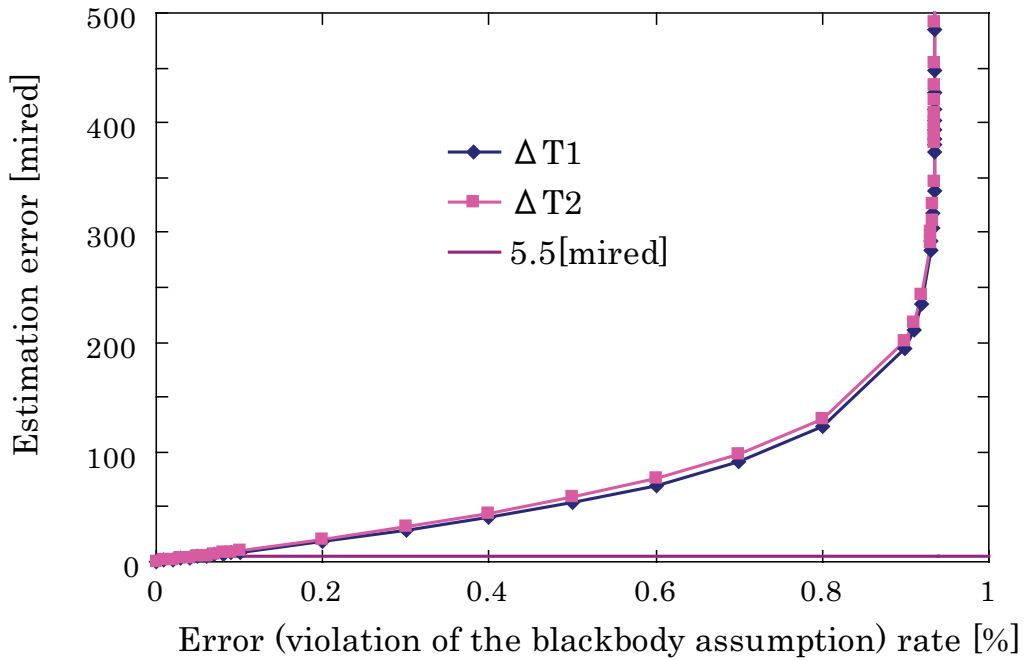


(b) Six reflectance patches.



(c) Camera-sensor sensitivity.

Figure 2.9: Real data used in the experiments; (a) eight illuminants' spectra: A, B, C of CIE standard illuminants and Judd daylight phases D48, D55, D65, D75 and D100. Note the difference between the data shown in Figure 2.8 (a). (b) Six reflectance patches. (c) Camera sensitivities. They are the sensitivities of band-pass filters: MellesGriot 03FIV119, 03FIV111, 03FIV004.




Zoomed view

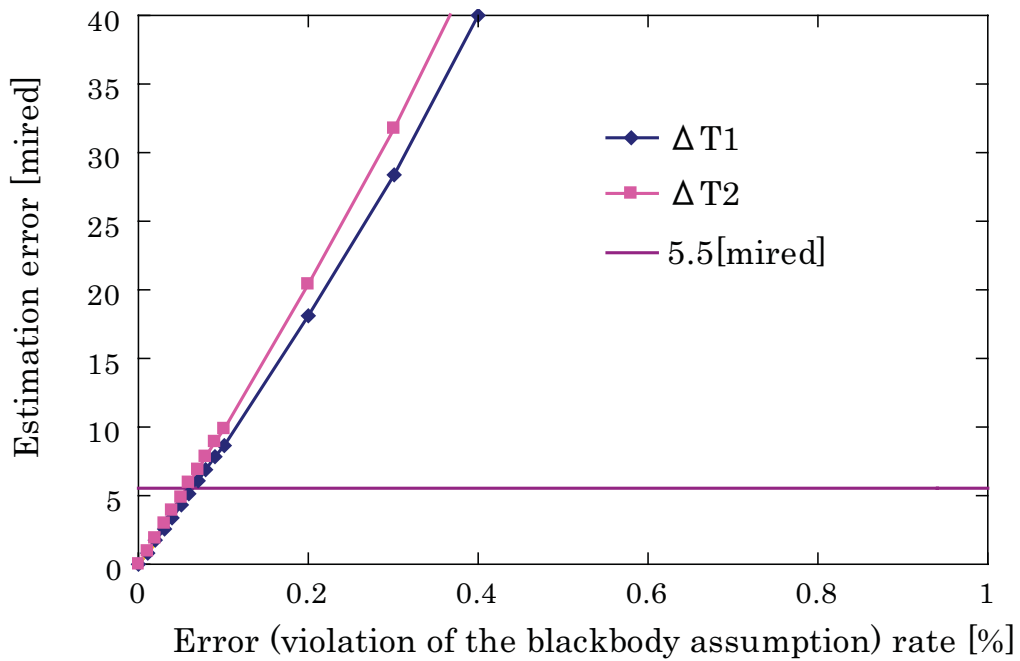


Figure 2.10: The plots of estimation error against the violation of the blackbody assumption; “ $\Delta T1$ ” and “ $\Delta T2$ ” express the estimation error. The JND chromaticity difference (5.5 mired) is also shown. In order to limit the estimation error to be lower than 5.5 mired, the violation should be under about 0.1 %.

temperature)/(chromaticity of the searched color temperature). The sensitivity which is 1 at 620 nm (red), 532 nm (green), 450 nm (blue) and 0 at others was used.

Results Table 2.4 shows the difference between the color of blackbody and real spectra. Except for CIE standard illumination A, all illumination has more than 0.1% difference. Therefore, the proposed method would produce significant errors when those illuminants are used.

Table 2.4: Difference between blackbody and real spectra.  $\Delta e_r$  and  $\Delta e_g$  are the error percentage of the illuminant's color to the nearest blackbody color. Note that the difference is defined in the color space of the sensitivity used in this experiment.

Illuminants	$\Delta e_r$ [%]	$\Delta e_g$ [%]	Nearest $T$ [K]
CIE A	0.0029	-0.0165	2856
CIE B	2.6368	-4.6126	5087
CIE C	5.5397	-6.1154	7451
Judd D48	-1.0788	2.0506	4818
Judd D55	-1.0617	1.6286	5584
Judd D65	-0.9358	1.1519	6698
Judd D75	-0.7690	0.8096	7842
Judd D100	-0.4606	0.3816	10852

**(4) Error caused by the narrow-band assumption** Methods We made a virtual sensitivity with variable bandwidth by using the Gaussian function as shown in Figure 2.11. The  $\sigma$  of the Gaussian function was the parameter to change the bandwidth. The center wavelengths were red: 620 nm, green: 532 nm, blue: 450 nm.

Color temperatures of illuminants were 4000 and 9000 in Kelvin. For the reflectance, we used "Dark skin," "Light skin," and "Green" of the Macbeth ColorChecker, which are shown in Figure 2.12 denoted by "Dark skin," "Light skin," and "Green."

Results Figure 2.13 shows the estimation error against the bandwidth of a camera sensitivity. The more the bandwidth (the standard deviation  $\sigma$  of a Gaussian function) grows, the larger the estimation error becomes. The speed of the error growth depends on reflectance. In the case of "Green" or "Light skin" reflectance, the estimation breaks

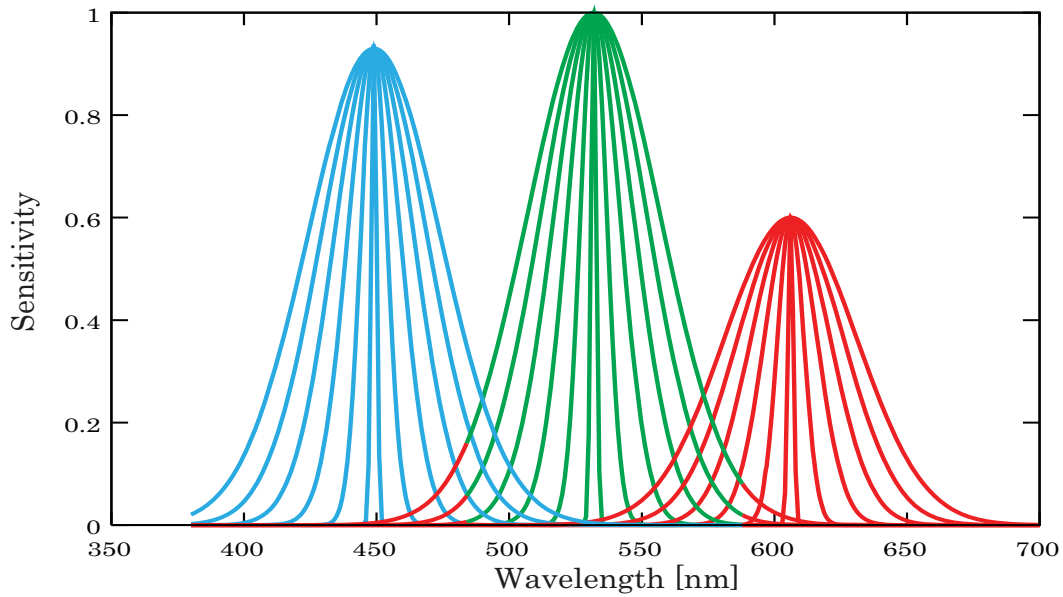


Figure 2.11: Virtual camera sensitivities. The standard deviation of Gaussian functions are changed from 1 nm to 20 nm.

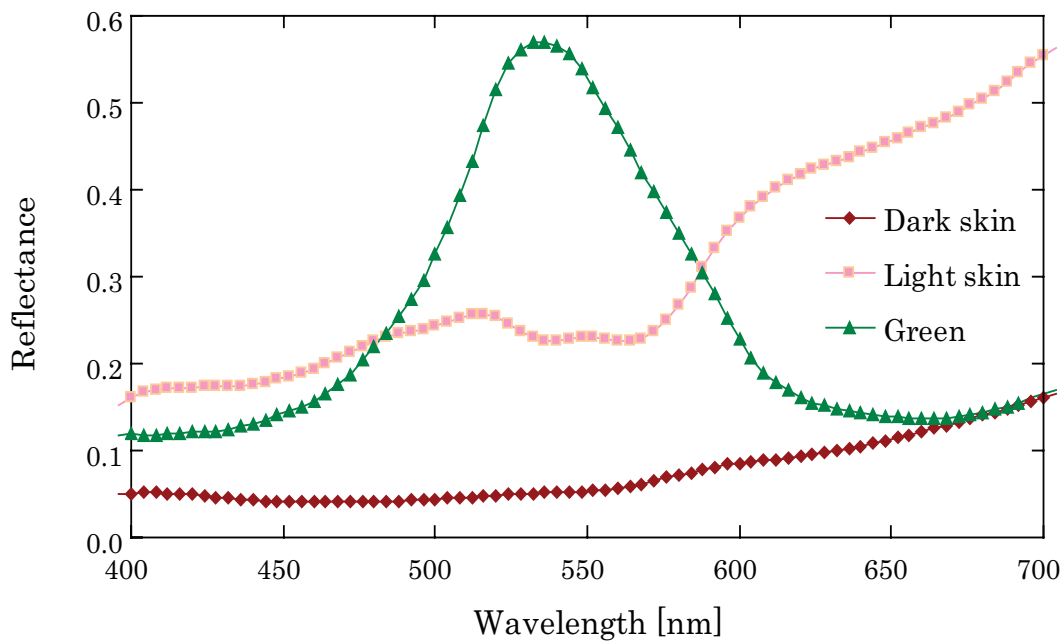


Figure 2.12: Reflectance data used in the fourth set of experiments; three reflectances are “Dark skin,” “Light skin,” and “Green” of the Macbeth ColorChecker. “Dark skin” varies linearly around wavelengths of a camera sensitivity compared to “Light skin” and “Green.”

down when the  $\sigma$  of Gaussian function is larger than 5 nm, while in the case of “Dark skin,” the estimation performs well until the  $\sigma$  becomes 20 nm.

If a reflectance varies linearly around wavelengths of a camera sensitivity, the integration in Eq. (2.3) becomes a multiplication by a constant number. Thus, the modeling error by the narrow-band assumption can be ignored. Otherwise, the modeling error affects the estimation; as Figure 2.12 shows, the reflectance “Dark skin” varies linearly around wavelengths of a camera sensitivity compared to “Green” and “Light skin.” When  $\sigma$  is set to 5 nm, half of the test data set provided good results within the error of 5.5 mired.

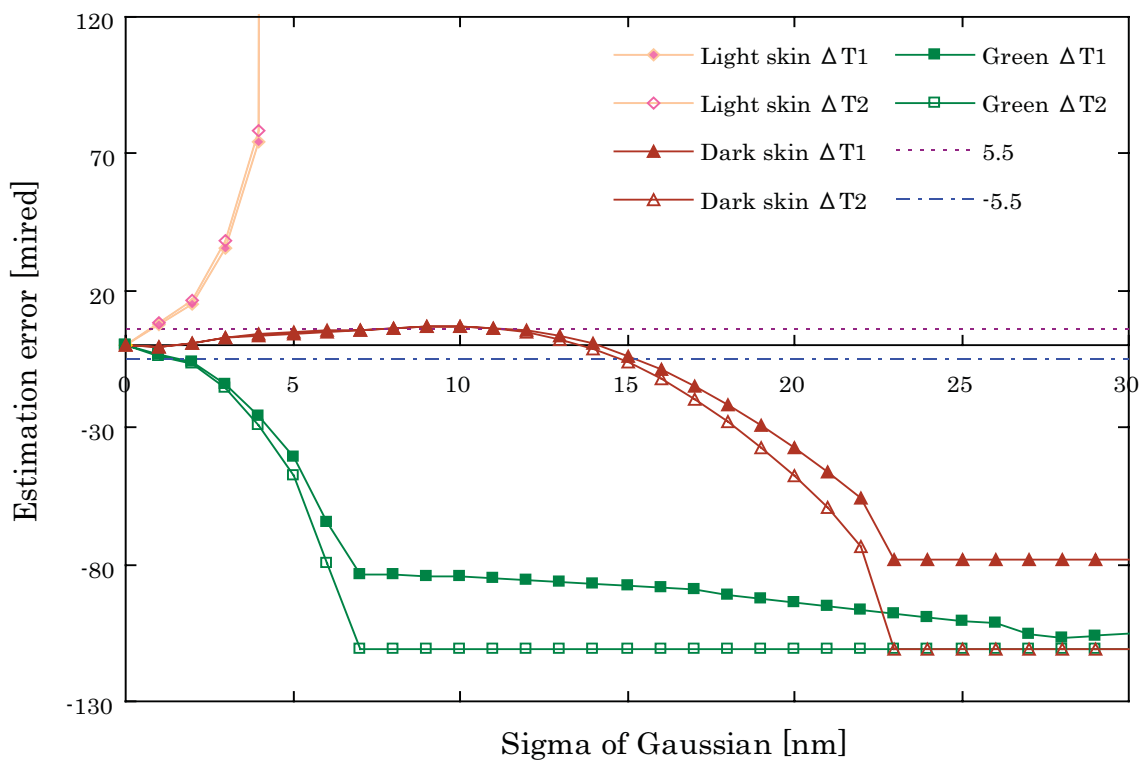


Figure 2.13: The plot of estimation error against the violation of the narrow-band sensitivity assumption. The more the bandwidth of a camera sensitivity (the standard deviation  $\sigma$  of a Gaussian function) grows, the larger the estimation error becomes. Three reflectances “dark skin,” “light skin,” and “green” were tested. The speed of the error growth depends on reflectance.

## 2.7 Discussion

Assuming illumination to be the blackbody radiation made the estimation sensitive to the modeling error. There are two other ways to express illumination by a one-dimensional parameter. One is to use Wien's approximation for blackbody radiation and the other is to use Finlayson et al.'s straight line approximation. The blackbody illumination model can be compared to those models. Wien's approximation to the Planck formula can be expressed as:

$$M(\lambda, T) \simeq c_1 \lambda^{-5} \exp(c_2/\lambda T)^{-1}. \quad (2.22)$$

From the last equation, we can derive the following relation [FH01, MO00]:

$$e_r = m e_g^A \quad (2.23)$$

where  $e = [e_r, e_g]^t$  is an illumination chromaticity,  $A = (\frac{1}{\lambda_R} - \frac{1}{\lambda_B}) / (\frac{1}{\lambda_G} - \frac{1}{\lambda_B})$  and  $m = \frac{\lambda_G^{5A}}{\lambda_R^A \lambda_B^{5A-5}}$  are constant numbers characterizing a camera. If we substitute the equation into Eqs. (2.12) and (2.13), we obtain two redundant equations and cannot determine the solutions for each color temperature. The Planck formula and Wien's approximation are very similar when the color temperature is low. Therefore, estimation of our method would be unstable if the two color temperatures of input illumination are both low.

Finlayson et al. assumed that natural daylight illumination falls on a line [FFB95] in an inverse-chromaticity space. Namely, they assumed the following relation:

$$1/e_g = m(1/e_r) + c. \quad (2.24)$$

Note that the last equation does not appear in the reference[FFB95] but it expresses its idea. The paper[FFB95] assumes that a set of all diagonal matrices mapping chromaticities under arbitrary illumination  $(e_r, e_g)$  to canonical illumination  $(e_r^{\text{canonical}}, e_g^{\text{canonical}})$  appears linear in the 1st-2nd diagonal matrix component space. In other words, it assumes  $f(x) = m'x + c'$ , where  $x$  and  $f(x)$  correspond to the first and the second diagonal matrix component  $e_r^{\text{canonical}}/e_r$  and  $e_g^{\text{canonical}}/e_g$ , respectively. We can derive Eq. (2.24), since both  $e_r^{\text{canonical}}$  and  $e_g^{\text{canonical}}$  could be any constant numbers, they can be replaced by (1, 1).

If we substitute the last equation into Eqs. (2.12) and (2.13), we can solve all the unknown parameters explicitly. (This paper was inspired by this discovery.) The gradient  $m$  and the intercept  $c$  in Eq. (2.24) are constant numbers calculated by the least-square fitting to the data of CIE standards and Judd's daylight phases. The

difference between those illumination data points and the straight line is shown in Table 2.5. Considering the results shown in Table 2.3, the previous method, Finlayson et al.'s straight line model, is the most successful, and we think that this is the only model for solving color constancy with illumination constraint. However, as shown in Tables 2.3 and 2.5, even the straight line model cannot help suffering from the effect of the modeling error.

Table 2.5: Difference between real illumination colors and colors calculated from the straight line illumination model.  $\Delta e_r$  and  $\Delta e_g$  are the error percentage of the illuminant's color to the straight line color model. Note that the difference is defined in the color space of the sensitivity used in Table 2.4.

Illuminants	$\Delta e_r$ [%]	$\Delta e_g$ [%]
CIE A	6.9829	-7.2289
CIE B	-1.9758	4.0070
CIE C	-1.1578	2.7347
Judd D48	-0.6929	1.3720
Judd D55	-0.4382	0.9421
Judd D65	-0.0239	0.0553
Judd D75	0.3781	-0.9191
Judd D100	1.0385	-2.6985

Thus, the comparison of one-dimensional models of the illumination shows that illumination color constraint can work itself as long as there is no modeling error. However, the modeling error cannot be ignored and must be considered in order to perform stable and accurate color constancy. We conclude that both illumination constraint and other rich information such as assumptions on reflectances should be taken into account for a robust estimation.

## 2.8 Summary

We proposed a new method to solve color constancy problem by exploiting blackbody radiation. Based on the approach, we examined and obtained the results in the following four points:

1. Our method performed considerably well in the experiments with simulation data.
2. To achieve the accuracy within the error of Just Noticeable Difference, the modeling error between the blackbody radiation and the illuminants should be lower than 0.1%.
3. Though the method uses initial values, the results do not depend on how to choose them.
4. Most illuminants have larger than 0.1% difference from the blackbody radiation.

The discussion about the robustness of our method and the possibility of solving color constancy using a one-dimensional model of the illumination shows that much information such as assumptions about reflectances should be taken into account with the constraint on illumination to achieve stable and accurate color constancy.



## Chapter 3

# Robust Framework to Estimate Surface Chromaticity from Illumination Changes

The appearance of surface colors of an object is both deceptive and inconsistent. Color sensors do not see the true color of the surface because its appearance is significantly altered by varying illumination colors. To derive the actual and consistent surface colors, we have to estimate and then remove the illumination colors. This chapter proposes a method that stabilizes illumination-color estimation by using the idea of a finite illumination color space. It is a finite line where every illumination color exists. By restricting the estimated illumination colors to be on this line, the method succeeds in making the estimation more robust and accurate. We have shown the difficulty of estimating illumination colors in the previous chapter. Thus, the method presented here would be a strong alternative for solving the problem. Experiments show the effectiveness of our method.

We also show a method to find two differently illuminated regions in a single image. This would make the proposed method applicable to a single image. The technique we introduce utilizes shadowed and non-shadowed regions by using physics-based knowledge of outdoor illuminations. Experimental results with real outdoor images show the effectiveness of our method.

### 3.1 Introduction

Reflected light from an object is the product of surface spectral reflectance and illumination spectral power distribution. Consequently, illumination color significantly determines the object's color appearance. When the illumination color changes, the object color appearance changes accordingly. This leads to many problems in algorithms of computer vision. An example is shown in Figure 1.2; it shows that the illumination change in creating a realistic model causes the color appearance of an object to be inconsistent. Recovering the surface's actual color requires a method that discounts the inconsistencies caused by variations in illumination.

This chapter aims to estimate and to remove the illumination color of outdoor scenes, and to accurately estimate the surface color of the object. In real outdoor images, the presence of input errors is inevitable. Such errors include measurement errors caused by sensor noises and systematic errors caused by variation of the medium (air), assumption of simple reflection models, interreflection, and imperfect paintings of the object. Outdoor illumination colors may also include a small error from the assuming color model. The previous methods [D'Z92, FFB95] would produce large errors when those errors are included in the input images; details of the related works for estimating surface colors are summarized in 2.1.1. This paper aims to minimize the effect of those errors by calculating the most likely values of error-less input. We have also analyzed those errors and identified the situations in which we could robustly perform the estimation. Experiments on real images show the effectiveness of the method.

Another problem to deal with in outdoor images is the presence of shadows. An image often includes both shadowed and non-shadowed regions. Images with shadows cannot be correctly handled by the previous methods [BF97, FHH01, TW02] because those methods require uniformly colored illumination in images. Previously researchers (for example, [FF94]) have found that shadowed regions are illuminated by sky light, while non-shadowed regions are illuminated by a combination of sky light and sunlight. This paper proposes a method that can handle them by utilizing this difference of illuminations in shadowed and non-shadowed regions. It estimates illumination colors for both sunlight and sky light and then removes them. Two colors from shadowed and non-shadowed regions are extracted automatically by using the expectation-maximization (EM) algorithm. Illumination colors are assumed to be uniform inside each region.

## 3.2 Assumptions and Definitions

This paper assumes the following: (1) Linearity assumption: The output of camera response is linear to the flux of incoming light intensity. (2) Narrowband assumption: The camera sensitivity function is narrowband and known. (3) Straight-line assumption: The illumination color can be approximated by a straight line in an inverse-chromaticity space. (4) Two-region assumption: Target scenes can be segmented into two differently illuminated regions, and each region is lit by a uniformly colored light. (5) Common-region assumption: A target object exists in the scene under the two-region assumption, and the target surface color exists in both regions in the scene. (6) Non-interreflection assumption: The diffuse interreflection is negligible.

The linearity and narrowband assumptions are common in many color constancy algorithms. The two-region assumption is valid when the target scene includes a region lit by strong direct sunlight and a hard-shadowed region.

### Image Formation

According to the linearity assumption, the image intensity of diffuse objects taken by a digital color camera can be described as:

$$I_c = \int_{\Omega} S(\lambda)E(\lambda)q_c(\lambda)d\lambda \quad (3.1)$$

where  $I_c$  is the sensor response (RGB pixel values),  $S(\lambda)$  is the surface spectral reflectance,  $E(\lambda)$  is the illumination spectral power distribution,  $q_c$  is the three-element vector of sensor sensitivity, and index  $c$  represents the type of sensors (R, G, and B). The integration is done over the visible spectrum ( $\Omega$ ). In this model we ignore camera noise and gain. By the narrowband assumption that follows the Dirac delta function, Eq. (3.1) can be simply rewritten as:

$$I_c = S_c E_c \quad (3.2)$$

where  $S_c = S(\lambda_c)$  and  $E_c = E(\lambda_c)$ . Camera sensitivity can be obtained using a monochromator and a spectrometer [VFTB97]. If camera sensitivity cannot be approximated by the Dirac delta function (narrowband sensor), we could apply camera sharpening algorithms proposed by [FDF94, BCF01].

### Chromaticity

Following [FFB95], this paper defines chromaticity (or specifically *image* chromaticity) as:

$$i_r = \frac{I_R}{I_B}, \quad i_g = \frac{I_G}{I_B} \quad (3.3)$$

The reason for using Eq. (3.3) is because the relation of Eq. (3.2) still holds in this color space:

$$i_c = s_c e_c \quad c = \{r, g\} \quad (3.4)$$

where  $s_c$  and  $e_c$  correspond to the chromaticities of  $S_c$  and  $E_c$ . We call  $s_c$  surface chromaticity and  $e_c$  illumination chromaticity. In Eq. (3.3), either the red or green channel may be alternatively used as the denominator if the intensity of the blue channel is considerably low.

### 3.3 Surface Color Estimation

The problem of color constancy can be considered, from Eq. (3.4), as the problem of estimating the values of  $e_c$  and  $s_c$  given the value of  $i_c$ , where the index is  $c = \{r, g\}$ . However, estimating four unknown values ( $e_r, e_g, s_r, s_g$ ) from two equations is mathematically ill-posed. Therefore, we add constraints to increase the number of equations and make them solvable. First, we increase the number of image chromaticities:  $i_c^1$  and  $i_c^2$  are taken from a single surface chromaticity ( $s_c$ ) but with different illuminations ( $e_c^1$  and  $e_c^2$ ):

$$i_r^1 = s_r e_r^1, \quad i_r^2 = s_r e_r^2 \quad (3.5)$$

$$i_g^1 = s_g e_g^1, \quad i_g^2 = s_g e_g^2 \quad (3.6)$$

Four equations with six unknowns ( $s_r, s_g, e_r^1, e_g^1, e_r^2, e_g^2$ ) can be obtained.

Second, we model the relation between  $e_r$  and  $e_g$  by utilizing the knowledge of natural (outdoor) illumination distributions. Regarding Finlayson et al.'s method [FFB95], which assumes that the correlation can be approximated as a straight line in the inverse-chromaticity space, we can write the relation of  $(1/e_r, 1/e_g)$  as:

$$\frac{1}{e_g} = m \frac{1}{e_r} + c \quad (3.7)$$

We call this line an *Illumination line* for convenience. Having introduced Eq. (3.7), we have six equations with six unknowns and thus the set of the six equations becomes

solvable. Note that the last equation does not appear in the reference [FFB95], but it can be simply derived from it. The gradient  $m$  and the intercept  $c$  are constant numbers calculated by the least-square fitting to the data of CIE (International Commission on Illumination) standard illuminants (A, B, C) and Judd et al.'s daylight phases (D48, D55, D65, D75, D100).

Fig. 3.1 (a) shows that those illuminants roughly form a line in the inverse-chromaticity space. The sensitivity used to calculate the color space is shown in Fig. 3.1 (b). It is the sensitivity of SONY-DXC9000 which we used for our experiments. We can predict that daylight illuminants would also form a line in other inverse-chromaticity spaces as well, such as in inverse 1931 CIE chromaticity diagram [FFB95]. As summarized in 2.1.2, Planckian locus could approximate the distribution of daylight colors. Since the locus can be approximated by a line in a certain range, we can predict that daylight colors would be approximated by a line in any inverse-chromaticity spaces.

Solutions of the equations can be derived as follows. By substituting Eq. (3.7) into Eqs. (3.5) and (3.6), the following two linear independent equations can be obtained:

$$s_g = \left(m \frac{i_g^1}{i_r^1}\right) s_r + i_g^1 c \quad (3.8)$$

$$s_g = \left(m \frac{i_g^2}{i_r^2}\right) s_r + i_g^2 c \quad (3.9)$$

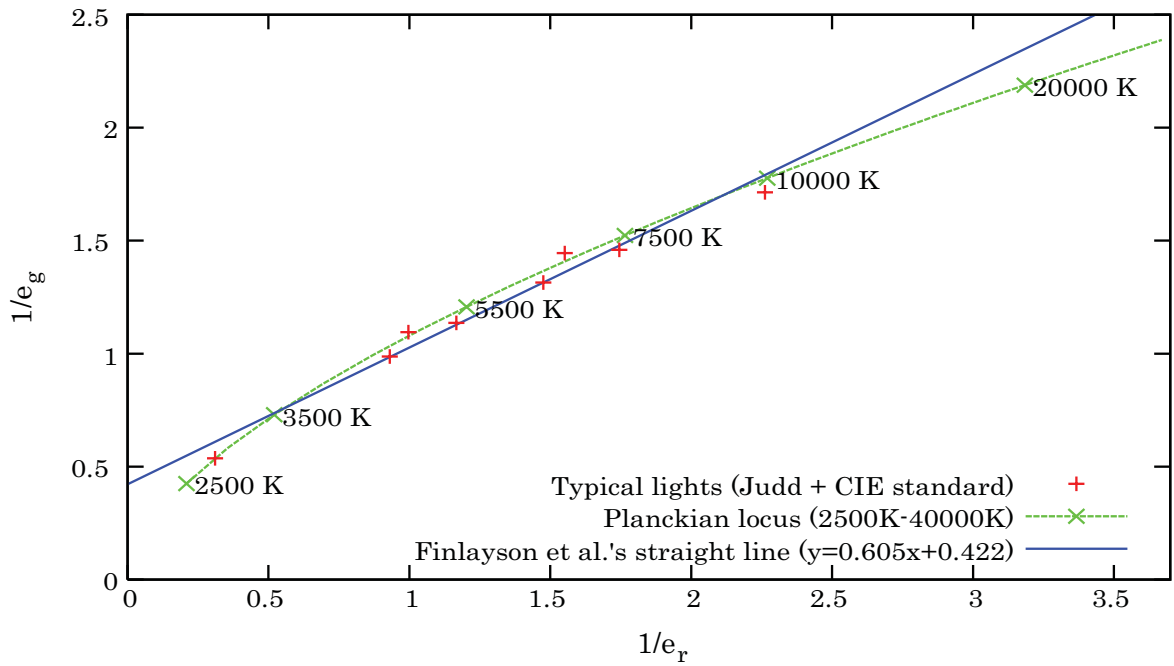
Each equation means an expanded *Illumination line* whose  $r$  axis is scaled by the factor of  $i_r$  and whose  $g$  axis is scaled by the factor of  $i_g$ . The surface color  $(s_r, s_g)$  becomes the intersection of two generated lines.

$$s_r = \frac{i_r^1 i_r^2 (i_g^2 - i_g^1)}{i_r^2 i_g^1 - i_r^1 i_g^2} \frac{c}{m} \quad (3.10)$$

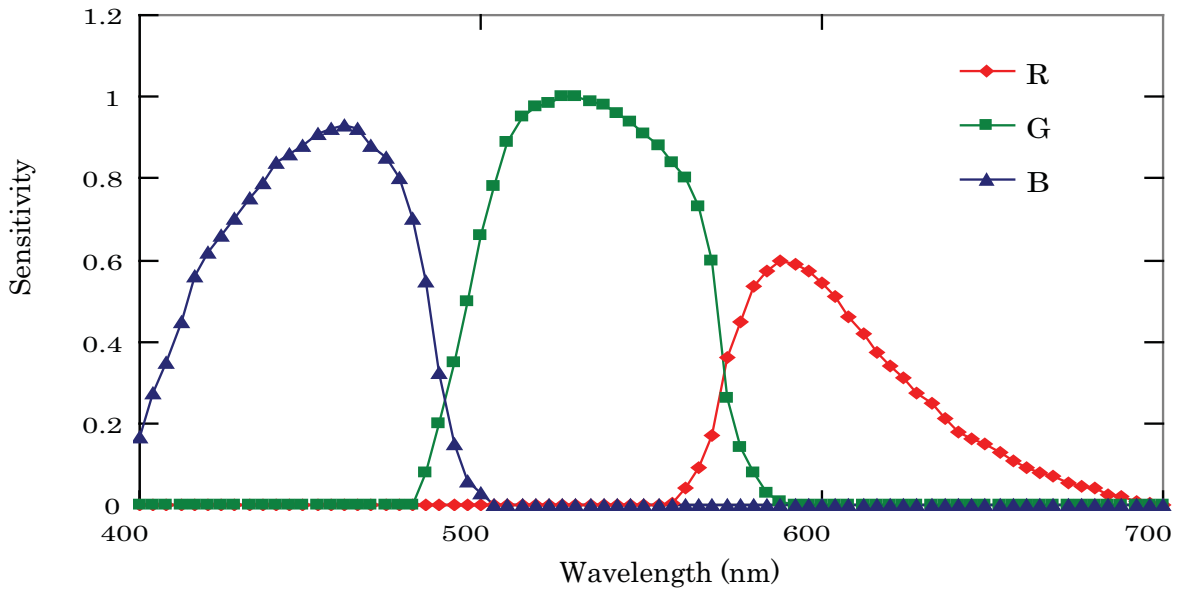
$$s_g = \frac{i_g^1 i_g^2 (i_r^2 - i_r^1)}{i_r^2 i_g^1 - i_r^1 i_g^2} c \quad (3.11)$$

### 3.4 The Effect of Input Errors

While surface color estimation using the straight-line assumption can theoretically solve the problem, in practice we observe that it is significantly sensitive to input errors. Assuming that input chromaticities are affected by errors, two generated lines in Eqs. (3.8) and (3.9) will be incorrect. As a result, the intersection, the surface color



(a) Typical daylight in an inverse-chromaticity space.



(b) Typical camera-sensor sensitivity.

Figure 3.1: (a) Typical daylight data roughly form a line in an inverse-chromaticity space. Crosses: Daylight data (CIE standards and Judd et al.'s daylight phases). Line: Finlayson et al.'s illumination line obtained by the least-square fitting. The Planckian locus is also shown for comparison. (b) The sensitivity of SONY-DXC9000. Each chromaticity in (a) was calculated in the color space of it.

estimated, will deviate significantly from the correct one, especially when the gradients of two lines are similar.

This section examines possible input errors and their effects on surface color estimation. We analytically derive the average amount of input errors and discuss the condition in which the estimation could endure such input errors.

### 3.4.1 Input errors

#### Error model

Sensor output includes noises and systematic errors. Sensor noises include: read, quantization, dark current, and shot noises. They can be reduced by averaging input values from increasing the number of pixels used, or by using the High Dynamic Range imaging technique.

Images of outdoor scenes also include systematic errors for surface color estimation. Those systematic errors come from the discrepancy between the reality and the assumption: (1) the straight-line assumption for outdoor illumination colors, (2) the narrowband assumption that is only an approximation for general cameras, (3) the effect of the participating medium (air), (4) simple reflection models (objects may not be entirely diffuse), (5) interreflection, and (6) imperfect paintings or dust on surfaces. These systematic errors cannot be reduced by using such averaging techniques.

Among those errors, we focused on errors caused by straight-line and narrowband assumptions. This is because those are the most dominant factors among them. Considering the errors, an actual chromaticity  $i_c$  deviates from an ideal chromaticity  $\hat{i}_c$ , with an error  $\Delta i_c$ .

$$i_c = \hat{i}_c + \Delta i_c \quad c = \{r, g\}. \quad (3.12)$$

Note that the effect of the straight-line and narrowband assumptions cannot be separately treated. The straight line already includes small error from the ideal illumination line defined in a narrowband camera's color space, because the illumination line is computed in a color space of a camera that has rather wide sensitivity.

The ideal chromaticity  $\hat{i}_c$  can be written as

$$\hat{i}_c = \hat{s}_c \hat{e}_c \quad (3.13)$$

where  $\hat{e}_c$  is the ideal illumination chromaticity that lies on the illumination line, and  $\hat{s}_c$

is an ideal surface chromaticity, a surface color under pure white illumination;

$$\hat{s}_c = \int_{\omega} S(\lambda)q_c(\lambda)d\lambda. \quad (3.14)$$

where the total power of the sensitivity  $q_c(\lambda)$  is supposed as follows;  $\int_{\omega} q_c(\lambda)d\lambda = 1.0$ . An input error can be defined as the difference between the actual  $i_c$  and the ideal  $\hat{s}_c\hat{e}_c$  image chromaticities.

### Error simulation

Using the error models defined, we calculated actual and ideal image chromaticities of surfaces with various natural illuminations. Examples plotted in inverse-chromaticity space according to six surface colors are shown in Figures 3.2, 3.3 and 3.4. The crosses are the set of actual chromaticities  $i_c$  calculated from a surface color with different illuminations whereas the lines are the set of ideal chromaticities  $\hat{i}_c$ . The values  $i_c$  and  $\hat{i}_c$  were calculated using Eq. (3.1) and  $\hat{s}_c\hat{e}_c$ , respectively.

Data used for surface reflectance, illumination spectra, and camera sensitivity are listed in Table 3.1. Here, we have conducted simulations of image measurements by SONY DXC-9000, of which filtering characteristics are shown in Figure 3.1 (b), using 18 different kinds of reflectance patches in the Macbeth color checker, under 12 blackbody and 7 CIE standard illuminants.

Most actual image chromaticities include small errors from ideal values, as shown in Figures 3.2, 3.3 and 3.4, because 12 blackbody and 7 CIE standard illuminants in Table 3.1 do not strictly follow the straight line, and the camera sensitivity shown in Figure 3.1 (b) is not sufficiently narrow. Furthermore, it is difficult to predict the error value  $\Delta i_c$  from the input value  $i_c$ , as shown in Figures 3.2, 3.3 and 3.4.

Table 3.1: Data used to simulate actual and ideal image chromaticities.

Data	Details	Number of samples
Reflectance	Reflectance of Color Checker (GretagMacbeth)	18
Illuminants	Blackbody illuminants (3500K-12000K)	12
	CIE standard illuminants (B,C,D48-D100)	7
Camera sensitivity	SONY DXC-9000 (Shown in Figure 3.1 (b))	1

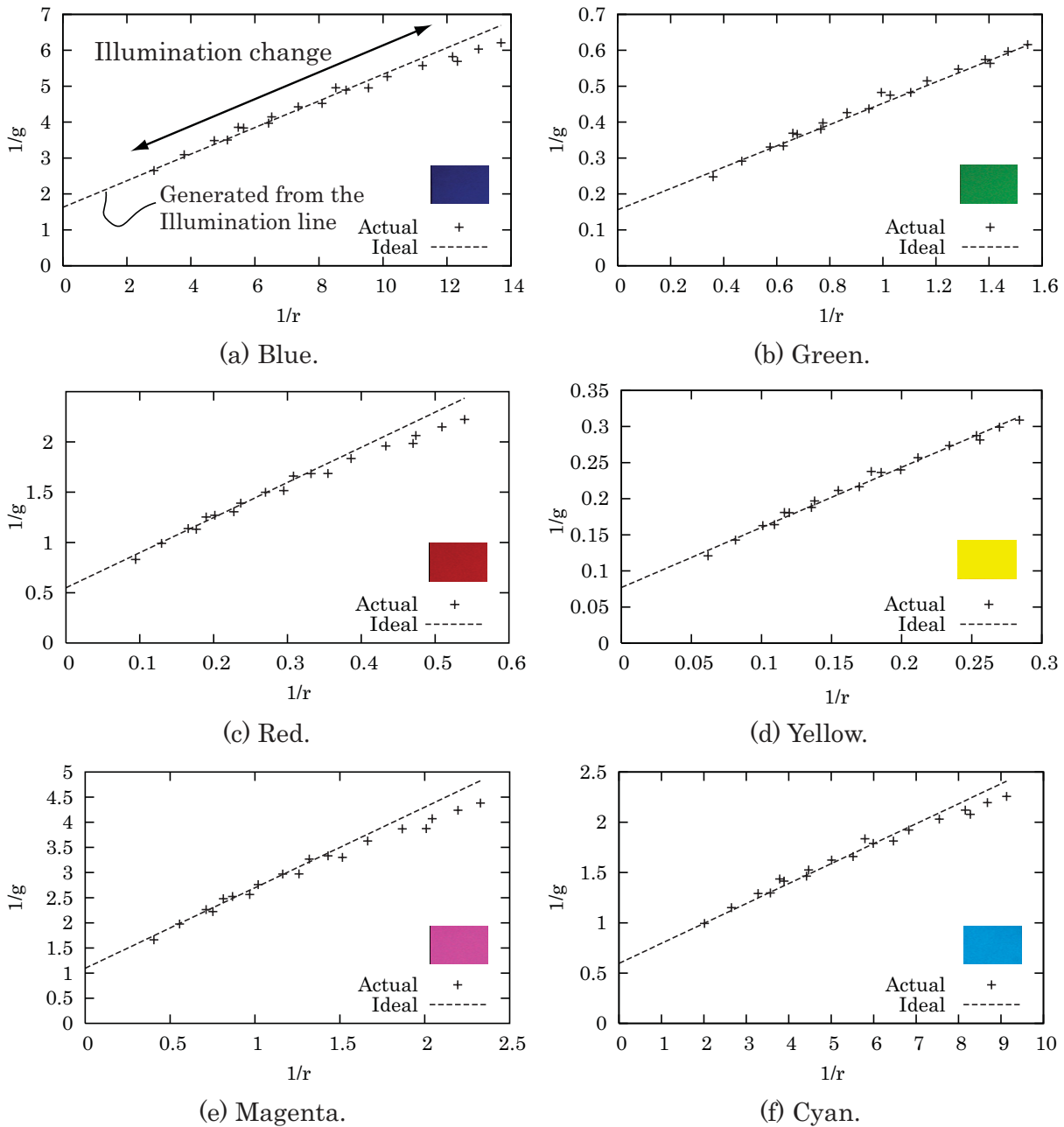


Figure 3.2: Simulated image chromaticities under illumination change: Actual (crosses) and ideal (lines) chromaticities in inverse-chromaticity space according to (a) Blue, (b) Green, (c) Red, (d) Yellow, (e) Magenta, and (f) Cyan reflectances with various illuminations; the details of data used for this simulation are shown in Table 3.1. Most actual image chromaticities  $(i_r, i_g)$  include a small error  $(\Delta i_r, \Delta i_g)$  from ideal values  $(\hat{i}_r, \hat{i}_g)$  due to the straight-line and the narrowband assumptions. While it is difficult to predict an error value from an input value.

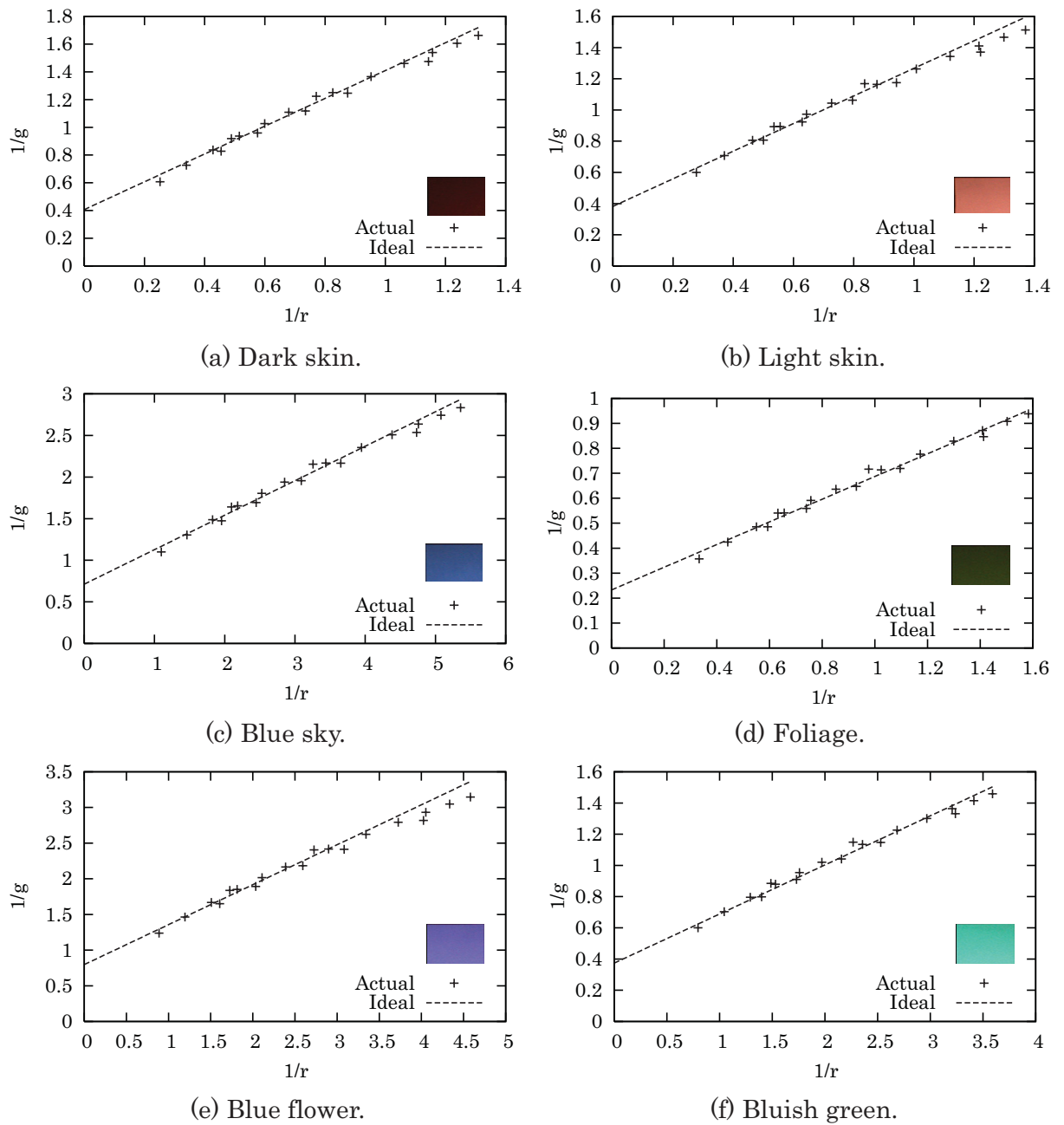
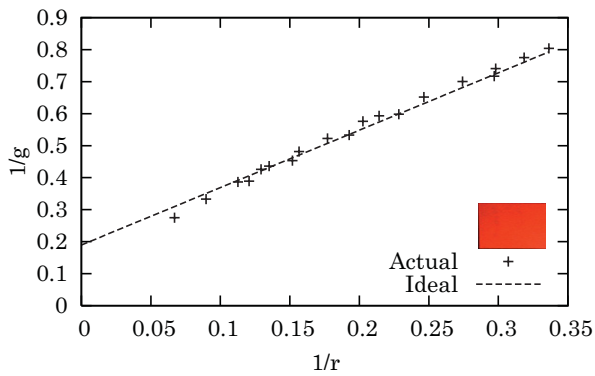
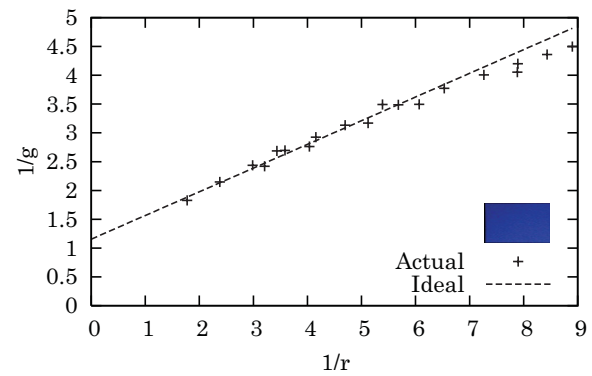


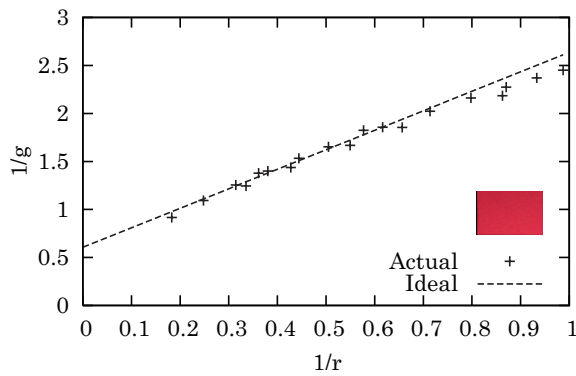
Figure 3.3: Other examples of simulated image chromaticities under illumination change: Actual (crosses) and ideal (lines) chromaticities according to (a) Dark skin, (b) Light skin, (c) Blue sky, (d) Foliage, (e) Blue flower and (f) Bluish green.



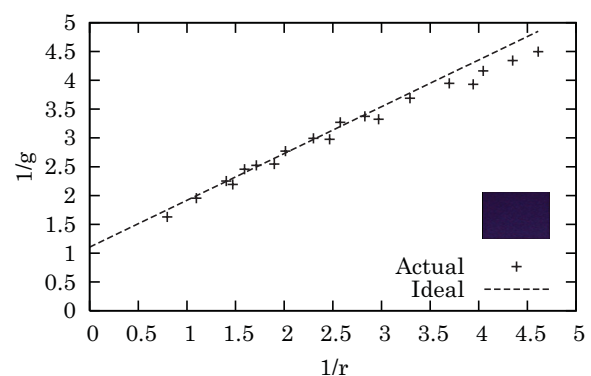
(a) Orange.



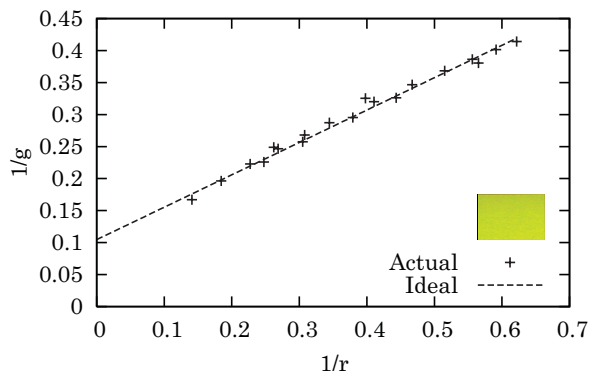
(b) Purplish blue.



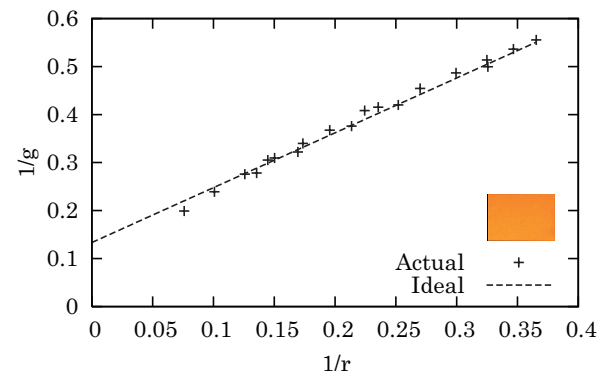
(c) Moderate red.



(d) Purple.



(e) Yellow green.



(f) Orange yellow.

Figure 3.4: Other examples of simulated image chromaticities under illumination change: Actual (crosses) and ideal (lines) chromaticities according to (a) Orange, (b) Purplish blue, (c) Moderate red, (d) Purple, (e) Yellow green, and (f) Orange yellow.

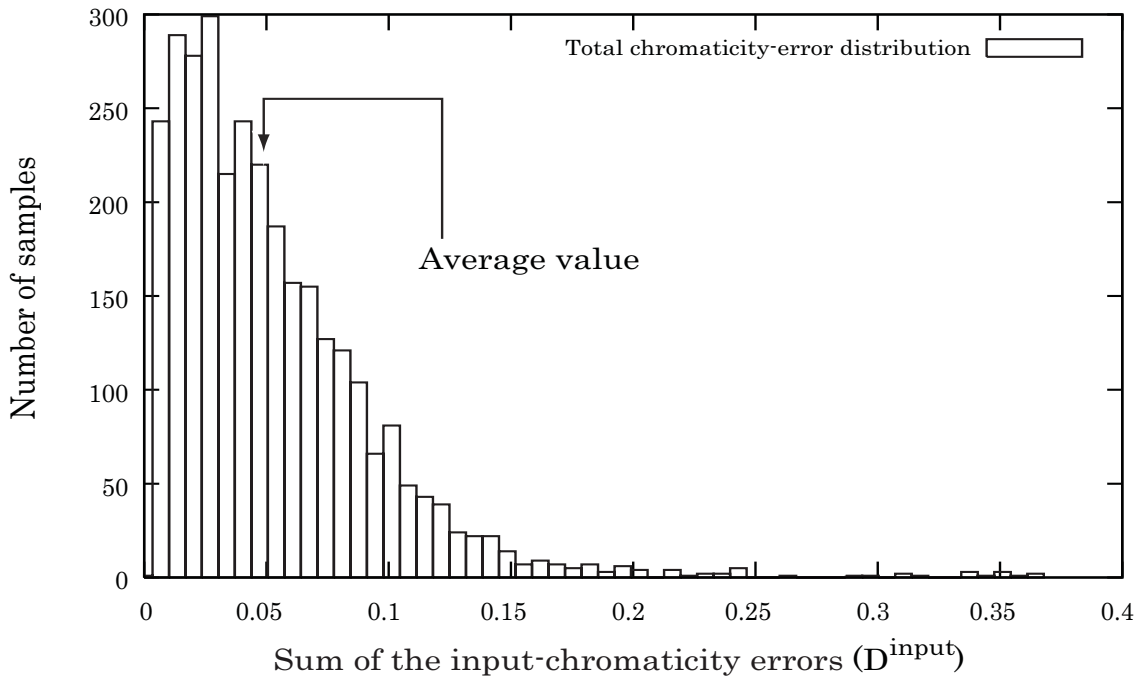


Figure 3.5: The distribution of the sum of the input error values,  $D^{\text{input}}$ . The average value was 0.0496, and the mode was 0.027. We also tested the distributions with Nikon D1 and SONY ICX204AK, and the averages were 0.0491 and 0.0664, respectively. The numbers predict that SONY DXC-9000 and Nikon D1 will produce similar algorithm performance.

### Total error approximation

The surface color estimation uses four input values  $i_r^1, i_g^1, i_r^2,$  and  $i_g^2$  that may include errors. To deal with the four values at once, we approximate that the sum of the four input error values  $D^{\text{input}}$  affects the estimation error values;

$$D^{\text{input}} \equiv \left( \left| \frac{\Delta i_r^1}{\hat{i}_r^1} \right| + \left| \frac{\Delta i_g^1}{\hat{i}_g^1} \right| \right) + n \left( \left| \frac{\Delta i_r^2}{\hat{i}_r^2} \right| + \left| \frac{\Delta i_g^2}{\hat{i}_g^2} \right| \right) \quad (3.15)$$

where  $n$  is 1.0 when the sign of  $\Delta i_r^1$  is equal to that of  $\Delta i_r^2$  and is  $-1.0$  otherwise. The  $n$  is introduced because either  $\Delta i_r^1$  and  $\Delta i_r^2$  or  $\Delta i_g^1$  and  $\Delta i_g^2$  cancel the effect of each other when their signs are equal.

The distribution of  $D^{\text{input}}$  that are calculated from the data in Figures 3.2, 3.3 and 3.4 is illustrated in Figure 3.5, where the horizontal and vertical axes represent  $D^{\text{input}}$  and the number of samples, respectively. The average value of  $D^{\text{input}}$  was about 0.05.

Table 3.2: The values of estimation error rate when the inputs include errors.

Input	Error rate in $r$ channel $\Delta s_r/s_r$	Error rate in $g$ channel $\Delta s_g/s_g$
$i_r^1 = \hat{i}_r^1 + \Delta i_r^1$	$\frac{\Delta i_r^1}{\hat{i}_r^1} \frac{1}{1 - \left(1 + \frac{\Delta i_r^1}{\hat{i}_r^1}\right) \frac{e_r^1/e_g^1}{e_r^2/e_g^2}}$	$\frac{\Delta i_r^1}{\hat{i}_r^1} \frac{1}{1 - \left(1 + \frac{\Delta i_r^1}{\hat{i}_r^1}\right) \frac{e_r^1/e_g^1}{e_r^2/e_g^2}} \frac{\hat{i}_r^1 i_g^2 - i_r^1 \hat{i}_g^1}{\hat{i}_r^1 i_r^2 - \hat{i}_r^1 \hat{i}_g^1}$
$i_g^1 = \hat{i}_g^1 + \Delta i_g^1$	$-\frac{\Delta i_g^1}{\hat{i}_g^1} \frac{1}{\left(1 + \frac{\Delta i_g^1}{\hat{i}_g^1}\right) - \frac{e_r^1/e_g^1}{e_r^2/e_g^2}} \frac{i_g^2 i_r^2 - i_r^1 \hat{i}_g^1}{\hat{i}_r^1 i_r^2 - \hat{i}_r^1 \hat{i}_g^1}$	$-\frac{\Delta i_g^1}{\hat{i}_g^1} \frac{1}{\left(1 + \frac{\Delta i_g^1}{\hat{i}_g^1}\right) - \frac{e_r^1/e_g^1}{e_r^2/e_g^2}} \frac{\hat{i}_r^1 i_g^2}{\hat{i}_r^1 i_r^2}$

### 3.4.2 The effect of input errors on surface color estimation

When the input chromaticities include errors, two generated lines, Eqs. (3.8) and (3.9), will be incorrect. As a result, the intersection, the surface color estimated, will deviate significantly from the correct one, especially when the gradients of two lines are similar.

This can be shown in a mathematical way. The surface chromaticity  $s_r$  is given as in Eq. (3.10). For instance, assume that an image chromaticity includes an error  $\Delta i_r^1$  from an ideal value  $\hat{i}_r^1$ , then the estimated surface chromaticity will deviate from the correct value  $s_r$  to  $s_r + \Delta s_{rr}$ .

$$s_r + \Delta s_{rr} = \frac{(\hat{i}_r^1 + \Delta i_r^1) i_r^2 (i_g^2 - i_r^1) c}{i_r^2 i_g^1 - (\hat{i}_r^1 + \Delta i_r^1) i_g^2} m. \quad (3.16)$$

Then, the error rate  $\Delta s_{rr}/s_r$  can be calculated as follows;

$$\frac{\Delta s_{rr}}{s_r} = \frac{\Delta i_r^1}{\hat{i}_r^1} \frac{1}{1 - \left(1 + \frac{\Delta i_r^1}{\hat{i}_r^1}\right) \frac{e_r^1/e_g^1}{e_r^2/e_g^2}} \quad (3.17)$$

We summarize those error rate in Table 3.2. Each row in Table 3.2 provides the effect from each channel. Deriving from Table 3.2, the estimation error rate of  $\Delta s_{rr}/s_r$  becomes;

$$\frac{\Delta s_{rr}}{s_r} \approx \frac{\Delta i_r^1}{\hat{i}_r^1} \frac{1}{\left(1 - \frac{e_r^1/e_g^1}{e_r^2/e_g^2}\right)} = \frac{\Delta i_r^1}{\hat{i}_r^1} W \quad (3.18)$$

where we assumed  $1 + \Delta i_r^1/\hat{i}_r^1 \approx 1$ .

$W$  in Eq. (3.18) increases as the color temperature difference between two illumination decreases. The actual numerical values of  $W$  are plotted in Figure 3.6. The horizontal and vertical axes mean the color temperature difference<sup>4</sup> and the value of  $W$ , respectively. As shown in Figure 3.6,  $W$  is always larger than 1.0, and thus, it magnifies the input error for the estimation. Note that we can approximate  $1 + \Delta i_c / \hat{i}_c \approx 1$ . Then, all the second terms of the equations in Table 3.2 can be approximated as  $W$ . Namely,  $W$  equally affects all input errors,  $\Delta i_c$ .

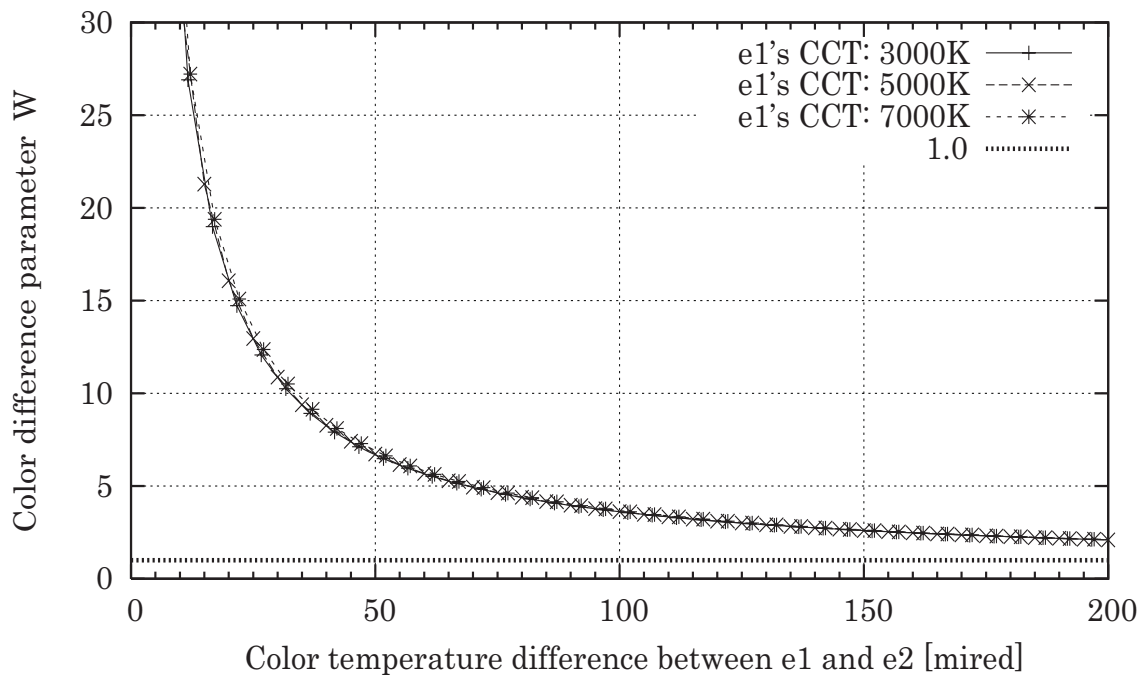


Figure 3.6: We simulated the actual value of  $W$ , which affects the surface chromaticity estimation.  $W$  is always larger than 1.0, and thus, it magnifies the input error for the estimation. The sensitivity shown in Figure 3.1 (b) was used to calculate the illumination chromaticity in this simulation.

### 3.4.3 Decreasing the effect of input errors

We have conducted experiments of surface color estimation using the straight-line method [FFB95], and plotted the estimation error against the multiplication of  $D^{\text{input}}$

<sup>4</sup> The unit of color temperature difference is  $10^6/K = \text{mired}$  (microreciprocal degrees). Two-hundred-mired difference corresponds to the difference between 3300K and 10000K, which covers the possible range of outdoor illumination colors.

and  $W$ ; i. e. , the sum of the input error values and the factor that magnify the input error. The result is shown in Figure 3.7.

As illustrated in Figure 3.7, the estimation error increases approximately linearly against  $D^{\text{input}}W$ ;

$$\text{(Estimation error value)} \propto D^{\text{input}}W \quad (3.19)$$

In Figure 3.7, the horizontal and vertical axes are  $D^{\text{input}}W$  and the color difference between the estimated  $\mathbf{e}_{\text{est}}^1$  and the true  $\mathbf{e}_{\text{true}}^1$  illumination colors in CIE LAB space, respectively. CIE LAB space is a color space in which the distance corresponds to the visual importance in human perception, and can be computed via simple formulas from the CIE 1931 XYZ space [WS00]. We used CIE LAB space to evaluate the estimation error in the system of human perception. Examples of CIE LAB colors are shown in Figure 3.8. From the figure, we decided that the error in surface/illumination estimation should be less than 10.0 in CIE LAB color space.

In order to suppress the estimation error value under 10.0 CIE LAB errors, Figure 3.7 indicates that the value of  $D^{\text{input}}W$  needs to be less than 0.20. With respect that the average value of  $D^{\text{input}}$  is about 0.05, as stated in 3.4.1, the preferable color temperature difference between two illumination colors should be more than 100 mired,  $W \leq 4$ , according to Figure 3.6.

As we mentioned in Section 3.4.1, it is difficult to predict an input error value  $\Delta i_c$  from an image chromaticity  $i_c$ . In order to minimize the estimation error under the presence of input errors, color temperature difference between two illuminations is preferred to be as large as possible (more than 100 mired). However, the color temperature difference during a day is not likely to be more than 100 mired. We have measured daylights in Tokyo on a sunny day, 31st January in 2007. The reddest was observed at sunset, when the measuring device was facing the sun direction; the correlated color temperature was 260 mired. The bluest was 150 mired at meridian passage and at sunset, when the device was against the sun; the maximum difference was 110 mired. The difference is mostly less than our recommended color difference, 100 mired. Hence, a method to detect and reduce the input errors is necessary.

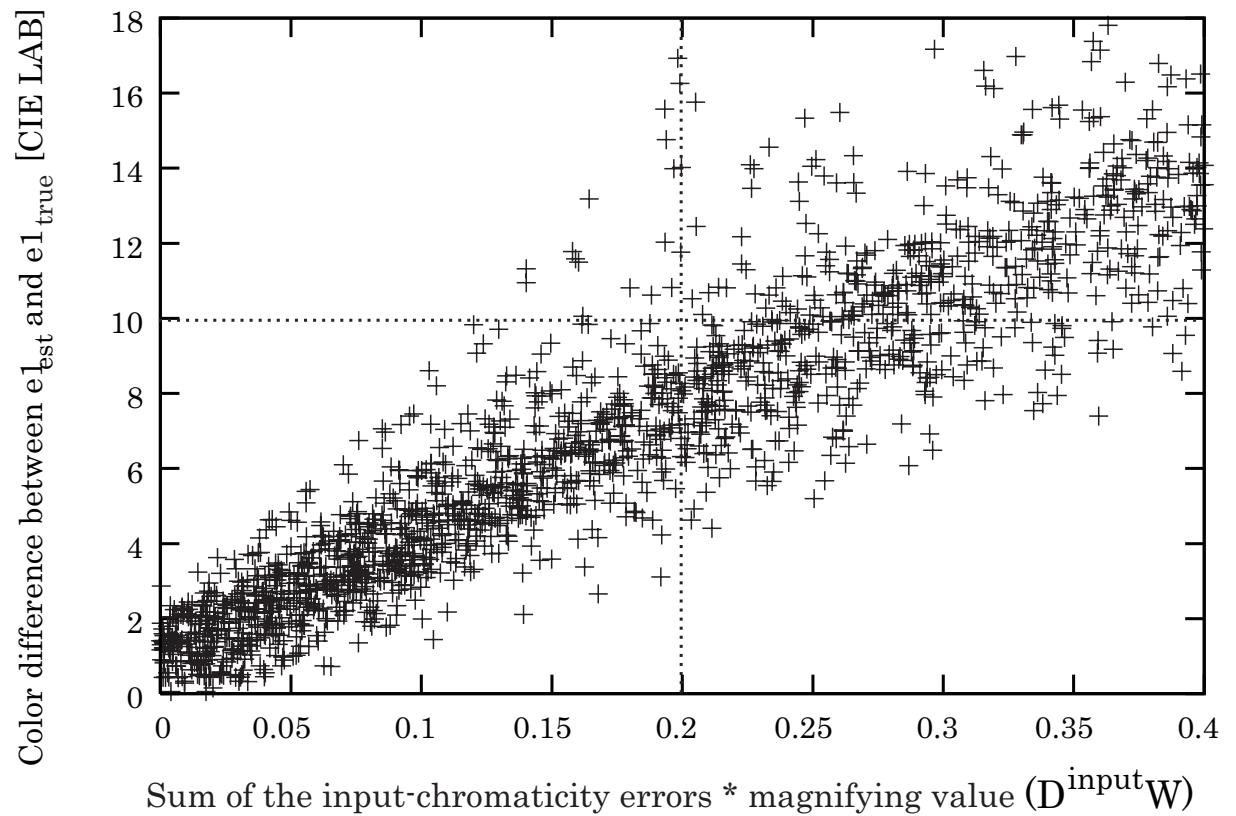


Figure 3.7: The estimation error values in CIE LAB color space against  $D^{\text{input}}W$ . The estimation error increases approximately linearly as  $D^{\text{input}}W$  increases. The value of  $D^{\text{input}}W$  needs to be less than 0.2 to suppress the estimation error value under 10 CIE LAB errors. Consequently, the preferable color temperature difference between two illumination colors will be more than 100 mired ( $W \leq 4$  in Figure 3.6), since the average value of  $D^{\text{input}}$  is about 0.05.

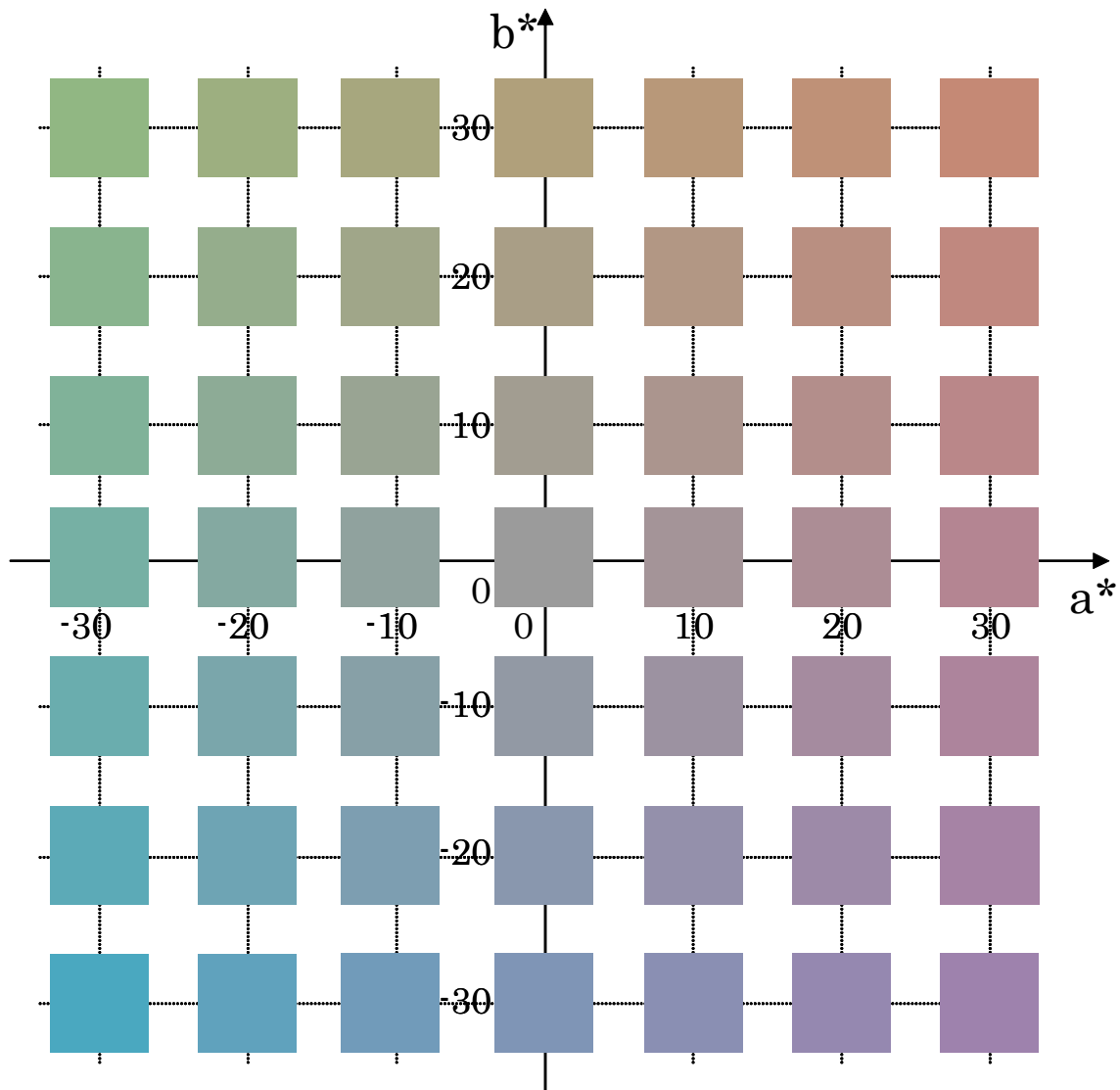


Figure 3.8: CIE LAB color examples. The value of  $L^*$  is uniform in the figure. From the figure, we decided that the error in surface/illumination estimation should be less than 10.0 in CIE LAB color space.

### 3.5 Proposed method I: Robust Framework

We propose a method for detecting the estimation error and reducing it by utilizing the finite range of the illumination color space. We can define the possible range of color temperature for outdoor illumination. Then, the plausible solutions of illumination colors are on the specific line segment along the Illumination line. This line segment provides a constraint to examine the soundness of the solution.

If the estimated illumination chromaticities are outside of the defined line segment, the estimated chromaticities contain errors. The estimation error is influenced by input errors; the method makes an attempt to correct the input error. Specifically, it chooses one of four input chromaticity values  $(i_r^1, i_g^1)$ ,  $(i_r^2, i_g^2)$  and adjusts the chromaticity value.

Each procedure of the whole algorithm is as follows:

1. Estimate illumination color from the Illumination line segment.
2. If the estimation includes no error,  $\Rightarrow$  terminate the process.
3. Otherwise,  $\Rightarrow$  select one of the image chromaticity values and adjust it.
4. Do the illumination estimation once again with the new adjusted chromaticities.

The details of each procedure are explained in the following subsections; Subsections 3.5.1, 3.5.2, 3.5.3 and 3.5.4 are about the procedures 1, 2, and 3, respectively.

#### 3.5.1 Finite range of outdoor illumination

Since the possible range of outdoor illumination colors is finite (assuming that the illumination follows blackbody radiator), the Illumination line is actually a line segment in the real world. This range of color temperatures varies from approximately 3500 K (286 mired) to 7500 K (133 mired) according to the data that we measured in Tokyo, Japan. We determined the gradient and the intercept of the line by using the least square fitting to the data of CIE A, B, C and Judd's daylight phases D48, D55, D65, D75 and D100. The range of the line was determined by the range of color temperatures, 3500 to 7500 in Kelvin.

As a consequence of defining the line segment, the two lines generated by Eqs. (3.8) and (3.9) become two line segments. The surface color is the intersection of those line segments. The important point is that *when the intersection divides a line segment in  $p : 1 - p$ , the illumination color  $\mathbf{e}^1 = \{e_r^1, e_g^1\}$  divides the Illumination line segment in  $p : 1 - p$ ,*

as illustrated in Figure 3.9. Let one line segment generated from  $\mathbf{i}^1 = \{i_r^1, i_g^1\}$  be Line 1, and the other line segment generated from  $\mathbf{i}^2$  be Line2. When the intersection  $\mathbf{s} = \{s_r, s_g\}$  internally divides Line 1 in  $p : 1 - p$ , the illumination color  $\mathbf{e}^1$  would be the point that divides the Illumination line segment in  $p : 1 - p$ .

Similarly, when the intersection  $\mathbf{s}$  internally divides Line 2 in  $q : 1 - q$ , the illumination color  $\mathbf{e}^2$  would be the point that divides the Illumination line segment in  $q : 1 - q$ . If the intersection does not exist on both lines, we could consider that the estimation contain errors.

This can be proved as follows. From Eqs. (3.5) and (3.6),

$$\begin{bmatrix} s_r \\ s_g \end{bmatrix} = \begin{bmatrix} i_r^1 & 0 \\ 0 & i_g^1 \end{bmatrix} \begin{bmatrix} 1/e_r^1 \\ 1/e_g^1 \end{bmatrix} \quad (3.20)$$

$$\begin{bmatrix} s_r \\ s_g \end{bmatrix} = \begin{bmatrix} i_r^2 & 0 \\ 0 & i_g^2 \end{bmatrix} \begin{bmatrix} 1/e_r^2 \\ 1/e_g^2 \end{bmatrix}. \quad (3.21)$$

Namely, Eq. (3.7) of the Illumination line (Figure 3.9, right) can be converted to Eq. (3.8) of a line (Figure 3.9, left, Line 1) by a simple scaling as expressed in Eq. (3.20). Scaling does not change the ratio of internal division. Thus, when the intersection  $\mathbf{s}$  internally divides Line 1 in  $p : 1 - p$ , the illumination color  $\mathbf{e}^1$  would be the point that divides the Illumination line in  $p : 1 - p$ .

### 3.5.2 Detecting the Estimation error

The implementation of detecting the estimation error is as follows. Suppose that we generate a line segment from an image chromaticity, and let the coordinates of its start and end points be  $(l_{rmin}^1, l_{gmin}^1)$  and  $(l_{rmax}^1, l_{gmax}^1)$ . Let the other line segment's start and end points be  $(l_{rmin}^2, l_{gmin}^2)$  and  $(l_{rmax}^2, l_{gmax}^2)$ . The coordinate of the intersection point is  $(s_r, s_g)$ . The intersection point exists on both line segments if and only if,

$$l_{rmin}^1 \leq s_r \leq l_{rmax}^1 \quad \text{and} \quad (3.22)$$

$$l_{rmin}^2 \leq s_r \leq l_{rmax}^2. \quad (3.23)$$

The above condition may be rewritten as follows by using the g-coordinate.

$$l_{gmin}^1 \leq s_g \leq l_{gmax}^1 \quad \text{and} \quad (3.24)$$

$$l_{gmin}^2 \leq s_g \leq l_{gmax}^2 \quad (3.25)$$

We can determine whether the estimation has an error or not using either the equations (3.22) and (3.23), or (3.24) and (3.25).

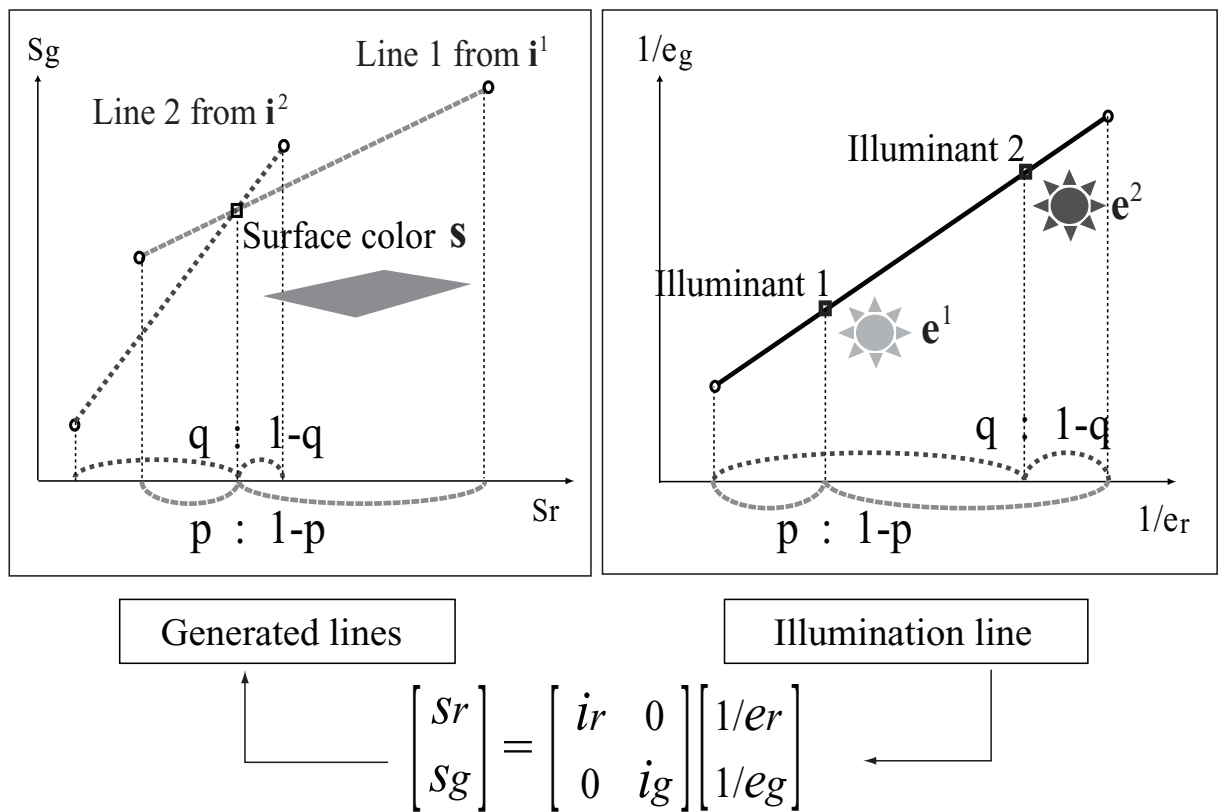


Figure 3.9: Lines 1 and 2 are generated by  $i^1$  and  $i^2$ . When the intersection  $s$  divides Line 1 in  $p : 1 - p$ , the light color  $e^1$  divides the Illumination line in  $p : 1 - p$ .

### 3.5.3 Correcting the Error of Input Image Chromaticity

The following describes a method to reduce the estimation error by correcting the input error. When the intersection does not exist on both line segments, the estimation must have failed because of input errors. Therefore, the method selects one of the input image chromaticities and adjusts it so that the intersection will be on both lines. Since an input image chromaticity determines the gradient and the intercept of the generated line, it can change the position of the intersection.

Input image chromaticities consist of the four following values  $i_r^1$ ,  $i_g^1$ ,  $i_r^2$ , and  $i_g^2$ , but we only adjust one of them. If we allow two values to change, one can move the intersection to an arbitrary position in many ways. How to select one from four values is explained in the next subsection.

The correction value can be constrained using Eqs. (3.22) and (3.23), or (3.24) and (3.25). We can assume that  $i^2$  is redder, or has a lower color temperature, than  $i^1$  without loss of generality. When the value  $i_g^2$  is selected, for instance, Eqs. (3.22) and (3.23) determine the range of possible  $\tilde{i}_g^2$  value. By substituting Eq. (3.10) into Eqs. (3.22) and (3.23), the range for the adjusted value  $\tilde{i}_g^2$  can be calculated:

$$i_g^1 \frac{i_r^2 (l_{r\min}^* \frac{m}{c} + i_r^1)}{i_r^1 (l_{r\min}^* \frac{m}{c} + i_r^2)} \leq \tilde{i}_g^2 \leq i_g^1 \frac{i_r^2 (l_{r\max}^* \frac{m}{c} + i_r^1)}{i_r^1 (l_{r\max}^* \frac{m}{c} + i_r^2)} \quad \text{where } * = \{1, 2\}$$

The current value  $i_g^2$  will be adjusted to the nearest  $\tilde{i}_g^2$  that satisfies the last equation.

In the case where we select  $i_r^2$  for adjustment, the range for  $\tilde{i}_r^2$  can be calculated in a similar way.

$$i_r^1 \frac{i_g^2 (l_{g\max}^* \frac{1}{c} - i_g^1)}{i_g^1 (l_{g\max}^* \frac{1}{c} - i_g^2)} \leq \tilde{i}_r^2 \leq i_r^1 \frac{i_g^2 (l_{g\min}^* \frac{1}{c} - i_g^1)}{i_g^1 (l_{g\min}^* \frac{1}{c} - i_g^2)} \quad \text{where } * = \{1, 2\}$$

where it assumes  $l_{g\min}^* \frac{1}{c} - i_g^2 > 0$ .

### 3.5.4 Selecting the Input Image Chromaticity to be Corrected

There is an issue of selecting one from four image chromaticity values,  $i_r^1$ ,  $i_g^1$ ,  $i_r^2$ , and  $i_g^2$ , to be adjusted. Selecting input  $i^1$  or input  $i^2$  would make no difference in illumination color estimation as shown in Figure 3.10. The left of Figure 3.10 is the case of selecting  $i_g^1$  and the right is the case of selecting  $i_g^2$ . Even if we adjust  $i_g^1$  or  $i_g^2$ , the new intersection would internally divide each line segment in the same ratio. As mentioned in 3.5.1,

the ratio determines the illumination colors, and thus the estimated results would be unchanged in both cases.

On the other hand, a different estimation results depending on which channel to select,  $r$  or  $g$ . Therefore, we calculate the effectiveness of each channel for the estimation and select the one that has greater effectiveness. We define the effectiveness  $\alpha$  as

$$\alpha = \left| \frac{(i_r^2 - i_r^1) i_g^2}{(i_g^2 - i_g^1) i_r^2} \right| \quad (3.26)$$

The above equation assumes that the input  $\mathbf{i}^1$  is going to be adjusted. If  $\alpha$  is larger than 1, a small difference in channel  $g$  affects the estimation compared to channel  $r$  and therefore the method selects channel  $g$  to be adjusted. Otherwise, channel  $r$  will be selected.

The detailed derivation of the effectiveness  $\alpha$  is as follows. As aforementioned in Table 3.1, when  $i_g^1$  has noise  $\Delta i_g^1$ , then the error ratio of estimated surface chromaticity becomes

$$\begin{aligned} \frac{\Delta s_{rg}}{s_r} &= \frac{\Delta i_g^1}{i_g^1} \frac{-1}{1 + \frac{\Delta i_g^1}{i_g^1} - \frac{i_r^1/i_g^1}{i_r^2/i_g^2}} \frac{(i_r^2 - i_r^1) i_g^2}{(i_g^2 - i_g^1) i_r^2} \approx \frac{\Delta i_g^1}{i_g^1} \frac{-1}{1 - \frac{i_r^1/i_g^1}{i_r^2/i_g^2}} \frac{(i_r^2 - i_r^1) i_g^2}{(i_g^2 - i_g^1) i_r^2} \\ &\approx -\frac{\Delta s_{rr}}{s_r} \frac{(i_r^2 - i_r^1) i_g^2}{(i_g^2 - i_g^1) i_r^2}. \end{aligned} \quad (3.27)$$

This shows that even the error ratio of  $i_r^1$  and  $i_g^1$  are the same, the effect on the estimation error ratio depends on the factor  $\left| \frac{(i_r^2 - i_r^1) i_g^2}{(i_g^2 - i_g^1) i_r^2} \right|$ . We derived the factor using  $\Delta s_r/s_r$ , but the same can be derived by using  $\Delta s_g/s_g$ .

### 3.5.5 Experiments

#### Evaluation with Macbeth color checker

**Method** We conducted experiments to evaluate the proposed method. Images of the GretagMacbeth ColorChecker were taken under six illuminants using SONY DXC-9000 progressive 3 CCD digital cameras by setting its gamma correction off. Images that are taken are shown in Figure 3.11. From Figure 3.11 (a) through (f), the color of the illuminant gradually changes from red to blue. The colors of the illuminants plotted

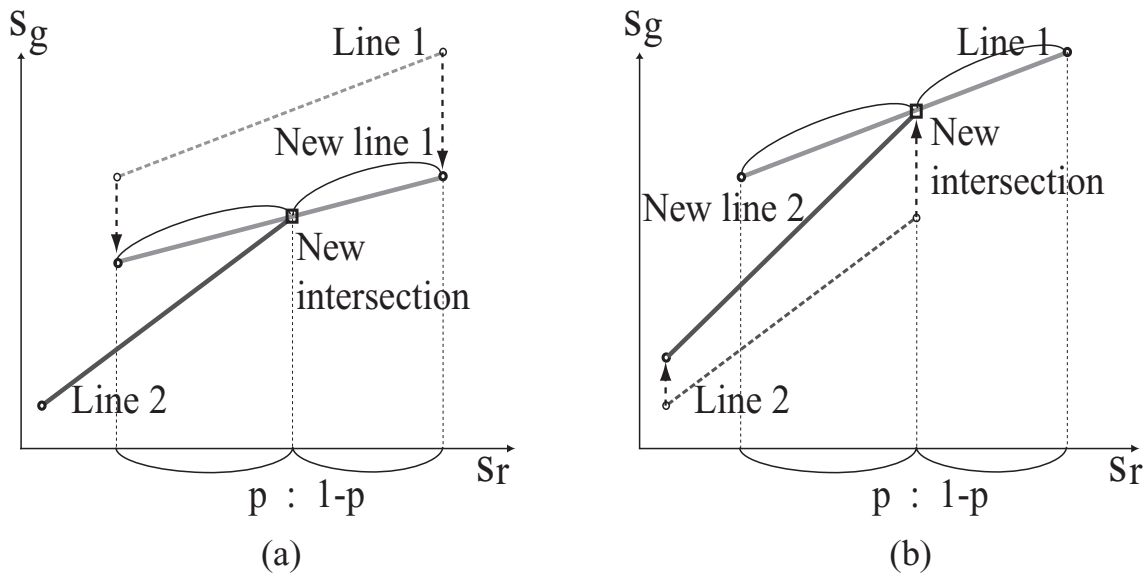


Figure 3.10: (a) The case of adjusting  $i_g^1$ . (b) The case of adjusting  $i_g^2$ . The ratio  $p$  does not change in either case.

in the inverse-chromaticity space are shown in Figure 3.12 (a), L1 through L6, and one of their measured spectral distributions is shown in Figure 3.12 (b). The details of six illuminants are shown in Table 3.3. We have cut out each image of eighteen surface color patches, those surrounded by the red dotted line in Figure 3.11 (a), and prepared  $18 \times 6$  color patch images. Each was resized to  $70 \times 70$  pixels.

Having selected a pair of color patch images whose surface color is identical, we randomly chose one pixel from each image and estimated their illumination chromaticities. This was repeated 50,000 times for a pair. The same was done with the previous method [FFB95] for comparison. The total combination number of two illuminants and a surface was  ${}^6C_2 \times 18 = 270$ .

**Results** From the results of the 270 experiments, we obtained Figures 3.13, 3.14, 3.15, 3.16, 3.17, 3.18, 3.19, 3.20, and 3.21. Each row of those figures shows a pair of input images, estimated chromaticities (of two illuminants and a surface) obtained by the proposed method, the ground truth, and the previous method [FFB95]. Each figure includes two surfaces that provided similar results to each other. Authors selected the order of the figures so that the effectiveness of the proposed methods becomes clearer

<sup>5</sup>Correlated Color Temperature.



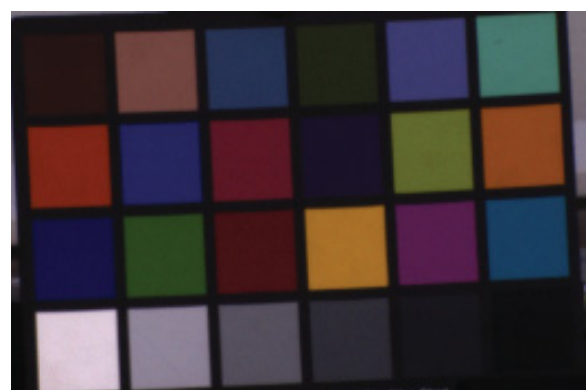
(a) Image taken under L1.



(b) Image taken under L2.



(c) Image taken under L3.



(d) Image taken under L4.

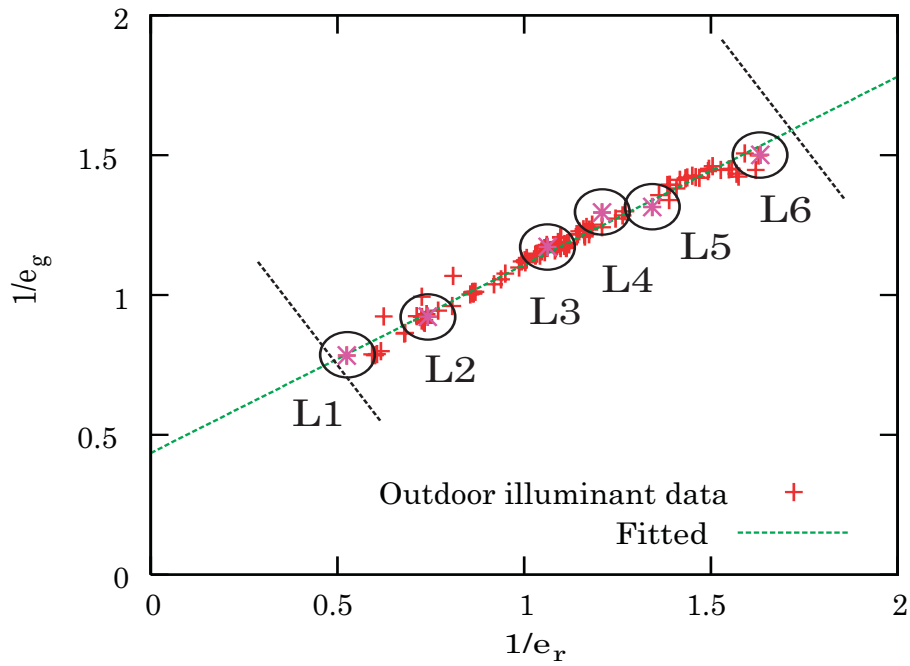


(e) Image taken under L5.

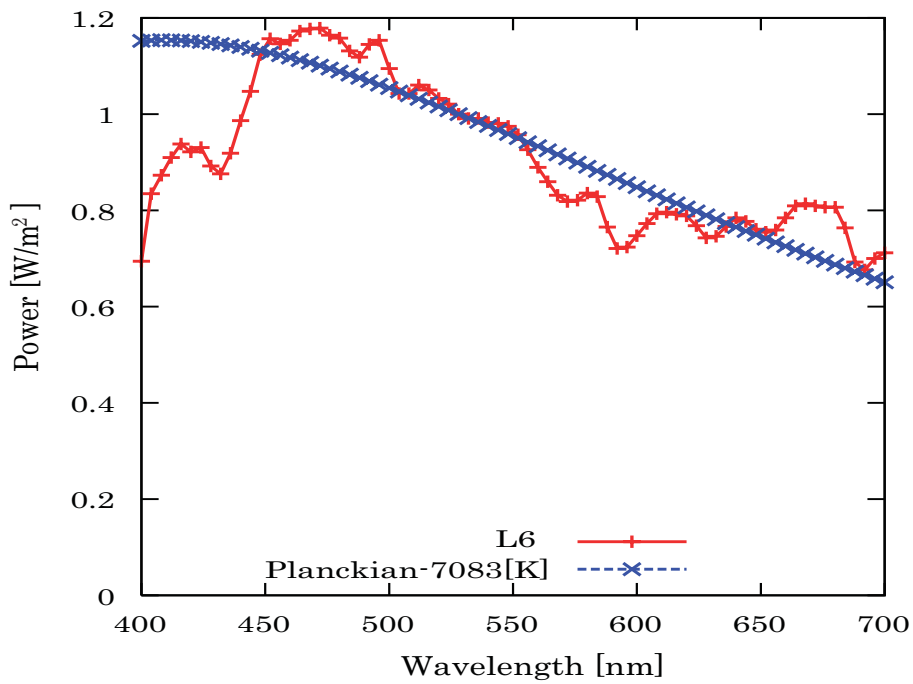


(f) Image taken under L6.

Figure 3.11: Images of the Macbeth ColorChecker taken under different outdoor illuminants (L1 to L6). Illuminant's color gradually changes from (a) to (f). Eighteen surface colors (colors surrounded by the red dotted line) were used in the experiments.



(a) Six illuminants used in the experiments.



(b) The spectral distribution of L6.

Figure 3.12: (a) Six illuminants which are plotted in the inverse-chromaticity space. (b) The spectral distribution of L6 is shown as an example. The spectrum also shown is the blackbody radiation curve of 7083 K.

Table 3.3: Details of six illuminants used in the evaluation experiments.

Illuminants	Details	CCT <sup>5</sup> (K)
L1	2003/8/22 17:30, Tokyo, Outdoor illumination, Fine day	3539
L2	2007/3/16 16:30, Tokyo, Outdoor illumination, Cloudy day	4083
L3	2003/3/16 15:30, Tokyo, Outdoor illumination, Cloudy day	5130
L4	2003/3/16 13:00, Tokyo, Outdoor illumination, Cloudy day	5632
L5	2003/7/14 14:30, Tokyo, Outdoor illumination, Cloudy day	5991
L6	2003/7/14 18:20, Tokyo, Outdoor illumination, Cloudy day	7083

to the readers.

In Figures 3.13, 3.14, 3.15, 3.16, 3.17, 3.18, and 3.19, it is clear to see that the proposed method improves the previous methods' [FFB95] results. The bottom rows in the figures show the average of the estimated surface colors by each method. We can see that if we take the average of the estimated surface color, the results can be much improved. However, some of the previous method's [FFB95] results can be very unstable, while they can be stably estimated by the proposed method.

In order to numerically evaluate our method, we took the histograms of the estimation errors of two illuminants and a surface; they are shown in Figure 3.22. Here, the estimation error is defined as the Euclidean distance between the estimated and true chromaticities in CIE LAB color space. The average estimation errors of the proposed method were 8.6 (redder illuminants  $e^1$ ), 8.7 (bluer illuminants  $e^2$ ) and 8.0 (surfaces.) Those of the previous method [FFB95] were 104.2 (redder illuminants), 98.6 (bluer illuminants) and 74.2 (surfaces.) The previous method provides larger errors than 10.0 [CIE LAB] (surfaces) in 150 data sets, while the proposed method provides 122. The previous method provides larger errors than 30.0 [CIE LAB] (surfaces) in 47 data sets, while the proposed method provides none. The proposed method surpasses the previous method in terms of both the average and the maximum error values.

As an example, we show the results when selecting L1 and L6 for illuminants and Blue sky for a surface color (shown in Figure 3.20 (a).) We sampled a pixel randomly from each color patch image, performed the estimation, and repeated this for 50,000 times. Distributions of the two estimated chromaticities (of L1 and L6) are shown in

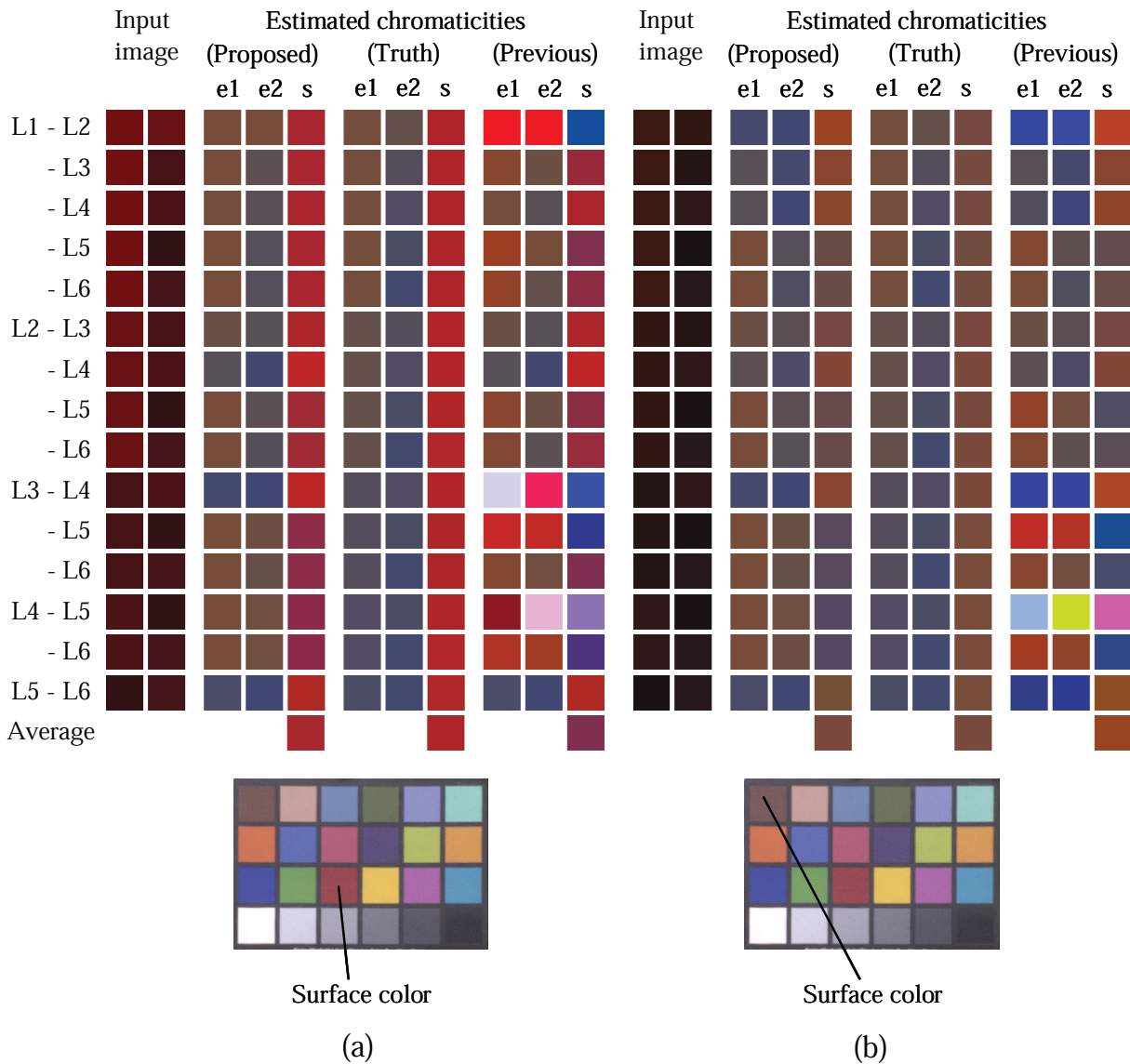


Figure 3.13: The figure shows the results of using (a) Red, and (b) Dark skin, of the Macbeth chart. Each row shows a pair of input images, estimated chromaticities (of two illuminants and a surface) obtained by the proposed method, the ground truth, and the previous method [FFB95]. L1 to L6 are the outdoor illuminants that are used; there are  ${}_6C_2 = 15$  rows for each surface color. The bottom row shows the average of the estimated surface colors by each method.

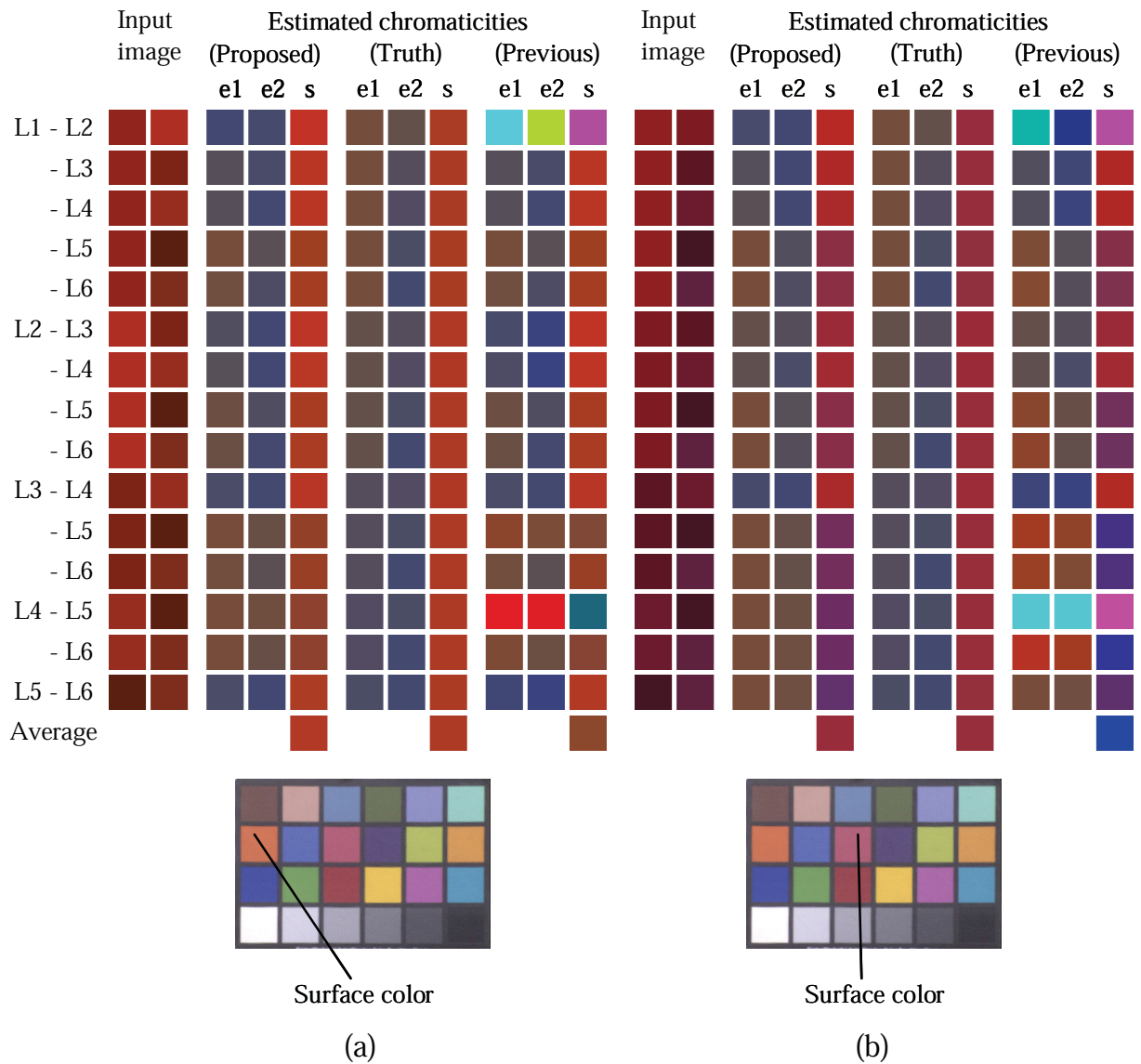


Figure 3.14: The figure shows the results of using (a) Orange, and (b) Moderate red, of the Macbeth chart.

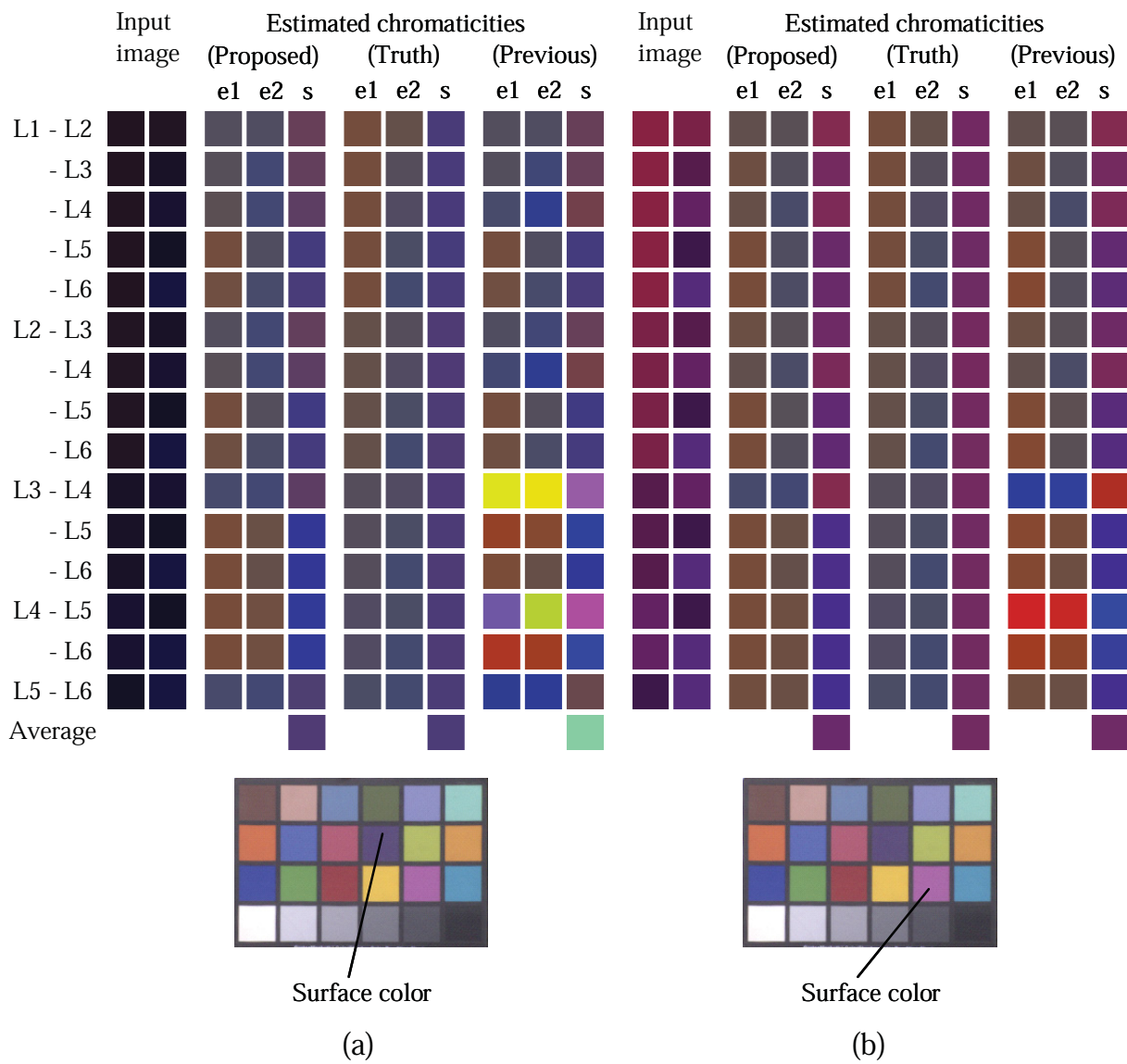


Figure 3.15: The figure shows the results of using (a) Purple, and (b) Magenta, of the Macbeth chart.

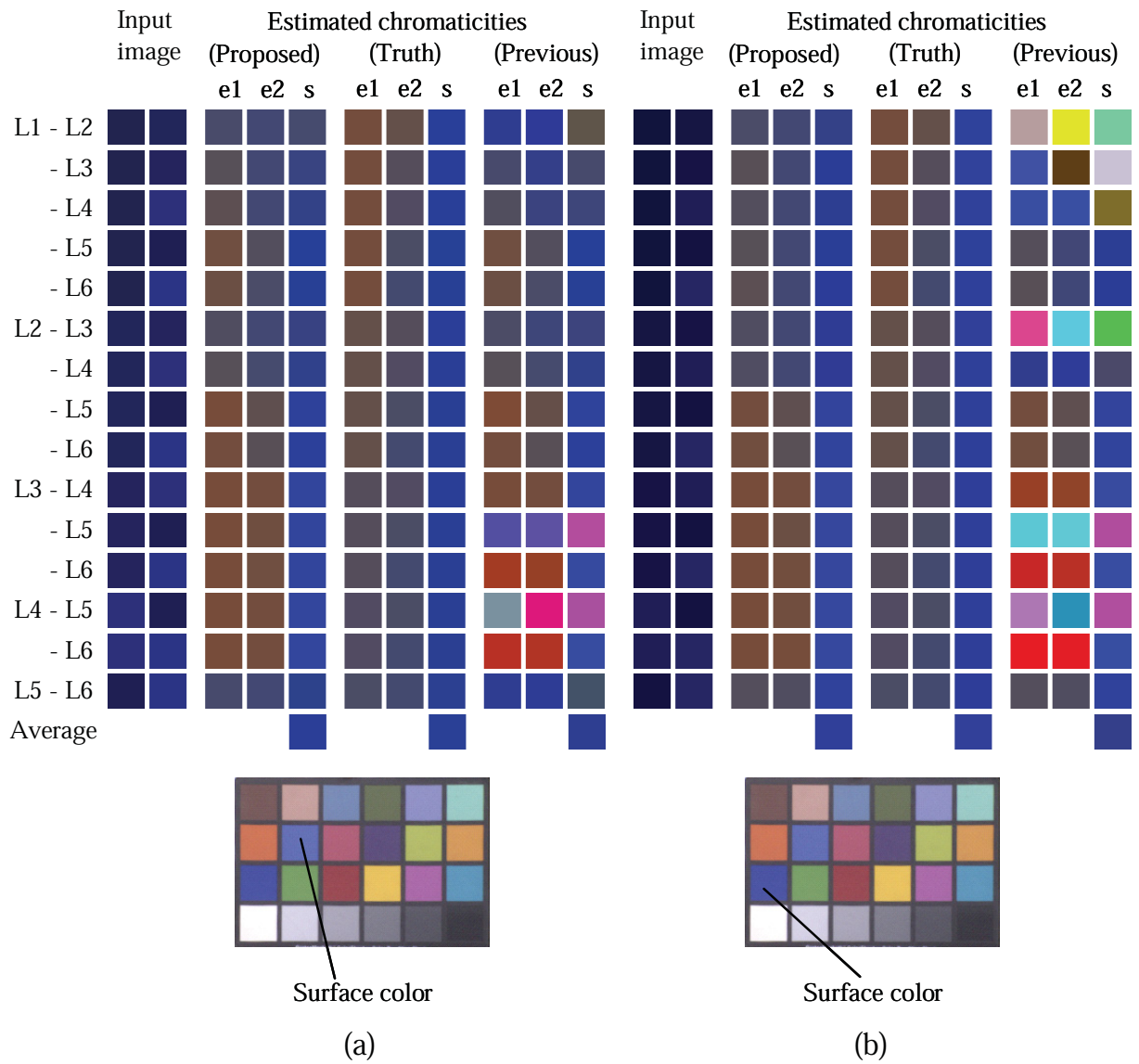


Figure 3.16: The figure shows the results of using (a) Purplish blue, and (b) Blue, of the Macbeth chart.

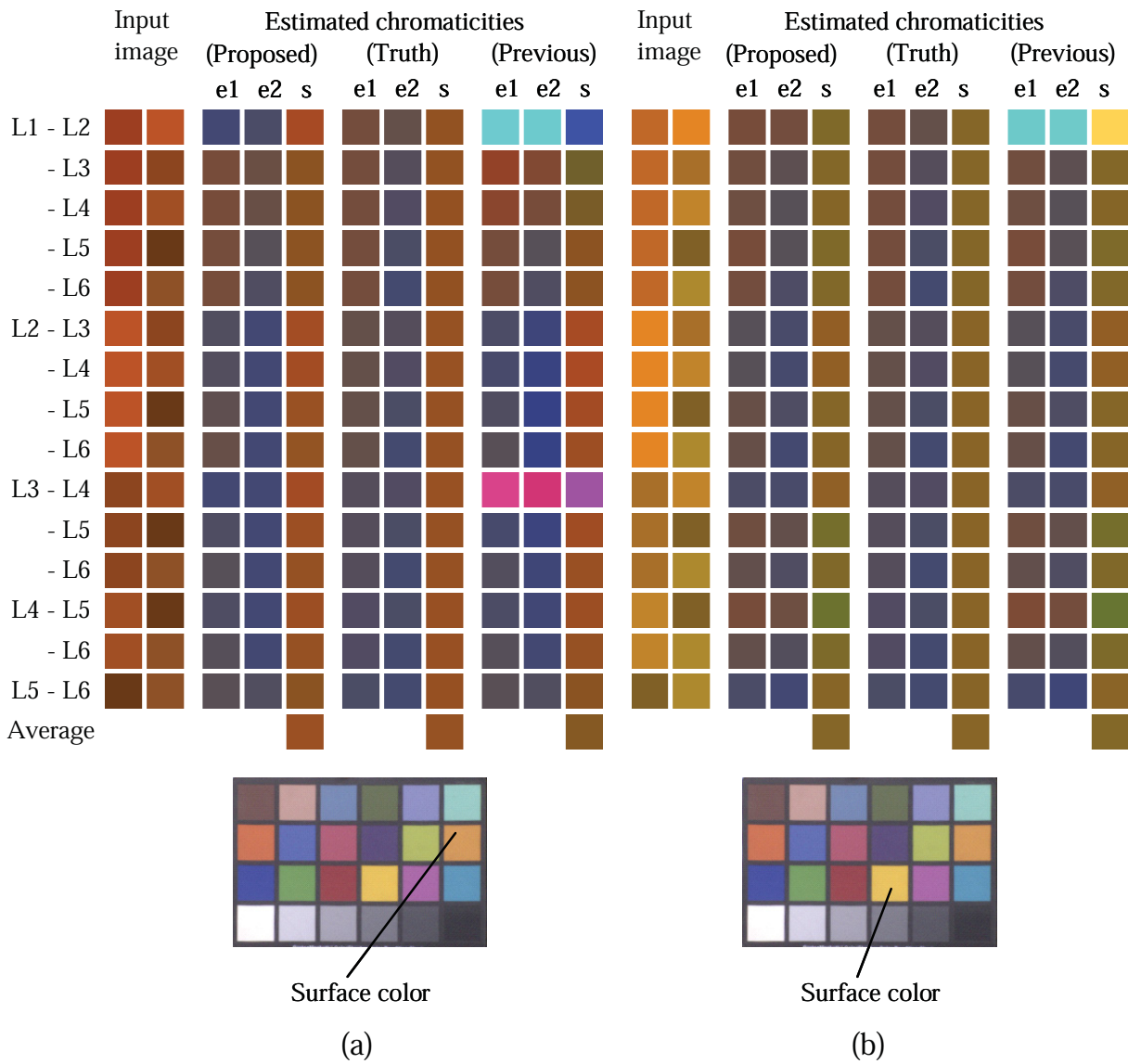


Figure 3.17: The figure shows the results of using (a) Orange yellow, and (b) Yellow, of the Macbeth chart.

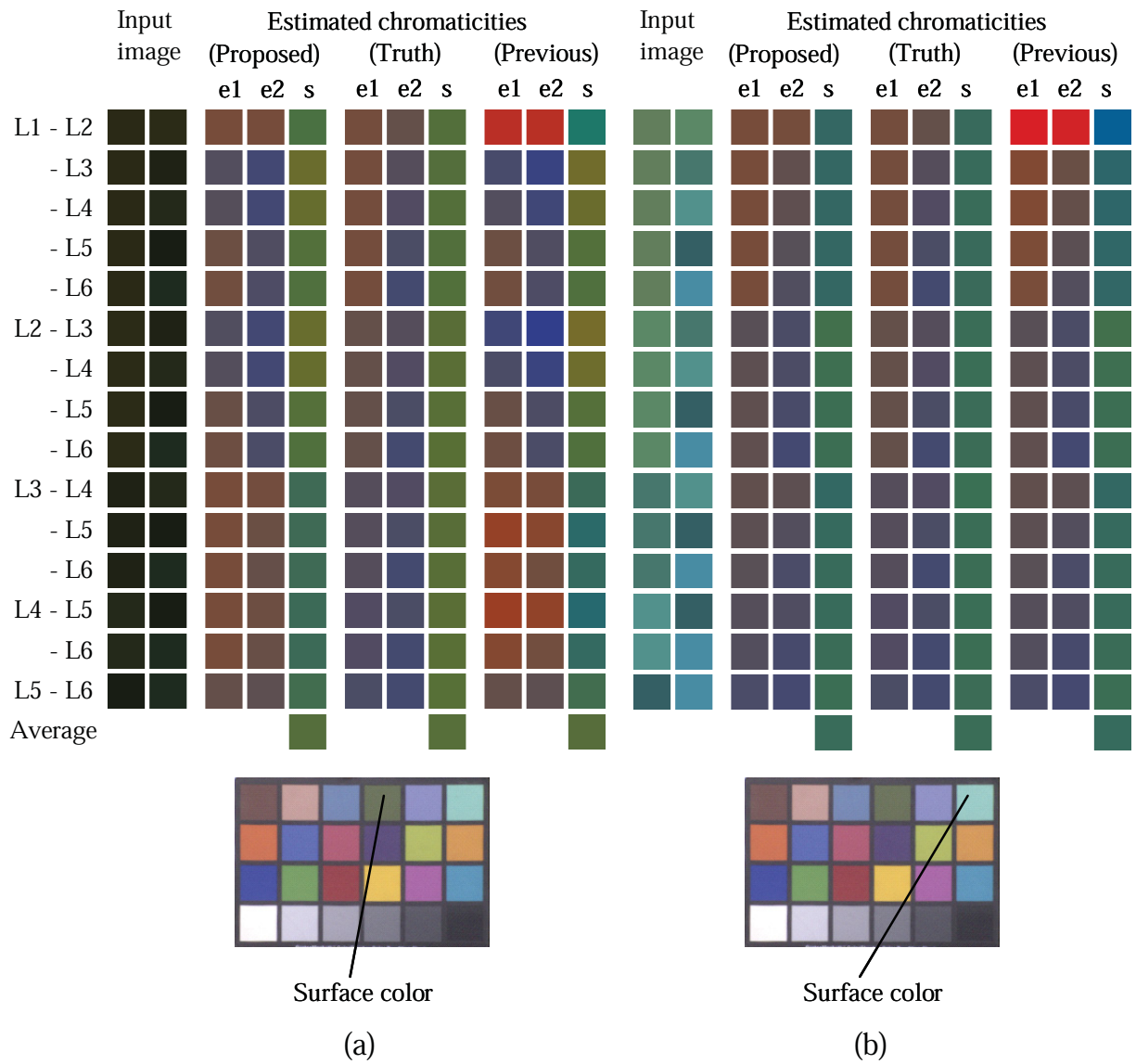


Figure 3.18: The figure shows the results of using (a) Foliage, and (b) Bluish green, of the Macbeth chart.

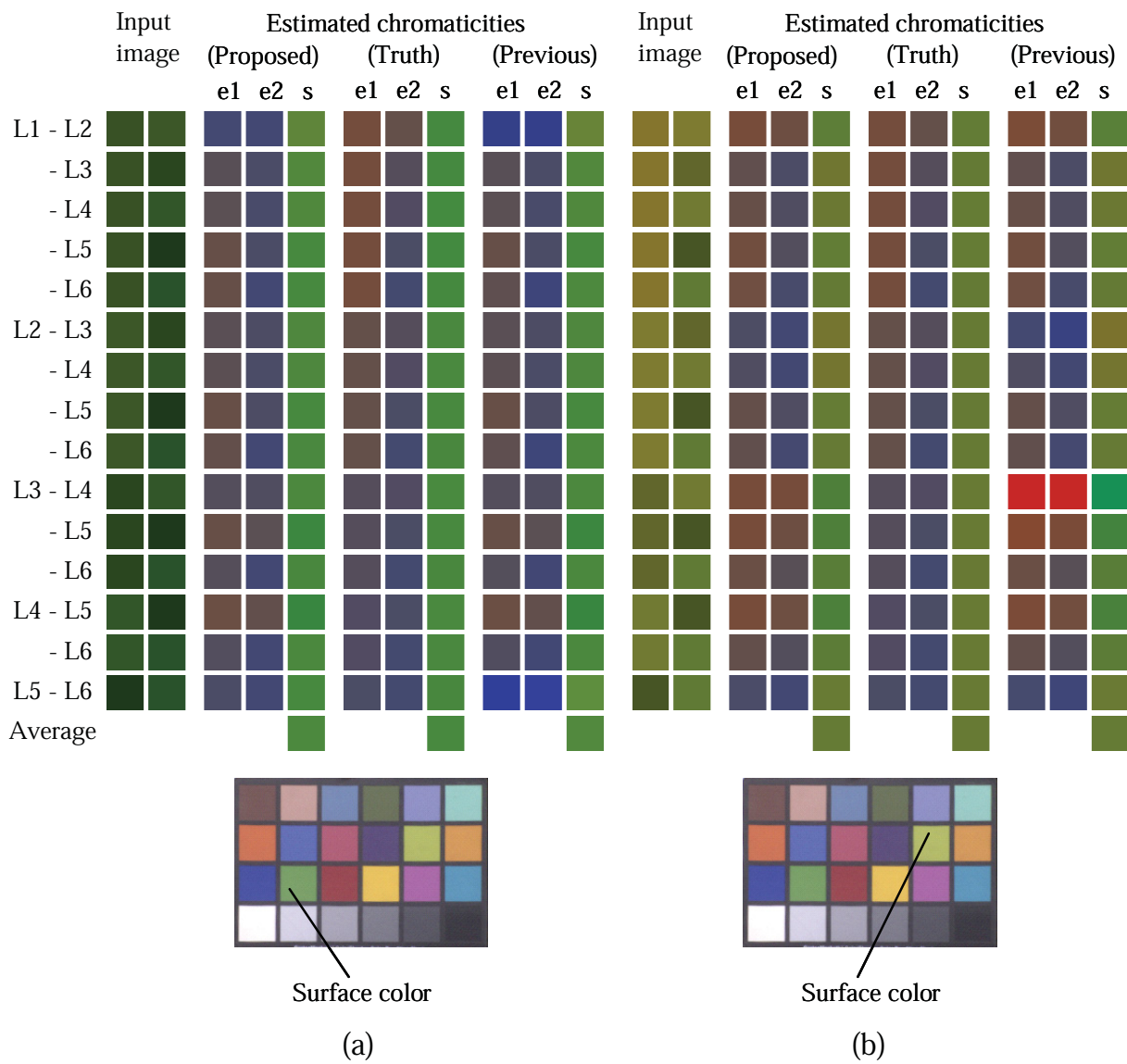


Figure 3.19: The figure shows the results of using (a) Green, and (b) Yellow green, of the Macbeth chart.

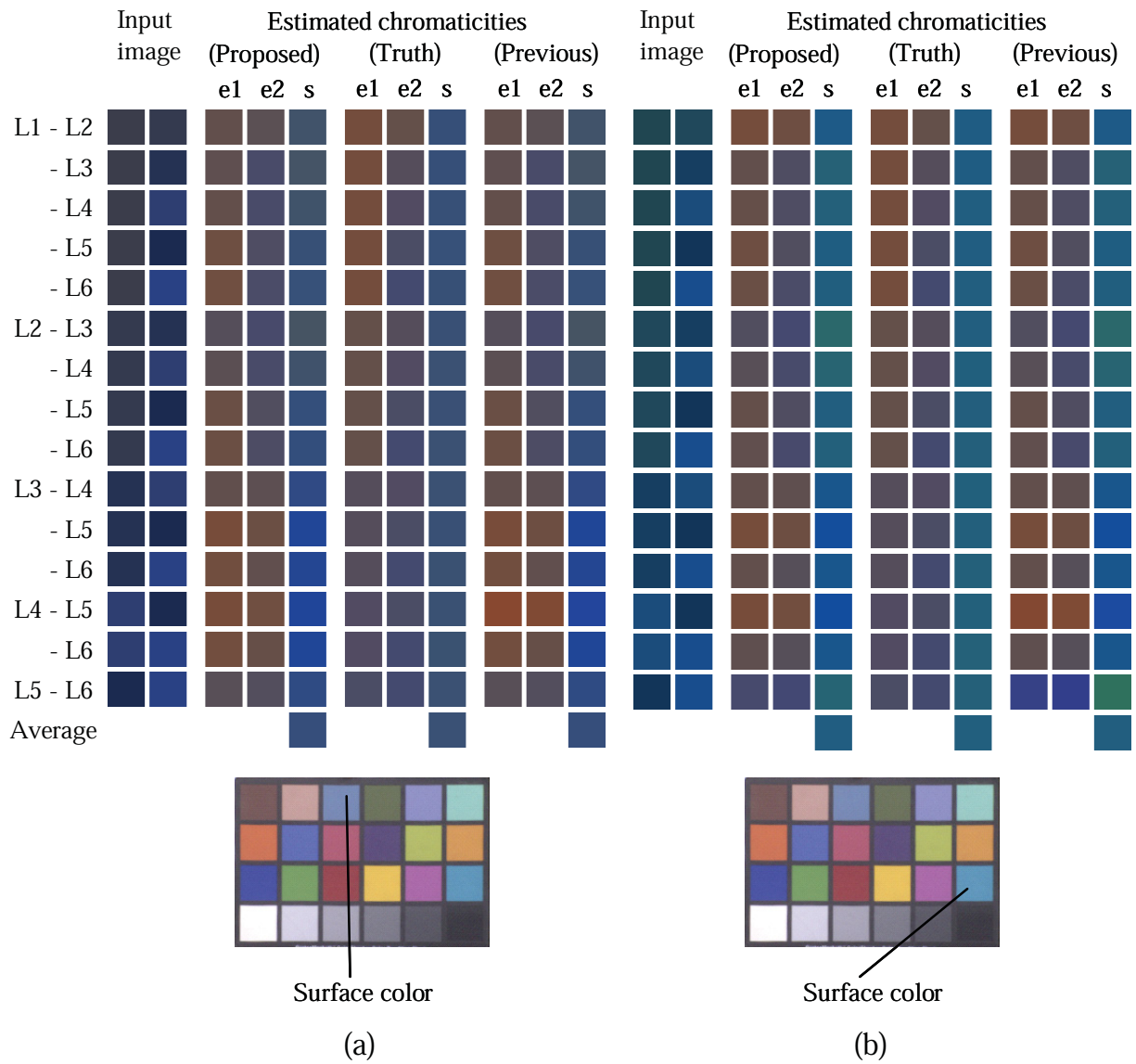


Figure 3.20: The figure shows the results of using (a) Blue sky, and (b) Cyan, of the Macbeth chart.

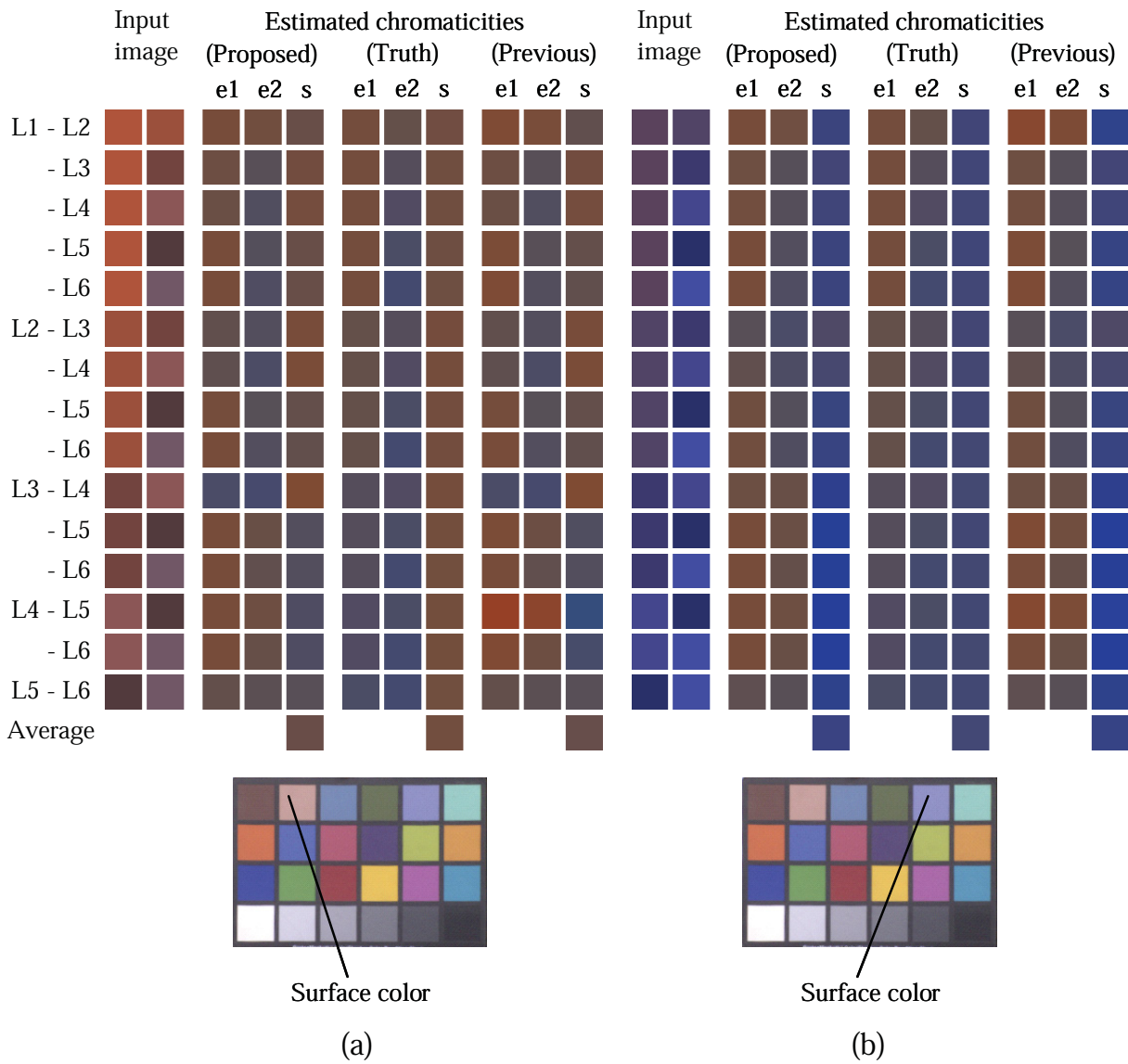


Figure 3.21: The figure shows the results of using (a) Light skin, and (b) Blue flower, of the Macbeth chart.

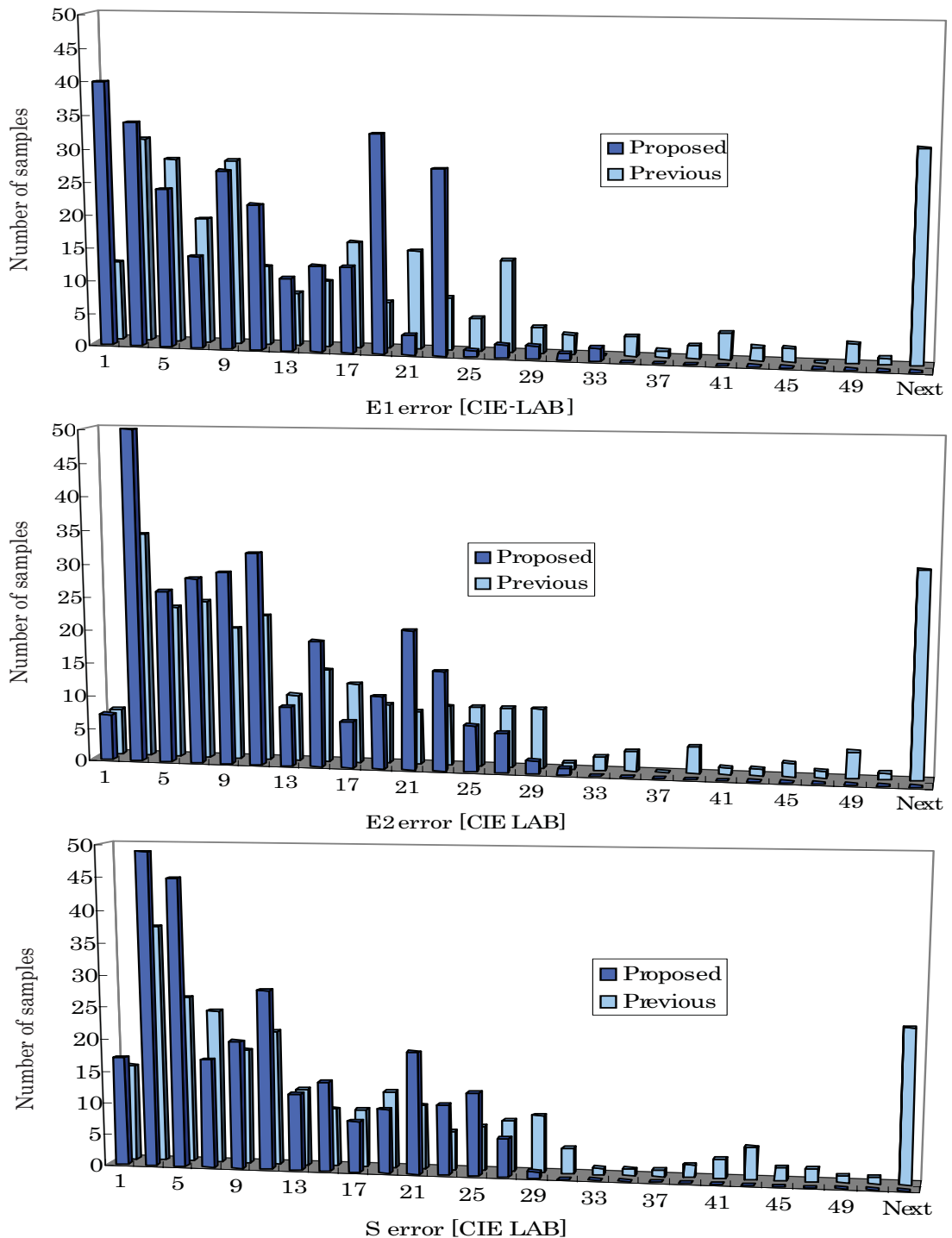


Figure 3.22: Histograms of estimation errors of the illuminant 1;  $e^1$  (top), illuminant 2;  $e^2$  (middle), and surface;  $s$  (bottom). The estimation error is defined as the Euclidean distance between the estimated and true chromaticities in CIE LAB color space. The averages of the proposed method were 8.6 (redder illuminants  $e^1$ ), 8.7 (bluer illuminants  $e^2$ ) and 8.0 (surface  $s$ ). Those of the previous method [FFB95] were 104.2 (redder illuminants  $e^1$ ), 98.6 (bluer illuminants  $e^2$ ) and 74.2 (surface  $s$ ).

Figures 3.23 (a) and (b). Figures 3.23 (a) and (b) show the distributions of estimated colors of L1 and L6, respectively. The color temperature difference between L1 and L6 was 142 mired.

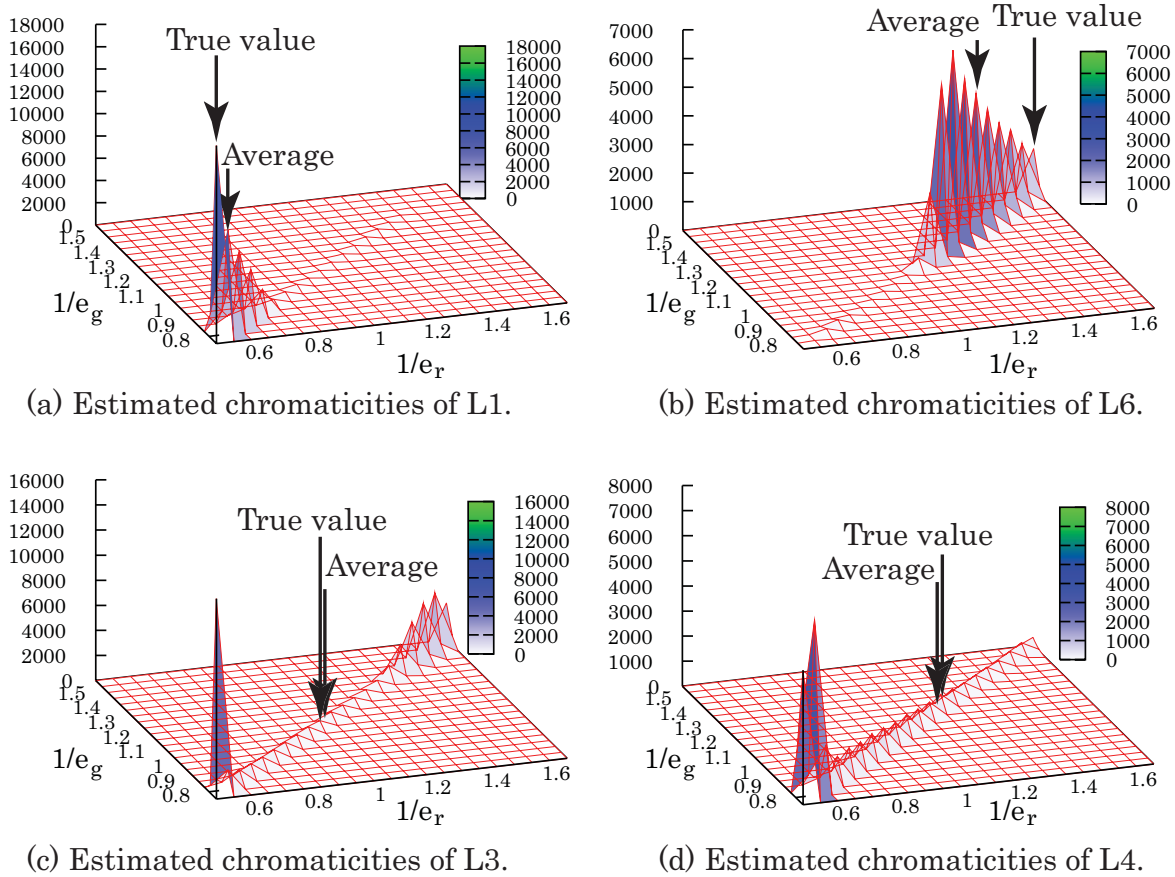


Figure 3.23: The estimated illumination chromaticities' distribution in an inverse-chromaticity space. Estimated values are restrained on the defined line segment. In (c) and (d), the estimated values were more widely spread compared to (a) and (b), due to the less color difference of illuminations.

As Figs. 3.23 (a) and (b) show, estimated chromaticities are restrained on a specific range. They tend to concentrate on the end-points of the line segment. The reason for this is that when an intersection by the proposed method is made, one of the estimated illumination chromaticities would always be one of the end-points of the line segment.

The averages  $(\frac{1}{e_r}, \frac{1}{e_g}, \frac{1}{e_b})$  of the distributions of L1 were (0.609, 0.845, 1.0) from Figure 3.23 (a), and the ground truths obtained by the standard white reference were (0.525, 0.784, 1.0.) Those of L6 from Figure 3.23 (b) were (1.41, 1.38, 1.0), and the truths

were (1.63, 1.50, 1.0.) The color differences between those values were 3.6 for L1, 3.8 for L6, and 3.1 for the surface, in CIE LAB space.

We showed other results in Figures 3.23 (c) and (d), which were obtained by selecting L3 and L4 for illuminants and Blue sky for the surface. The color temperature difference between L3 and L4 was 78 mired, and this is lower than our recommended color difference, 100 mired. Consequently, the estimated values were more widely spread compared to Figures 3.23 (a) and (b). The averages of L3 were (1.06, 1.15, 1.0) and the ground truths were (1.06, 1.17, 1.0). Those of L4 were (1.18, 1.23, 1.0), and the truths were (1.21, 1.30, 1.0). The color differences between them were 0.9 (L3), 2.3 (L4), and 1.1 (the surface) in CIE LAB. As Figures 3.23 (c) and (d) shows, one estimation is less reliable, and therefore it is better to do the estimation repeatedly and calculate the average as we did in this experiment.

### Evaluation with outdoor object

**Method** We conducted experiments on real images, taken using a SONY DXC-9000, a progressive 3 CCD digital camera, by setting its gamma correction off. To ensure that the outputs of the camera were linear to the flux of incident light, we used a spectrometer: Photo Research PR-650. We used planar and convex objects to avoid interreflection, and excluded saturated pixels from the computation. For evaluation, we compared the results with the average values of image chromaticity of a white reference image (Photo Research Reflectance Standard model SRS-3), captured by the same camera.

In our implementation, we captured two images of a scene from a fixed object and camera position but under different illumination. From the same pixel location of the two images, we convert the sensor response values into image chromaticity values. Surface and illumination colors are calculated from those inputs, and we eliminated the illumination color from input images by using the estimated values.

**Results** Figure 3.24 (a) and 3.24 (b) show input image chromaticities of pixels taken from an outdoor object illuminated by cloudy sky-light at 15:00 and 18:00. The actual surface color obtained by using the standard white reference is shown in 3.24 (c). Figure 3.24 (d) shows our surface color estimation, while 3.24 (e) is produced by Finlayson et al.'s method. We have several conditions of experiment with the same object, and our estimation produced consistent results, while the results of Finlayson et al.'s method

were so inconsistent that the result could be green or blue, which is far from the ground truth.

Figure 3.25 (a) shows a scene of one of our two input images. This image was taken at 18:05 illuminated by cloudy daylight. Another input (Figure 3.25 (b)) was taken at 15:05 also illuminated by cloudy daylight on the same day. Figure 3.25 (c) shows our estimation result of the image. To produce this image, we considered only pixels whose intensities are not saturated and above camera dark. We computed the average of the estimated illumination color of image shown in Figure 3.25 (a), and normalized that image. Note that we excluded the needles of the tower's clock as well as moving leaves from the computation by evaluating the image chromaticity difference. Figure 3.25 (d) is the result based on the standard white reference which shows that our result is quite good.

Results from images that are taken from different view points are shown in Figure 3.27. Figures 3.27 (a) and (b) are the input images, which were taken at 18:00 with cloudy illumination on different days. Those images were aligned by using a 3D shape of the object. Other alignment techniques such as homography can be alternatively used. Figure 3.27 (c) shows our estimation result of the image, and Figure 3.27 (d) is the result based on the standard white reference. From those results, we found that the method produces convincing results with images that have small difference in illumination. Also, we found that the camera view point can be arbitrary.

## 3.6 Proposed method II: Using Shadows

This section proposes a method to accomplish the illumination color estimation from a single image. The method uses shadowed and non-shadowed regions in an image. Previous researchers (for example, [FF94]) have found that shadowed regions are illuminated by sky light, while non-shadowed regions are illuminated by the combination of sky light and sunlight. Based on this difference of illuminations in shadowed and non-shadowed regions, we estimate illumination colors for both sunlight and sky light and then remove them. Note that illumination colors are assumed to be uniform inside each region.

**Blackbody Radiation** The blackbody assumption assumes that natural (outdoor) illumination can be approximated by blackbody radiation, and modeled by Planck's

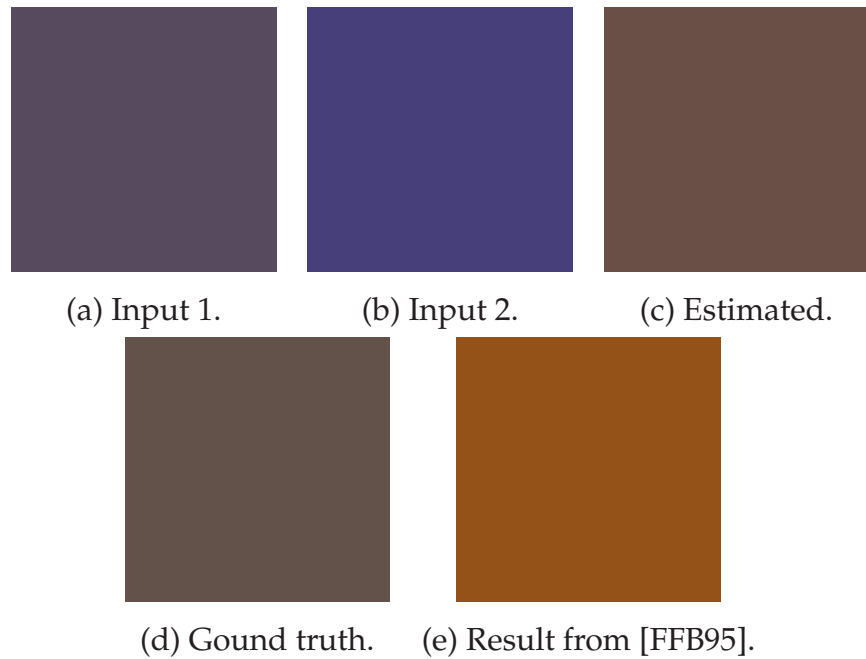


Figure 3.24: Comparison results between our proposed method and Finlayson et al.'s method.

formula:

$$M(\lambda) = c_1 \lambda^{-5} [\exp(c_2/\lambda T) - 1]^{-1} \quad (3.28)$$

where  $c_1 = 3.7418 \times 10^{-16} \text{ Wm}^2$ ,  $c_2 = 1.4388 \times 10^{-2} \text{ mK}$ ,  $\lambda$  is wavelength (m), and  $T$  is temperature in Kelvin. By combining with known sensor sensitivity, we can obtain a camera response of Planck's formula:

$$I_c = \int_{\Omega} M(\lambda, T) q_c(\lambda) d\lambda \quad c = \{R, G, B\} \quad (3.29)$$

The colors from Eq. (3.29) with different temperature  $T$  form a curved line in chromaticity space that is called the Planckian locus. The temperature is called color temperature (CT).

### 3.6.1 Shadowed and Non-shadowed Region

Color temperatures of a shadowed region and a non-shadowed region are generally different. There are two kinds of illuminants outdoors: direct sunlight and sky light. Statistically, both spectra can be approximated by blackbody radiation [FF94, JMW64]. Therefore, if we have shadowed and non-shadowed regions of the same surface in



(a) Input image taken at 18:05.



(b) Input image taken at 15:05.

Figure 3.25: (a) One of the two input scene, illuminated by cloudy daylight at 18:05.  
(b) The other input, illuminated by cloudy daylight at 15:05.



(a) Estimated result by the proposed method.



(b) Estimated by using the standard white reference.

Figure 3.26: (a) The estimated scene actual color of the image shown in Fig. 3.25 (a), computed using our proposed method. (b) The estimated scene actual color using the standard white reference.



(a) Input image taken at 18:00.



(b) Input image taken from different view at 18:00 on another day.

Figure 3.27: (a) One of the two input scene, illuminated by cloudy daylight at 18:05.  
(b) The other input, illuminated by cloudy daylight at 15:05.



(a) Estimated result by the proposed method.



(b) Estimated by using the standard white reference.

Figure 3.28: (a) The estimated scene actual color of the image shown in (a), computed using our proposed method. (b) The estimated scene actual color using the standard white reference.

an image, we can apply the method described in Section 3.5 and estimate the actual surface color.

### 3.6.2 Illumination Invariant

In order to extract two colors of the same surface from a single image, we further add a constraint to the assumption of blackbody illuminants. Previously researchers [FH01, FHLD06, MO00] have found that if we use Wien's approximation  $M(\lambda) = c_1\lambda^{-5} \exp(-c_2/\lambda T)$ , then the Planckian locus can be approximated as:

$$e_r = me_g^A \quad (3.30)$$

where  $A = \left(\frac{1}{\lambda_R} - \frac{1}{\lambda_B}\right) / \left(\frac{1}{\lambda_G} - \frac{1}{\lambda_B}\right)$ ,  $m = \frac{\lambda_G^{5A} / \lambda_B^{5A}}{\lambda_R^5 / \lambda_B^5}$ , and both are constant numbers characterizing the camera.  $\lambda_c$  (where index  $c = \{R, G, B\}$ ) is the center wavelength of the camera sensitivity.  $(e_r, e_g)$  is a chromaticity of a blackbody illuminant. If we substitute Eq. (3.30) into Eqs. (3.5) and (3.6), we obtain:

$$i_r^1 = \frac{s_r}{(s_g)^A} (i_g^1)^A \quad (3.31)$$

$$i_r^2 = \frac{s_r}{(s_g)^A} (i_g^2)^A. \quad (3.32)$$

If two pixels have an identical surface color, they will have the same values;  $i_r^1 / (i_g^1)^A = i_r^2 / (i_g^2)^A = s_r / (s_g)^A$  even though their image chromaticities are different. Therefore, we use this value as an illumination invariant and determine whether their surface color is identical. Following Marchant et al. [MO00], the value  $s_r / (s_g)^A$  is referred to as  $F$ .

If we take a logarithm of Eqs. (3.31) and (3.32), the following relations can be obtained.

$$\log(i_r^1) = \log(F) + A \log(i_g^1) \quad (3.33)$$

$$\log(i_r^2) = \log(F) + A \log(i_g^2) \quad (3.34)$$

Thus, all the chromaticities make a line in  $\log(r)$ - $\log(g)$  space as their illumination color changes. Gradients are the same constant number  $A$  determined by a camera. Chromaticities from shadowed and non-shadowed regions of the same surface colors fall on a line whose intercept is  $\log(F)$ . We classify pixels that have the same surface colors by the  $\log(F)$  value, since the space becomes linear.

Note that some surface colors can coincide in  $F$  by chance; a reddish surface cannot be distinguished from a white surface lit by a reddish sunlight. Currently, the method assumes those are not included in an image.

### 3.6.3 Implementation for Extracting Two Colors

We propose the following procedures for estimating illumination chromaticities by extracting two chromaticities of shadowed and non-shadowed regions.

1. Fit a Gaussian mixture model to the histogram of  $\log(F)$  values.
2. Select pixels that have the mean value of the Gaussian that has the maximum weight.
3. Fit a Gaussian mixture model to the histogram of  $\log(r)$  values of the selected pixels' chromaticities.
4. Select pixels that have values close to the mean value of each Gaussian.
5. Estimate illumination chromaticities using a pair of pixels randomly chosen from each selected set of pixels, repeatedly.
6. Calculate the average of estimated chromaticities.

Procedures 1 and 2 extract dominant surface colors in an image. For simplicity, the method assumes that an area of dominant surface color in an image has both shadowed and non-shadowed regions. It also assumes that if  $F$  values of two pixels are the same, their surface colors are identical. The Gaussian Mixture Model that we used was  $p(x) = \sum_{i=1}^N \xi_i G(x, \mu_i, \sigma_i^2)$ , where  $x$  is the variable,  $N$  is the number of the Gaussians,  $\xi$  is the weight, and  $G()$  is the Gaussian function whose parameters are  $\mu$  and  $\sigma^2$ . In Procedure 1, the user decides the number of Gaussians  $N$ .

Procedures 3 and 4 extract shadowed and non-shadowed pixels that have dominant surface colors. Therefore, in this case,  $N$  is set to 2 in the Gaussian fitting process. We extracted not only the pixels that have the mean value, but also the pixels close to the mean value. This is for extracting relatively large number of pixels for denoising. The threshold is set to the mean value  $\pm\sigma/2$ . All the Gaussian fittings are processed by the EM algorithm.

### 3.6.4 Experiments

#### Evaluation with toy objects

**Method** We conducted the following experiments to evaluate estimation from a single image. We placed two illuminants and target objects as Figure 3.29 (a) shows, and

took images of objects so that those images contained two chromaticities of a surface with different illuminations. The camera used was SONY DXC-9000 with its gamma correction off. The details of illuminants are shown in Table 3.4. We selected planar convex singly-colored objects as target objects. The four images taken are shown in Figure 3.29 (b)-(e).

We measured illumination colors (ground truths) by taking an image of the standard white reference every time we replaced objects.

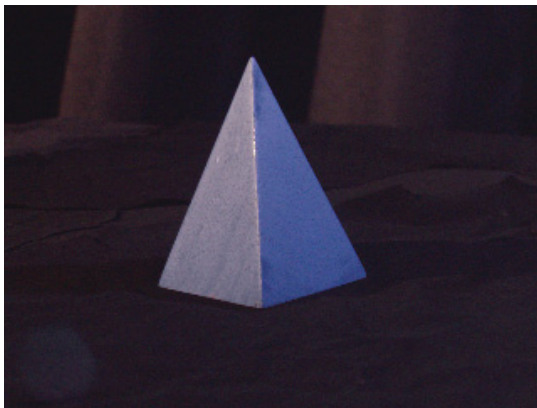
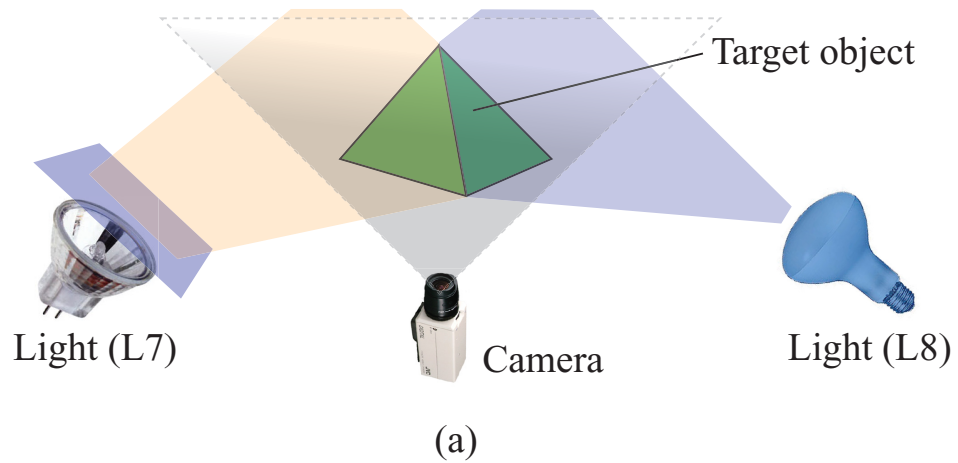
Table 3.4: Details of illuminants used in the evaluation experiments.

Illuminants	Details	CCT <sup>6</sup> (Kelvin)
L7	Halogen lamp (JCDBL100V500W, LPL Co., Ltd.) + Color filter (PolyColor B-4, Tokyo Butai Showmei Co., Ltd.)	4096
L8	Tungsten lamp with a color filter (Eyelamp PSR500WD, Iwasaki Electric Co., Ltd.)	7169/ 11763

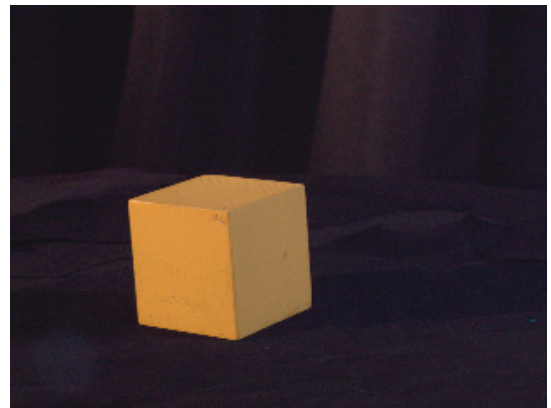
**Results** Having conducted experiments using four images shown in Figure 3.29 (a)-(e), we summarized the estimated results in Table 3.5, which shows both estimated and true chromaticities. It also shows the color difference between estimated and true chromaticities in CIE LAB space. The average color difference of the proposed method was 8.9. We also provided input image, estimated, estimated from the previous method [FFB95], and true surface chromaticities in Figures 3.30 (a), (b), (c) and (d), respectively. Figure 3.30 (e) shows the pixels chosen by the proposed method, and used for illumination color estimation. While there is room for improving the accuracy, the estimated surface chromaticities are closer to the true chromaticities than to the input chromaticities, as a result of the proposed method’s color constancy.

Gaussian fitting results are shown in Figure 3.31. The left is the Gaussian fitted to the histogram of  $\log(F)$  values, and the right is that of  $\log(r)$  values that have the selected  $F$  value. The distributions fit the Gaussians well in  $\log(F)$  and  $\log(r)$  spaces, and therefore two colors from shadowed and non-shadowed regions can be extracted successfully. The image used was Figure 3.30 (c). Two of four experiments failed to

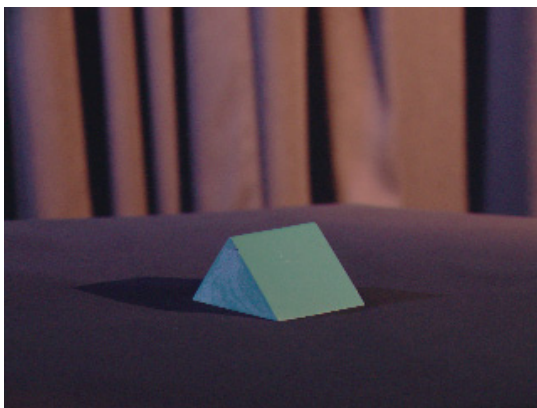
<sup>6</sup>Correlated color temperature.



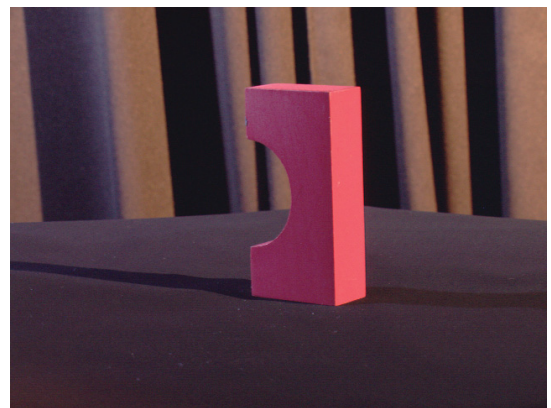
(b) Blue object.



(c) Yellow object.



(d) Green object.



(e) Red object.

Figure 3.29: Experimental setup and obtained input images: (a) We placed the target object and light sources so that each surface of the object is illuminated by different illuminants. (b) - (e) Obtained images of blue, yellow, green, and red objects.

generate the correct histograms of  $F$  values, because of assuming narrowband sensitivity for a camera that has a relatively wide band. In those cases, we corrected the value of  $A$  in Eq. (3.30).

Table 3.5: Estimated and true chromaticities of illumination colors.

Input		Proposed (r,g) <sup>7</sup>	True (r,g)	Previous (r,g)	Error (Proposed) (CIE LAB)	Error (Previous) (CIE LAB)
Blue object	$e^1$	(1.20, 1.03)	(1.45, 1.07)	(1.13, 0.96)	4.84	5.97
	$e^2$	(0.43, 0.55)	(0.65, 0.60)	(0.41, 0.52)	7.70	9.07
Yellow object	$e^1$	(1.12, 0.99)	(1.45, 1.07)	(1.11, 0.99)	6.26	6.35
	$e^2$	(0.56, 0.65)	(0.65, 0.60)	(0.56, 0.65)	6.11	6.01
Green object	$e^1$	(0.95, 0.92)	(1.37, 1.02)	(0.24, 0.34)	8.54	48.99
	$e^2$	(0.39, 0.51)	(0.46, 0.44)	(0.10, 0.16)	8.56	44.61
Red object	$e^1$	(2.01, 1.30)	(1.37, 1.02)	(3.24, 1.51)	10.03	21.35
	$e^2$	(0.60, 0.69)	(0.46, 0.44)	(0.97, 0.92)	19.46	30.78

### Applying the method to outdoor scenes

We show the results of applying the proposed method to real images of natural outdoor scenes in Figures 3.32 and 3.34. Figure 3.32 (a) is the input image, (b) shows the input image chromaticities, (c) is the result of removing illumination colors from (a), and (d) shows image chromaticities of (c). While (b) has two chromaticities due to the presence of different illuminations, (d) has unified chromaticities since those illumination colors are removed.

Figure 3.33 shows details of our method's processes. Figure 3.33 (a) shows the pixels used for illumination color estimation. The blue pixels of (a) are chosen from shadowed region, and red pixels are chosen from non-shadowed region. Figure 3.33 (b) shows the classified pixels that belong to shadowed and non-shadowed regions, and (c) is the visualized  $F$  values of the input image in grayscale.

Another result is shown in Figure 3.34. Fig. 3.34 (a) is the input image, (b) shows its image chromaticity, (c) shows the result of color constancy, and (d) is the image

<sup>7</sup>b=1.0.

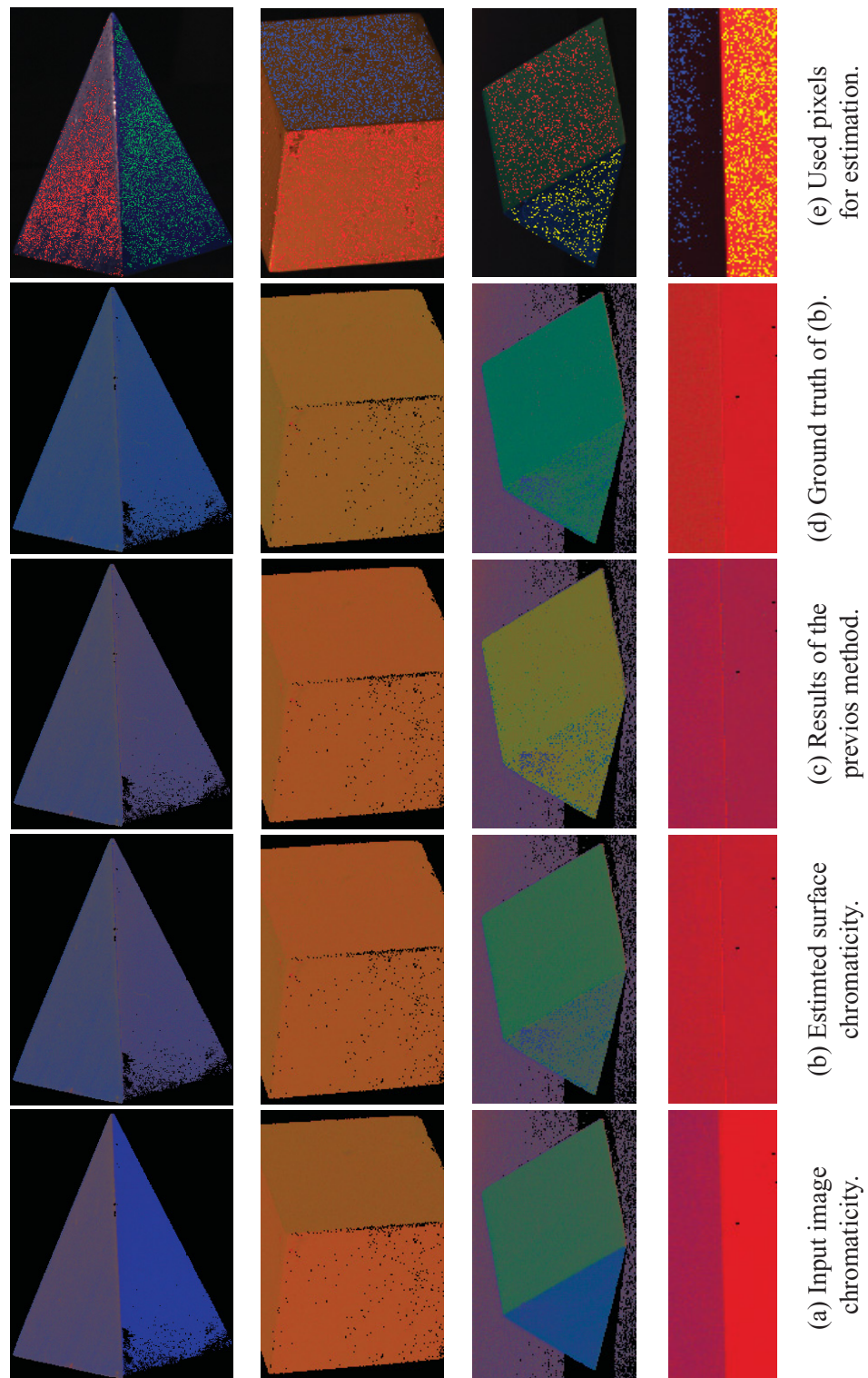


Figure 3.30: Experimental Results of four objects. (a) Input image chromaticities. (b) Estimated surface chromaticity by the proposed method. (c) Results of the previous method [FFB95]. (d) Ground truths of the top row. (e) Used pixels for our estimation.

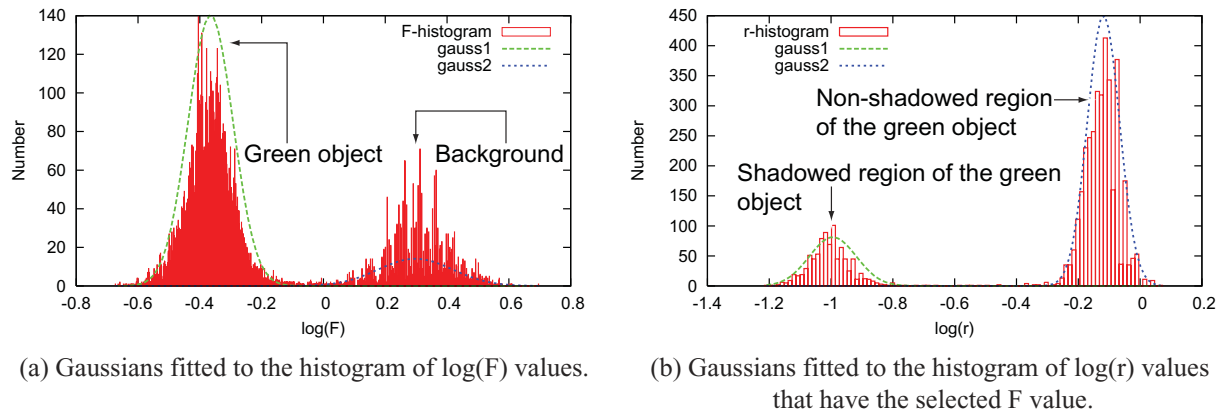


Figure 3.31: Results of fitting the Gaussian mixture model to the input image's distributions. The image used was Figure 3.30 (c). The left is the Gaussian fitted to the histogram of  $\log(F)$  values of the input image, and the right is that of  $\log(r)$  values that have the selected  $F$  value. The distributions fit the Gaussians well in  $\log(F)$  and  $\log(r)$  spaces, and therefore two colors from shadowed and non-shadowed regions can be extracted successfully.

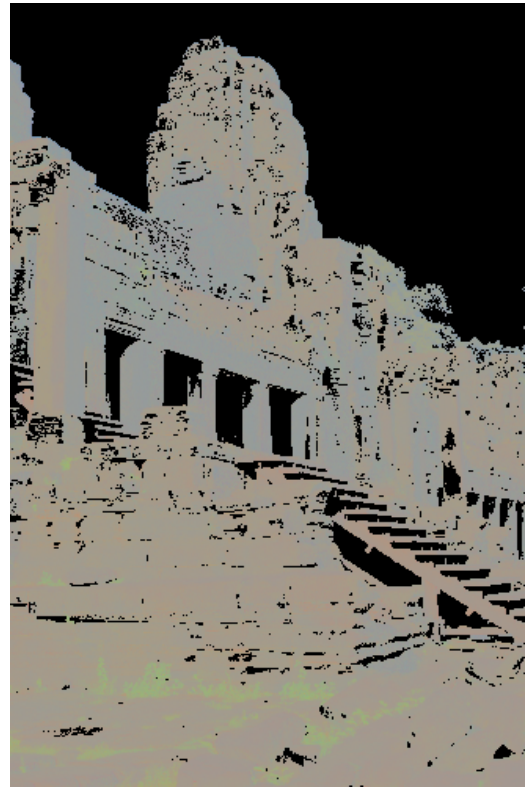
chromaticity of (c). The object's color becomes uniform in (c). Figure 3.35 (a) shows the selected pixels from shadowed and non-shadowed regions, (b) shows the classified pixels that belong to shadowed and non-shadowed regions, and (c) shows  $F$  values of Fig. 3.34 (a). Those results indicate the realizability of illumination color estimation for real images of natural outdoor scenes.

### 3.7 Summary

We have proposed a method to estimate surface and illumination chromaticities using an illumination change. Our main contribution is to develop a method that is robust and accurate even for outdoor objects, where conditions are less controllable compared with conditions for indoor objects. We analyzed the effect of input errors on the previous method, and found the two following facts: (1) Color difference between two input illuminations magnifies the input errors, and thus the estimation may produce large errors; (2) The usual daylight-color changes are less than preferable color difference regarding the usual input chromaticity channel's error. Based on those facts, we made the previous method more robust and accurate by considering the possible range of outdoor illumination colors, that is a specific line segment in a color space. Experi-



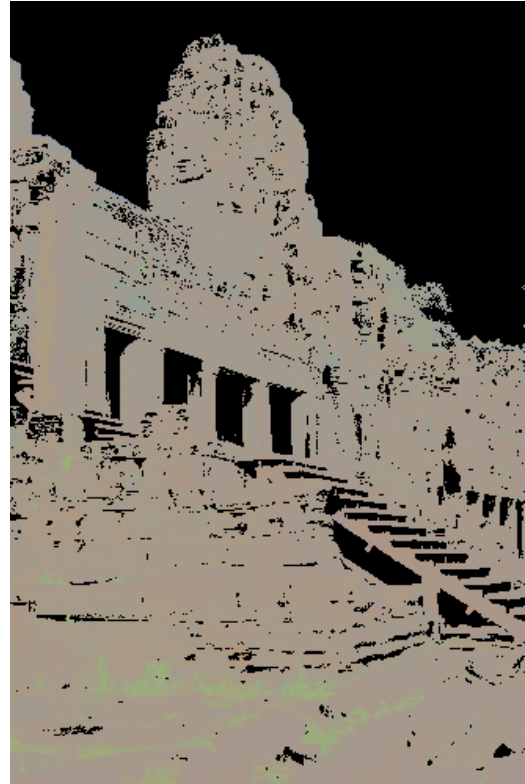
(a) Input image.



(b) Input image chromaticity.



(c) Estimated surface color of (a).

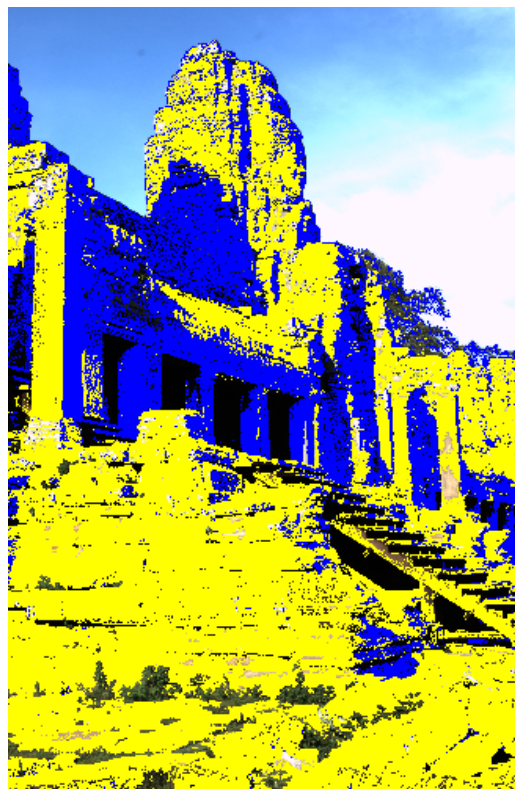


(d) Estimated surface chromaticity of (a).

Figure 3.32: An example of applying the proposed method to an outdoor image.



(a) Used pixels for illumination color estimation.



(b) Classified pixels for illumination color removal.



(c) Visualized  $F$  values of Fig. 3.32 (a).

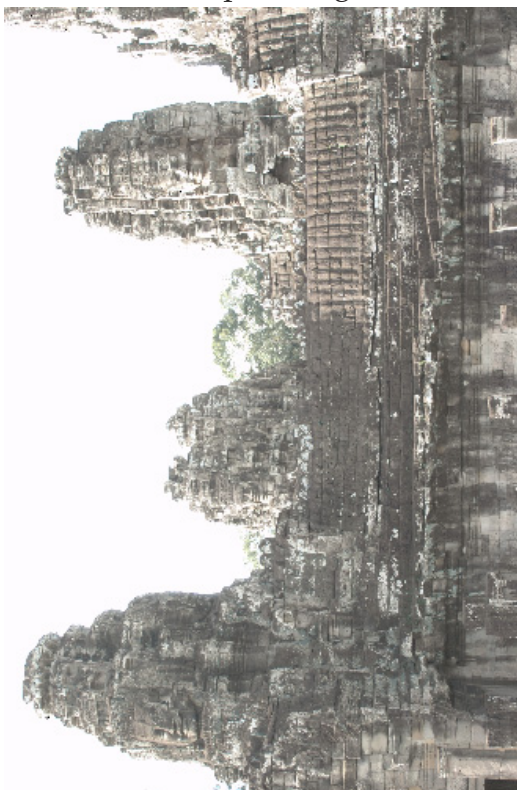
Figure 3.33: Details of our method's processes.



(a) Input image.



(b) Input image chromaticity.

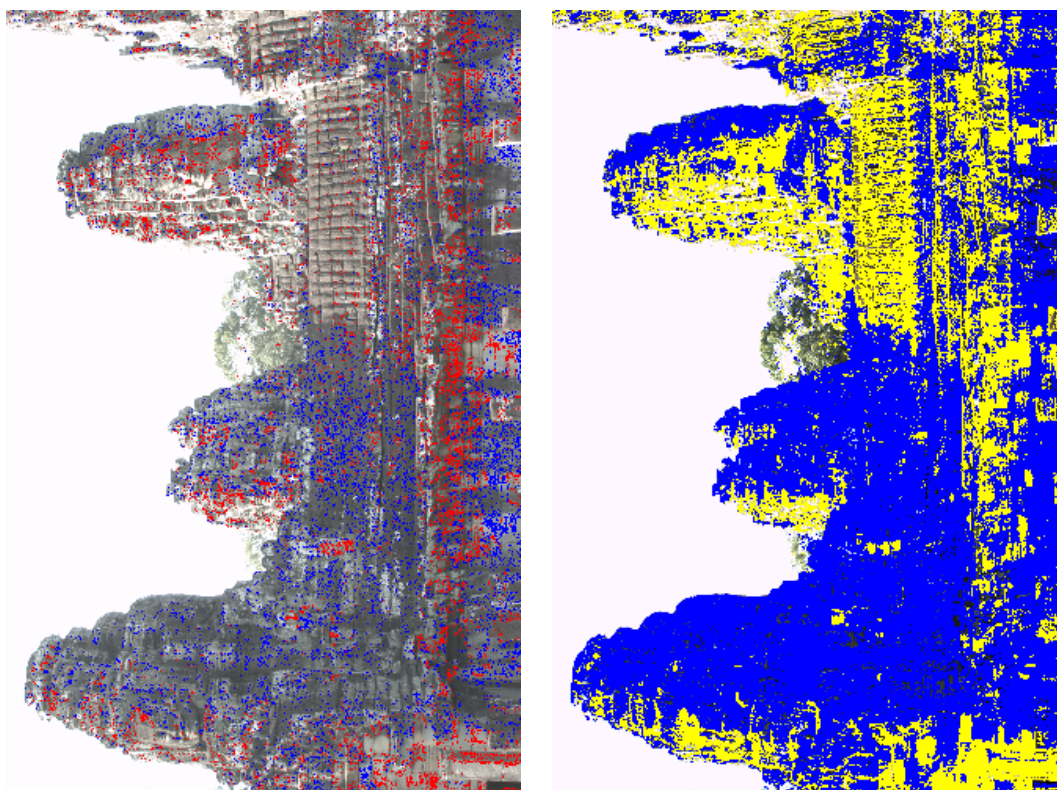


(c) Estimated surface color of (a).



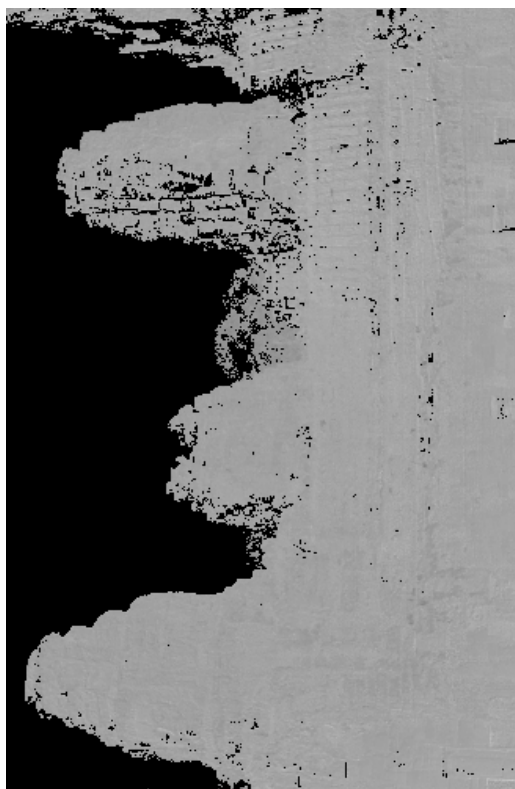
(d) Estimated surface chromaticity of (a).

Figure 3.34: Another example of applying the method to an outdoor image. Two chromaticities in (b) are unified in (d).



(a) Used pixels for illumination color estimation.

(b) Classified pixels for illumination color removal.



(c) Visualized  $F$  values of Fig. 3.34 (a).

Figure 3.35: Details of our method's processes.

mental evaluation has been done and it showed the effectiveness of our method. For accomplishing the estimation using a single image, we proposed a method utilizing the shadowed and non-shadowed region. The experimental results on an outdoor scene show the effectiveness of our method.

The remaining problem is the improvement of the accuracy of our estimation. We think that the method could be improved by using multiple surface colors, or using previously acquired information of a few surface colors. There are several problems for the estimation from a single image. The first is that the method assumes there are only two illumination colors included in an image. This is not the case when a curved surface is placed under two illuminants; the illumination colors would be blended on the surface. The second is that even if the  $F$  values are the same, the surface colors may not be identical if multiple surface colors are included in an image. We would like to extend the proposed method so that it can solve those problems.

## Chapter 4

# Estimating Surface Reflectance Using Spherical Images

This chapter proposes a new, efficient method to estimate reflectance parameters of diffuse outdoor objects from only one measurement with a spherical camera. The camera we used captures nearly 75 percent of a 360-degree field of view; thus, it captures the radiance of an object and illumination environment at one shot. By taking the known object's shape into account, the illumination effect is calculated and the surface reflectance is derived. Measurement and data-processing cost will be greatly decreased by this method compared to previous methods that need elaborate procedures. Neither specific apparatus nor calibration of the camera gain factor is needed. The shape of the object and the pose of the spherical camera are assumed to be known. We also assume that the target object only has diffuse reflection, and outdoor illumination is at infinity.

### 4.1 Introduction

Computer vision and graphics techniques to create a realistic model of a real world object have attracted interest from a wide range of research fields and industries in recent years. To simulate the accurate appearance of an object, we have to know the object's (1) shape and (2) surface reflectance properties. Acquiring shape information has been facilitated by the development of sensors and the progress of data processing algorithms, while acquiring surface reflectance properties remains a challenge, specifically

with outdoor objects.

This paper proposes a new, efficient method to estimate reflectance parameters of diffuse outdoor objects from only one measurement with a spherical camera. A spherical camera has nearly a 360-degree field of view; thus, it captures the radiance of an object and illumination environment at one shot. This enables us to capture both the object and illumination with an identical camera sensitivity, exactly at the same time, and in a geometrically consistent manner. By taking the known shape of the object into account, the illumination effect is calculated and the surface reflectance is derived. Measurement and data-processing cost will be greatly decreased by this method. Neither specific apparatus nor calibration of the camera gain factor is needed. However, the camera should cover a high dynamic range in order to measure both the intensity of the sun and the object. The shape of the object and the pose of the spherical camera are assumed to be known. We also assume that the target object only has diffuse reflection, and outdoor illumination is at infinity.

### 4.1.1 Related work

Acquiring surface reflectance properties has attracted a lot of attention in computer vision and computer graphics research fields. In the late 1990s, several modeling methods with range sensors were proposed [PCD\*97, NK99, LHS00, WKSS01, BMR01], however, those methods created surface textures by simply blending images taken from multiple views.

Meanwhile, physics-based reflectance estimation methods [DvGNK97, SWI97, LL99, MYT03], image-based rendering techniques [SOSI03, WMTG05], and techniques to measure the BRDF (Bidirectional Reflectance Distribution Function) [JC02] have been studied to create a more physically correct object appearance compared with those created in the early 1990s. Those methods have achieved highly accurate re-renderings, yet they were designed for an indoor environment where one can easily change lighting conditions [IOT\*07].

For calculating surface reflectance properties, one would need (1) the shape of a target object, (2) the actual appearance of the object, and (3) illumination environment. Shape information and actual appearance can be obtained by range and image sensors, respectively.

The illumination environment can be acquired in several ways. Yu et al., the first who handled outdoor objects to authors' knowledge, took photographs of the

sun and sky to measure their radiance distribution [YM98]. As they used a normal camera, they included landmarks in each photograph so that they could use them to recover the camera pose later. The position of the sun was calculated by the time and date, and the sky radiance was fitted to the CIE (International Commission on Illumination) standard model to extrapolate the missing portion of the sky. The color could have been calibrated by hand, since CIE standard model does not include spectral information. They first recovered diffuse reflectance from measured sky irradiance and from appearance, and then they acquired specular properties by fitting multiple photographs to the Lafortune model. Debevec et al., the second and the latest to tackle the outdoor problem, used a specific apparatus to measure the outside illumination [DTG\*04]. They used a mirrored sphere to image the sky and clouds, a shiny black sphere to indicate the position of the sun, and a diffuse grey sphere to indirectly measure the intensity of the sun. They decided the reflectance parameters of the previously obtained BRDF by an iterative calculation using the object's photographs from multiple views.

Methods to acquire a near light source environment have also been proposed. Sato et al. used omnidirectional stereo to recover illumination with geometric information [SSI99]. Takai et al. took an image of a pair of diffuse spheres, and used the difference between them to first estimate point light sources and then the remaining lighting environment [TNMM04]. The two methods successfully superimposed virtual objects into room scenes as well as exterior scenes by recovering illumination of the scenes.

To summarize those recent works, surface reflectance estimation needs a lot of elaborate procedures, such as calibration between absolute intensity and photometric device, calibration of the coordinates between geometric data, image sensors, and photometric device. With respect to large-scale objects set in outdoor, more practical methods are needed.

## 4.2 Scene Radiance Acquisition with a Spherical Camera

This paper proposes to use a spherical camera for acquiring the radiance distributions of the object and surrounding illumination. The benefit of it is that it captures the object and illumination with an identical camera sensitivity, exactly at the same time, and in a geometrically consistent manner. Using the same camera sensitivity for capturing the object and illumination, the algorithm becomes simple and no calibration of the camera gain factor is needed. It is always sure that the image intensity of the object reflects the



Figure 4.1: A camera Ladybug2 [Lad].

instantaneous response to the surrounding illumination that is captured in the same image. The camera pose calibration is required only once; the object and illumination are geometrically consistent in the acquired image.

A spherical camera used in this paper is Point Grey Research Ladybug2 [Lad]. Ladybug2 has 6 lenses, one of them and the others point to vertical and horizontal directions, as shown in Figure 4.1. We show an image taken by Ladybug2 in Figure 4.2. The image's vertical and horizontal axes correspond to the polar and zenith angles. The camera captures nearly 75 percent of a 360-degree field of view, so it captures the radiance distributions of the sky and the target object at a time.

The reflectance of the target object's surface can be estimated by using the image taken by Ladybug2. The incoming spectrum which is irradiated from surrounding illumination to the target object is calculated by integrating the incident radiance distribution of illumination from all the directions; we can calculate the irradiance of the target object's surface. By dividing the surface radiance by its irradiance, the surface reflectance can be obtained. Mathematical formulations of illumination and surface radiance are described in the following subsections.

### 4.2.1 Illumination radiance

As Figure 4.3 shows, the camera records the spherical radiance distribution of illumination at the camera center  $C$ . Let us denote the incident radiance distribution of illumination as  $L(\lambda, \theta, \phi)$ , where  $\lambda$  is the wavelength,  $\theta$  and  $\phi$  are the polar and zenith angles.

When recorded by a camera, the light will be multiplied by the camera sensitivity

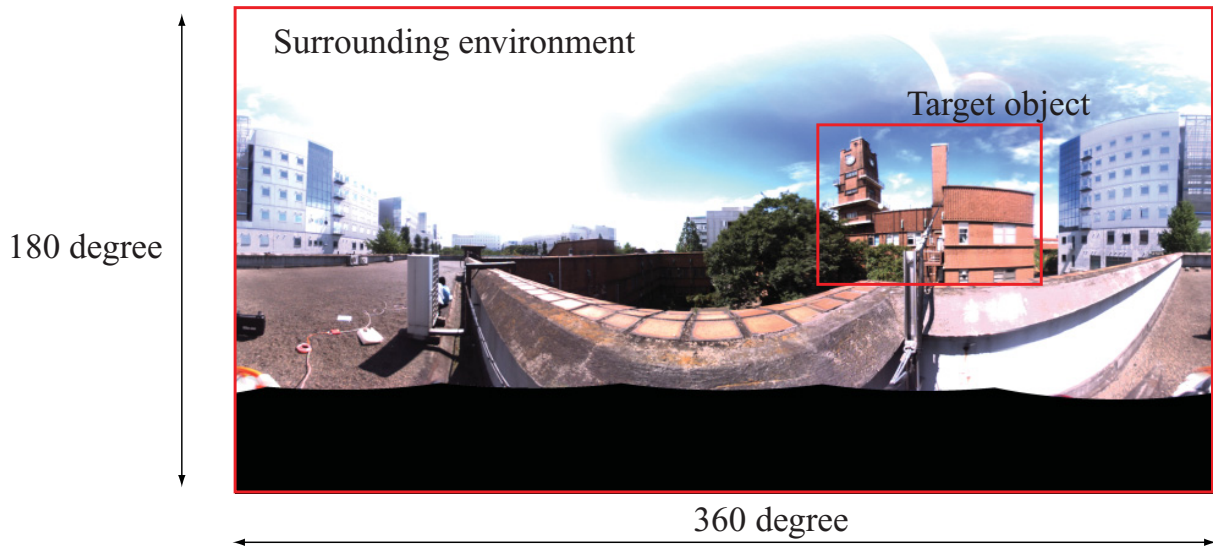


Figure 4.2: An image taken by Ladybug2.

function  $q_k(\lambda)$ , then integrated over the visible spectrum  $\Omega$ . Thus, image intensity  $I_k$  can be expressed as;

$$I_k(\theta, \phi) = \tau_k \int_{\Omega} L(\lambda, \theta, \phi) q_k(\lambda) d\lambda, \quad (4.1)$$

where  $k$  and  $\tau$  are the type of sensors and the camera gain determined by the aperture, the integration time, and the electronic amplification.

Assume that the camera sensitivity can be approximated by a Dirac's delta function (*narrow-band camera assumption*), the wavelength  $\lambda$  can be considered as a constant; the last equation can be rewritten as;

$$I_k(\theta, \phi) \simeq \tau_k L(\lambda_k, \theta, \phi) \quad k = \{r, g, b\}. \quad (4.2)$$

### 4.2.2 Surface radiance

The camera also records the radiance of the object's surface. Let us consider an infinitesimal solid angle  $d\omega_i$ . Seen from a point A,  $d\omega_i$  is constituted by a size  $d\theta_i$  in polar angle and  $d\phi_i$  in zenith angle as shown in Figure 4.4;

$$d\omega_i = \sin \theta_i d\theta_i d\phi_i. \quad (4.3)$$

Then, the light energy that the point A receives from the infinitesimal solid angle  $d\omega_i$  will be [SSI99];

$$L_i(\lambda, \theta_i, \phi_i) \cos \theta_i \sin \theta_i d\theta_i d\phi_i. \quad (4.4)$$

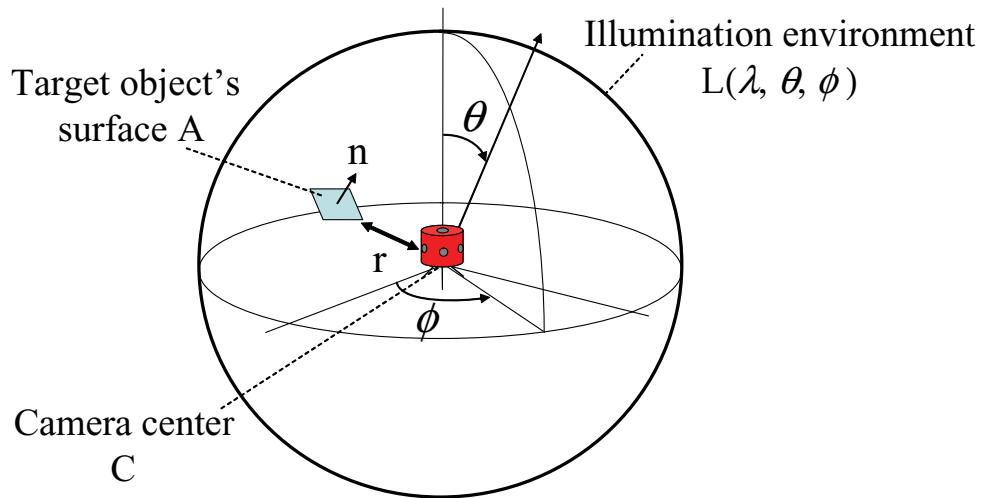


Figure 4.3: Illustration of our notations. The spherical camera at camera center  $C$  acquires radiance distribution of illumination environment  $L(\lambda, \theta, \phi)$  as well as the radiance of the surface  $A$ .  $\theta$  and  $\phi$  are the polar and azimuth angles.

The irradiance  $E$  at the point  $A$  is the integration of the incoming light energy over the hemisphere whose north pole is at the surface normal direction (Figure 4.4 (a));

$$E^A(\lambda) = \int_{-\pi}^{\pi} \int_0^{\frac{\pi}{2}} L_i(\lambda, \theta_i, \phi_i) \cos \theta_i \sin \theta_i d\theta_i d\phi_i. \quad (4.5)$$

Assume that the surface is a Lambertian surface. Then, the reflected light of the point  $A$  is uniform regardless of the viewing direction. Therefore, the radiance  $I$  of the point  $A$  can be simply written as the multiplication of irradiance  $E$  and the surface reflectance  $S$ ;

$$\begin{aligned} I^A(\lambda) &= \int_{-\pi}^{\pi} \int_0^{\frac{\pi}{2}} S^A(\lambda) L_i(\lambda, \theta_i, \phi_i) \cos \theta_i \sin \theta_i d\theta_i d\phi_i \\ &= S^A(\lambda) E^A(\lambda). \end{aligned} \quad (4.6)$$

When recorded by a camera, the radiance  $I^A(\lambda)$  will be filtered by the camera sensitivity function. By using the narrow-band camera assumption which is introduced before Eq.4.2, the wavelength  $\lambda$  becomes a constant. Hence, the image intensity  $I_k$  of the point  $A$  can be written as;

$$I_k^A = \tau_k S_k^A E_k^A \quad k = \{r, g, b\}. \quad (4.7)$$

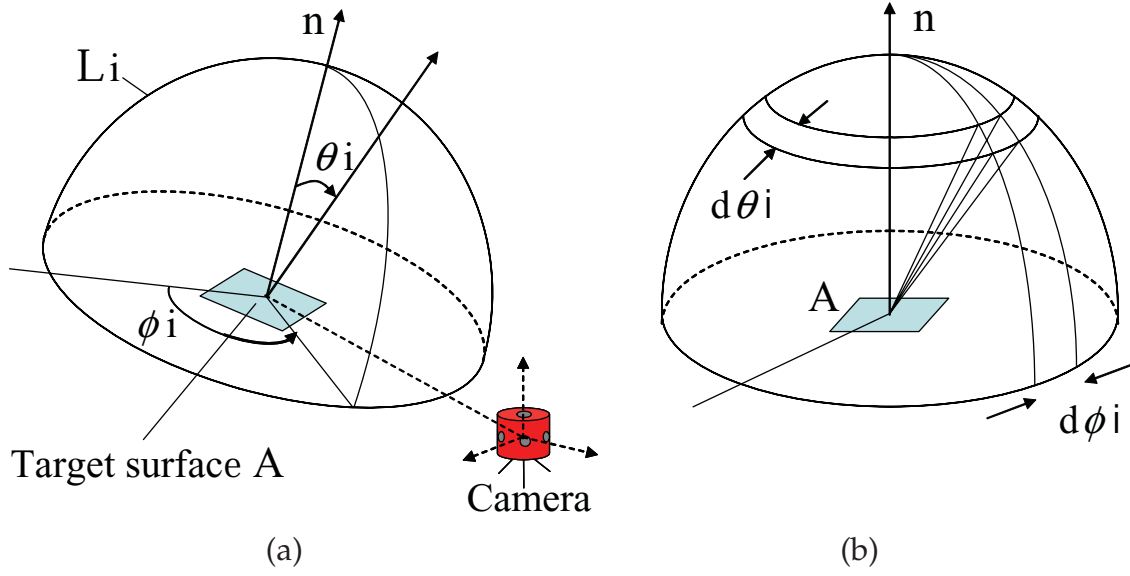


Figure 4.4: (a) The direction  $(\theta_i, \phi_i)$  of incident light rays to the surface  $A$ . (b) The solid angle at the direction  $(\theta_i, \phi_i)$ .

## 4.3 Reflectance Estimation from Scene Radiance and Object's Shape

### 4.3.1 Surface irradiance

Let us consider again the irradiance which the point  $A$  in Figure 4.3 receives. Owing to the assumption that the illumination is at infinity, the  $r$  in Figure 4.3, the distance between the camera and the point  $A$ , can be approximated as zero compared to the distance to the illumination. For this reason, surrounding illumination seen from the camera and the object surface is nearly equal;

$$L(\lambda, \theta, \phi) \simeq L_i(\lambda, \theta_i, \phi_i). \quad (4.8)$$

Then, the irradiance  $E$  at the point  $A$  (Eq. 4.5) can be rewritten using Eq. 4.8;

$$E^A(\lambda) = \int_{\Phi} \int_{\Theta} L(\lambda, \theta, \phi) \cos \psi \sin \theta d\theta d\phi \quad (4.9)$$

where  $\psi$  is the angle between the surface normal and the incoming light direction  $(\theta, \phi)$ . The new integral ranges  $\Theta$  and  $\Phi$  are introduced to reflect the change of the coordinate system.

By introducing the narrow-band camera assumption to Eq. 4.9,

$$\tau_k E_k^A = \tau_k \int_{\Phi} \int_{\Theta} L(\lambda_k, \theta, \phi) \cos \psi \sin \theta d\theta d\phi. \quad (4.10)$$

By substituting Eq. 4.2,

$$\tau_k E_k^A = \int_{\Phi} \int_{\Theta} I_k(\theta, \phi) \cos \psi \sin \theta d\theta d\phi. \quad (4.11)$$

The camera pose and the object shape are known, hence, we can calculate the value of  $\psi, \Theta, \Phi$ . Thus, we obtain the irradiance  $\tau_k E_k^A$  from the acquired illumination radiance  $I_k(\theta, \phi)$ .

### 4.3.2 Surface reflectance estimation

Surface reflectance can be obtained by dividing its radiance value by the irradiance value. We let the rendering software to calculate the irradiance of a surface point (Eq. 4.11). We let it render the object appearance seen from the camera position under the acquired illumination distribution  $I_k(\theta, \phi)$ , where the surface reflectance  $S_k^A$  was set to 1.0 for all sensors  $k$  and for all points  $A$ . We denote this image intensity as  $I_k^A$ . This could be considered as substituting 1.0 into  $S_k^A$  in Eq. 4.7. Therefore, the image intensity  $I_k^A$  can be expressed as;

$$I_k^A = \tau_k E_k^A. \quad (4.12)$$

The rendered image is the image of  $\tau_k E_k^A$ . By dividing the acquired image intensity  $I_k^A$  by the rendered image intensity  $I_k^A$ , (Eq. 4.7/Eq. 4.12), the surface reflectance  $S_k^A$  can be obtained.

$$S_k^A = I_k^A / I_k^A \quad (4.13)$$

## 4.4 Experiment

### 4.4.1 Measurement of the scene radiance

We used Point Grey Research Ladybug2, a spherical digital video camera. We captured the radiance distributions of the object and surrounding illumination by using Ladybug2.

To capture the wide level of intensity, we took images with ND filters and multiple shutter speeds. We used two ND filters, Fujifilm ND-4.0 and ND-3.0 that reduce

incoming light to  $1/10000$  and  $1/1000$ , respectively. Each filter was placed in front of the lenses, as Figure 4.5 shows. We also tuned the shutter speeds carefully to cover the entire dynamic range in conjunction with these filters, and took images, as Figure 4.6 shows.



Figure 4.5: Ladybug2 with an ND filter.

#### 4.4.2 Vignetting rectification

The ND filters attached in front of the lens produce vignette-like effect. Image brightness gradually reduces from the center towards the periphery of the image, as Figure 4.7 (a) shows. This is due to the reflection at the interface of the ND filter. Light that is reflected by the filter increases when its incident angle is off the optical axis.

To rectify the reduction of image brightness, we took images of a white board by Ladybug2 with and without the ND filter. In this experiment, images from each camera lens were output. Then, we modeled the effect by an empirical mathematical model, and calculated the parameter by the least square fitting. Figure 4.7 (b) shows the estimated vignetting effect. By dividing the images taken with ND filters by Figure 4.7 (b), rectified images can be acquired, as shown in Figure 4.7 (c).



Shutter speed : 1/39, with ND-4.0 filter



Shutter speed: 1/10000



Shutter speed : 1/19, with ND-4.0 filter



Shutter speed: 1/2500



Shutter speed : 1/9, with ND-4.0 filter



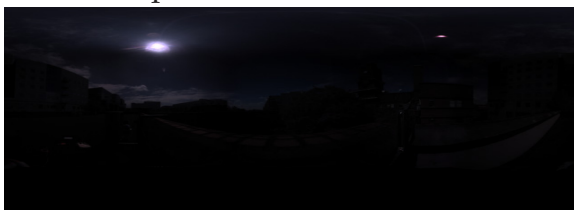
Shutter speed: 1/1250



Shutter speed : 1/5, with ND-4.0 filter



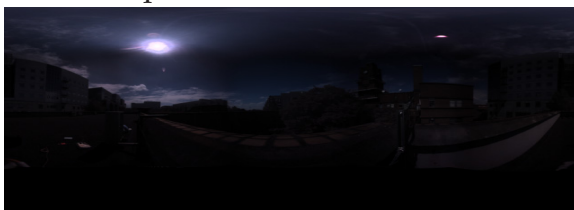
Shutter speed: 1/625



Shutter speed : 1/39, with ND-3.0 filter



Shutter speed: 1/312



Shutter speed : 1/19, with ND-3.0 filter

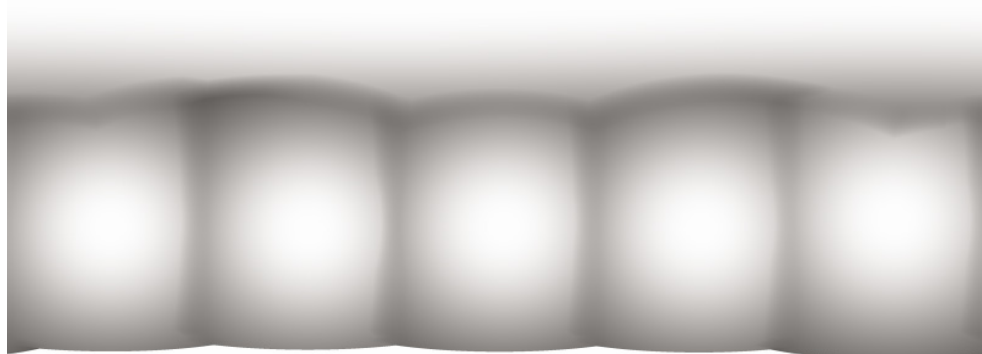


Shutter speed: 1/156

Figure 4.6: A set of images taken on a sunny day. The unit of shutter speeds is micro second. Normally, about twenty and ten images were taken on sunny and cloudy days, respectively.



(a)



(b)



(c)

Figure 4.7: (a) an image with vignette-like effect. See the upper right of the image. The reduction of image is highly visible. (b) the estimated vignette-like effect. (c) an image rectified. Image brightness is recovered.

### 4.4.3 Generating an HDR image

We generated an HDR (High Dynamic Range) image. At this point, we eliminated pixels which had values of brightness less than 10 or more than 210, because those pixels could be under camera dark or saturated. We also revised some pixels seemed to make lens flare in images taken.

Images taken with an ND filter were colorized by the filter. To rectify it, we took two images by Ladybug2 with and without the ND filter. By comparing these two images, we calculated the color scaling factors. Images with an ND filter were corrected with these parameters.

### 4.4.4 Measurement of the object's shape

We measured the shape of a diffuse outdoor object using a Cyrax 2500 [Cyr], a range sensor. We chose a planar convex object to avoid interreflection. The shape of surrounding environment was included to make the calibration easier. We could also get more real radiance distributions of surrounding illumination by taking the shape of surrounding environment into account.

We calibrated the object and the camera coordinates using Tsai's method [Tsa86]. We found corresponding points between the shape of the object and the images taken, then we calculated the view point and the projection matrix using those coordinate pairs.

### 4.4.5 Estimation of the surface reflectance

We rendered the object's shape, of which the surface reflectance was set to be 1.0, under the lighting environment captured by the Ladybug2. The view point was set to the estimated camera position. We used the rendering system software RADIANCE [Rad].

We generated the surface reflectance image by dividing the original HDR image by the rendered object image, where its surface reflectance was set to be white;  $S_k = 1.0$ , for all  $k$ .

### 4.4.6 Evaluation

We conducted the experiment three times, with different times and days. Figures 4.9 (a), 4.9 (b) and 4.9 (c) are the captured radiance images. They were taken at

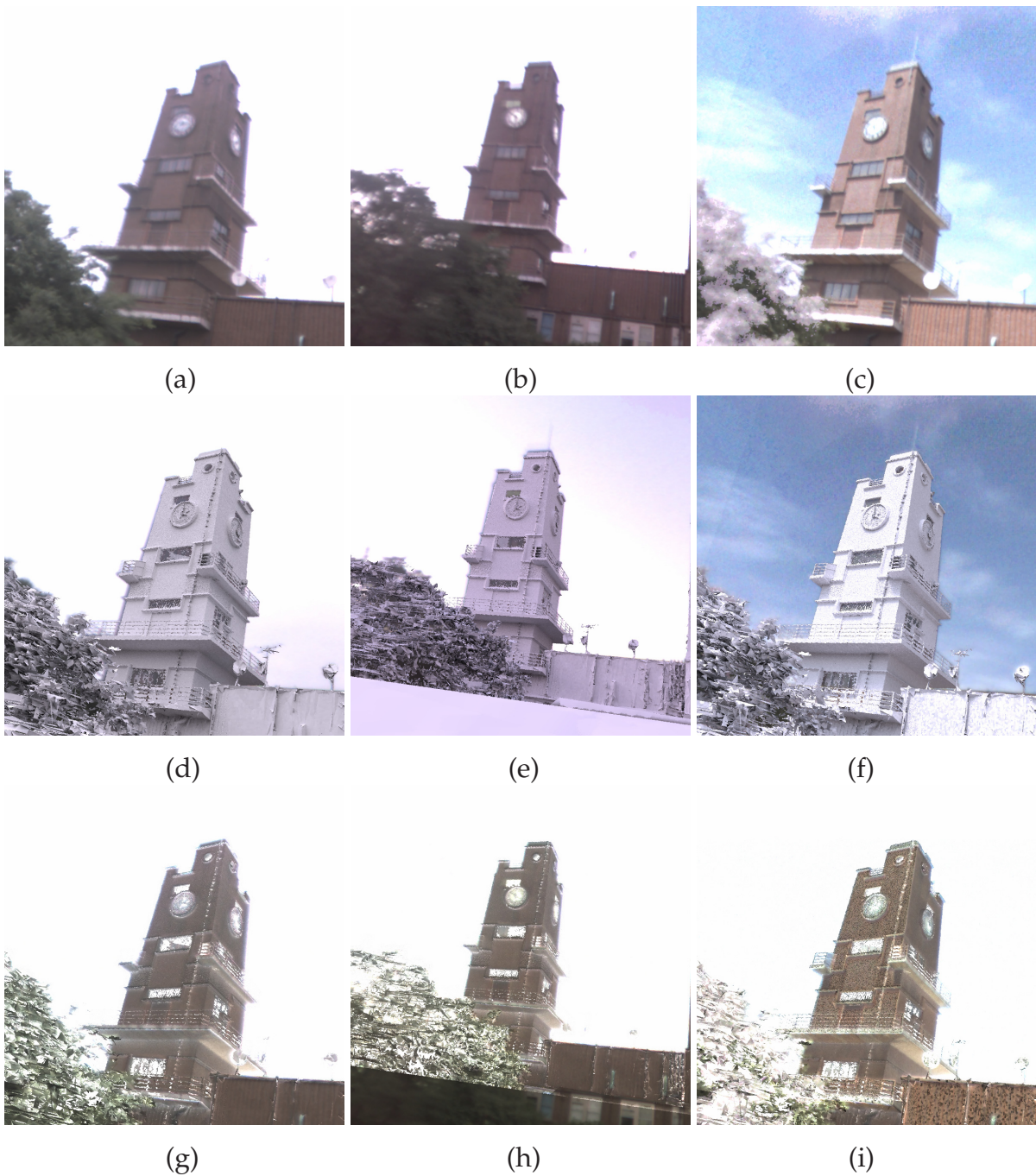


Figure 4.8: The captured images at (a) 14:35, illuminated by cloudy daylight, (b) 17:52, illuminated by twilight, (c) 11:50, illuminated by sunny daylight, are shown. The rendered images of the object's shape, (d) on cloudy day, (e) at dusk, and (f) on a sunny day, are shown in the middle row. Images in the bottom row are the estimated surface reflectance. (g) was derived from the images (a) and (d), (h) was from the images (b) and (e), and (i) was from (c) and (f).

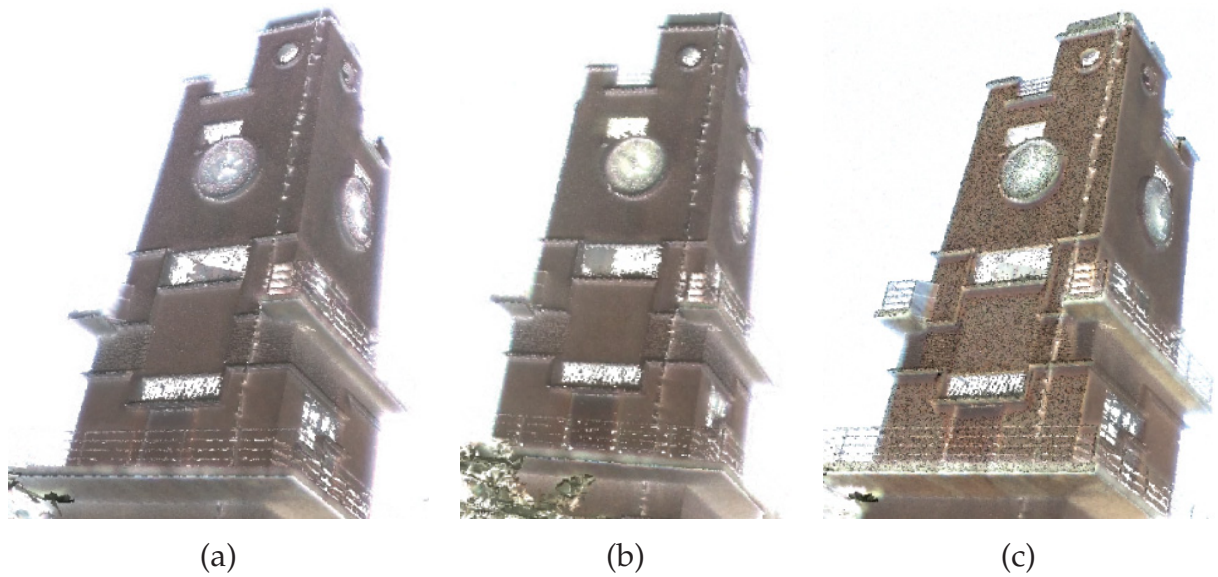


Figure 4.9: Zoomed images of estimated surface reflectance, shown in Fig. (g), (h) and (i).

14:35, illuminated by cloudy daylight, at 17:52, illuminated by twilight, and at 11:50, illuminated by sunny daylight, respectively. Figures 4.9 (d), 4.9 (e) and 4.9 (f) are the rendered images of the object's shape, of which the surface reflectance was set to be 1.0, under the cloudy light, twilight and daylight, respectively. Figures 4.9 (g), 4.9 (h) and 4.9 (i) are the estimated images of surface reflectance, derived from (a) and (d), (b) and (e), and (c) and (f), respectively.

Nevertheless there is much difference between the images (a), (b) and (c), the three estimated surface images, (g), (h) and (i), look similar to each other. The median RGB values of the part of the tower were (120, 108, 105) in (g), (120, 107, 98) in (h), and (141, 127, 111) in (i). The intensity is slightly different, whereas the chromaticity, (0.360, 0.324, 0.315) in (g), (0.369, 0.329, 0.302) in (h), and (0.372, 0.335, 0.292) in (i) are surprisingly similar. This indicates that the narrowband assumption is valid with the object used in the experiment.

## 4.5 Discussion

The appearance of one side of the clock tower is quite different from that of the other side in Figure 4.9 (i). One of the reasons for this difference is that we could not generate an accurate HDR image from images taken on the sunny day. This is partly because the

sky was so bright, that some portion of the sky could not be captured correctly. Then, an inaccurate HDR image, as shown in Figure 4.10, was generated. We did not need to use ND filters on the cloudy day and at dusk.

We see there is much noise in the brighter side of the clock tower in Figure 4.9 (i). The uneven and rough surface of the object causes this noise. When bright light illuminates an uneven and rough plane, some surface patches on the plane are illuminated by direct light and others are not. Therefore, the difference between the appearance of the bright patches and that of the dark patches becomes remarkable, and they are seen as noise.

Normally, we have to take interreflection into account. In this paper, we assumed that all the objects in the surrounding environment were white. Thus, the interreflection of white surfaces was calculated in the experiments. However, the interreflection between the ground and the surface of the building, or between the two surfaces of the building, is slightly different from what we have calculated, since their true colors are different from white. Estimated surface reflectance parameters may become lower than correct parameters, since the interreflection between white surfaces is brighter than that between colored surfaces.



Figure 4.10: An inaccurate HDR image.

In the future, we should acquire more accurate scene radiance by generating more accurate HDR image. To do so, we can possibly design a new camera which consists of several fish-eye lenses. Cameras with higher performance such as high-end digital

cameras have several advantages. Not only do they have higher resolution, they have a wide range of exposure times and apertures, and the flare, vignetting and distortion effects are minimized in those lenses.

The more precise shape of the target object could improve the quality of estimated surface albedos. Those could be achieved by using the principal component analysis to estimate accurate normals from the surrounding surface patches.

The diffuse interreflection is one of the significant problems in the proposed method. The problem seems to be ill-posed, but it could be possibly solved by using some assumptions or constraints, such as a uniform surface reflectance or a partially uniform surface reflectance.

## 4.6 Summary

We have proposed a new, efficient method to estimate reflectance parameters of diffuse outdoor objects from only one measurement with a spherical camera, since the radiance distributions of the object and surrounding illumination can be captured at one shot. Surface reflectance can be calculated from the measured surface radiance and calculated surface irradiance from the measured illumination radiance. The measurement and data-processing cost are greatly decreased by this method compared to previous methods that need elaborate procedures.

One of the challenging tasks of the method is how to acquire such a high-dynamic range, since the measurement must cover the range of both the radiance of the object and the illumination. Due to the limitation of shutter speeds of the device, neutral density filters have to be used. Attaching the filters in front of the lens causes a vignette-like effect because of the reflection at the interface of the filter. However, by modeling the effect with an empirical model, the original image intensity can be recovered.

Images taken under three different illumination conditions provided similar estimations of surface reflectance, in terms of both intensity and chromaticity. This encourages us to believe that the method can be applied to many outdoor objects with diffuse reflection. The method tends to provide results with undesirable effect on images taken on a sunny day. This is due to the limitation of the sensor device, and future work should be to combine cameras that have higher performance to produce better results. Development of a method that can handle specular surfaces and can take the diffuse interreflection into account would be a difficult but challenging work.

# Chapter 5

## Conclusions

### 5.1 Summary

The goal of this paper is to provide basic techniques for estimating surface properties of a large-scale object such as an architectural structure in an outdoor environment. Measuring surface reflectance properties of such a huge object becomes a challenge. Under the assumption that the appearance of an object can be modeled by mapping the image texture to the known shape of the object, we have proposed methods to arrive at consistent colors by using color constancy techniques and reflectance estimation techniques. Two methods were proposed for color constancy: a method that directly uses the physical model of illumination color, and a method that performs more robust estimation for a practical use. Both methods use illumination change as a constraint, so that they can perform a pixel-based operation. For the purpose of estimating surface reflectance, an efficient method that uses spherical images has been proposed.

#### 5.1.1 Estimating surface chromaticity from Blackbody illumination

We proposed a method to solve color constancy problem by exploiting blackbody radiation. Our method performed considerably well in the experiments with simulation data, while it produced significant errors with real outdoor illumination data. We specified that the allowable error in the system should be lower than 0.1%. Most illuminants have larger than 0.1% difference from blackbody radiation, and this resulted in the errors.

The discussion about the robustness of our method and the possibility of solving color constancy from an illumination change shows that much information such as assumptions on reflectances should be taken into account with the constraint on illumination to achieve stable and accurate color constancy.

### **5.1.2 Robust framework to estimate surface chromaticity from illumination changes**

We have proposed a method to estimate surface and illumination chromaticities using a single image. Our main contribution is to develop a method that is robust and accurate even for outdoor objects, where conditions are less controllable compared with conditions for indoor objects.

We have examined the effect of input errors on the previous method, and found the two following facts: (1) Color difference between two input illuminations magnifies the input errors, and thus the estimation may produce large errors; (2) With regards to the usual color difference between two daylights, it is difficult to perform a robust estimation, when a normal input chromaticity error exists. Based on those facts, we made the previous method more robust and accurate by considering the possible range of outdoor illumination colors, that is, a specific line segment in a color space. Experimental evaluation has been done and it showed the effectiveness of our method. For accomplishing the estimation using a single image, we proposed a method utilizing the shadowed and non-shadowed regions. The experimental results on an outdoor scene show the effectiveness of our method.

### **5.1.3 Estimating surface reflectance using spherical images**

We have proposed a new, efficient method to estimate reflectance parameters of diffuse outdoor objects from only one measurement with a spherical camera, since it captures the radiance distributions of both the object and surrounding illumination. Surface reflectance is derived by dividing the surface radiance by its irradiance calculated from the measured illumination radiance.

Several practical techniques to acquire such a high-dynamic range that includes both sunlight and light from dark diffuse surfaces have also been presented. We have succeeded in deriving similar reflectance images from images taken in different illumination conditions, and this shows the effectiveness of the method.

## 5.2 Contributions

In this thesis, we have proposed three methods that estimates surface properties of an object. Those are developed to provide fundamental techniques for estimating the surface properties of a large-scale object such as an architectural structure in an outdoor environment. The main contributions are summarized as follows:

1. *Insights into the stability and practicality of pixel-based color constancy.*

We introduced a method that assumes blackbody radiation as illumination colors. This enabled us to investigate the stability and practicality of the pixel-based color constancy problem theoretically.

2. *Development of a method that performs surface color estimation from two pixel values.*

Though numerous methods have previously been proposed, none of them can perform a pixel-based operation other than the methods [FFB95, FH01] proposed by Finlayson et al., and the method [MO00] proposed by Marchant et al. In fact, the methods<sup>8</sup> [FH01, MO00] are not for color constancy but for calculating the illumination invariant values. Therefore, our method is one of the two methods that perform pixel-based surface color estimation presently; the other is the method proposed by Finlayson et al. [FFB95], to which we have compared our method and shown that our method is an improvement.

3. *Development of an efficient method that estimates surface reflectance of large-scale objects in an outdoor environment.*

The advantage of the method is that neither specific apparatus nor calibration of exposure times, apertures, and camera gain factors is needed. Furthermore, geometric calibration between an image and shape information tends to be robust owing to the characteristic of a spherical camera. Measurement and data-processing cost will be decreased by the method compared to previous methods [YM98, DTG\*04]. This is critical specifically for large-scale objects.

## 5.3 Future Directions

This thesis has shown basic techniques for acquiring the surface properties of a large-scale object in an outdoor environment. While significant progress has been made,

<sup>8</sup>They independently proposed methods that do the same processing.

there remain some important issues to be explored to develop a system that models the object's appearance in reality.

### **5.3.1 Applying surface color estimation for plausible texture generation**

We have shown the problem that happens when images taken at different times are used directly for textures (Figure 1.2.) The color of the textures mapped on a model varies according to the illumination at the time the texture is captured. Our surface color estimation method is proposed with this problem as a starting point, and could be applied to solve the problem.

### **5.3.2 Surface color estimation using photo-sharing site**

Owing to the development of network infrastructures, we are able to collect many pictures from photo-sharing sites. Since our method can estimate surface colors more accurately with a large number of images, a use of a photo-sharing site would be an interesting future work. At this point, the variation of camera sensitivities would be one of the challenging tasks to solve.

### **5.3.3 Shadow extraction**

The proposed method succeeds in extracting colors from shadowed and non-shadowed regions. By utilizing the idea, a shadow extraction from an image could be possible. At this point, we would have to consider how to distinguish colors that have the same invariant. A method for extending the current method so that it can handle images with plenty of colors would be an interesting future work.

### **5.3.4 Development of high-performance spherical camera**

A new spherical camera with higher performance would improve the visual effects of the current results. Cameras with higher performance such as high-end digital cameras have higher resolution and a wide range of exposure times and apertures. Furthermore, the flare, vignetting, and distortion effects are minimized in those lenses. Designing a new spherical camera would provide improvement of the current system.

### **5.3.5 Surface reflectance estimation of specular objects**

We could extend the current reflectance estimation method so that it can handle specular objects. For this purpose, we may have to take images from multiple views. The diffuse interreflection must be also taken into account. The problem seems to be ill-posed, but it could possibly be solved by using some assumptions or constraints, such as a uniform surface reflectance or a partially uniform surface reflectance.

### **5.3.6 Illumination recovery from partially acquired albedo**

It may be a good idea to use the estimated albedo from spherical images to estimate albedos in different images. This would be a problem of recovering an unknown illumination with a partially acquired albedo. The technique would be practical and useful specifically for large-scale objects.



## References

- [Aut] AUTODESK, 3DS MAX: <http://usa.autodesk.com>.
- [BCF01] BARNARD K., CIUREA F., FUNT B.: Sensor sharpening for computational color constancy. *Journal of Optics Society of America A*. Vol. 18, No. 11 (2001), pp. 2728–2743.
- [BF97] BRAINARD D. H., FREEMAN W. T.: Bayesian color constancy. *Journal of Optics Society of America A*. Vol. 14, No. 7 (1997), pp. 1393–1411.
- [BFF97] BARNARD K., FINLAYSON G., FUNT B.: Color constancy for scenes with varying illumination. *Computer Vision and Image Understanding* Vol. 65, No. 2 (1997), pp. 311–321.
- [BJ01] BASRI R., JACOBS D.: Photometric stereo with general unknown lighting. In *Proceedings of 2001 IEEE Computer Society Conference on Computer Vision and Pattern Recognition (CVPR'01)* (2001), pp. pp. 374–381.
- [BMR01] BERNARDINI F., MARTIN I. M., RUSHMEIER H.: High-quality texture reconstruction from multiple scans. *IEEE Transactions on Visualization and Computer Graphics* Vol. 7, No. 4 (2001), pp. 318–332.
- [Buc80] BUCHSBAUM G.: A spatial processor model for object colour perception. *Journal of the Franklin Institute* Vol. 310, No. 1 (1980), pp. 1–26.
- [CF03] CIUREA F., FUNT B.: A large image database for color constancy research. In *Proceedings of the Eleventh Color Imaging Conference, Scottsdale* (November 2003), pp. pp. 160–164.
- [CGS06] CHEN T., GOESELE M., SEIDEL H.-P.: Mesostructure from specularities. In *Proceedings of 2006 IEEE Computer Society Conference on Computer Vision and Pattern Recognition (CVPR'06)* (2006), vol. Vol. 2, pp. pp. 1825–1832.

- [CH04] CHANDRA K., HEALEY G.: Estimating visible through near-infrared spectral reflectance from a sensor radiance spectrum. *Journal of Optics Society of America A*. Vol. 21, No. 10 (2004), pp. 1825–1833.
- [CH07] CHANDRA K., HEALEY G.: Reflectance recovery for airborne sensor images of 3d scenes. *Journal of Optics Society of America A*. Vol. 24, No. 4 (2007), pp. 957–966.
- [CT81] COOK R., TORRANCE K.: A reflectance model for computer graphics. *ACM Transactions on Graphics (Proceedings of ACM SIGGRAPH 1981)* (1981), pp. 506–512.
- [Cyr] CYRAX 2500, LEICA GEOSYSTEMS: <http://www.leica-geosystems.com>.
- [DA89] DHOND U. R., AGGARWAL J. K.: Structure from stereo—a review. *IEEE Transactions on Systems, Man and Cybernetics* Vol. 19, No. 6 (1989), pp. 1489–1510.
- [DF07] DREW M. S., FINLAYSON G. D.: Analytic solution for separating spectra into illumination and surface reflectance components. *Journal of Optics Society of America A*. Vol. 24, No. 2 (2007), pp. 294–303.
- [Dix78] DIXON E. R.: Spectral distribution of australian daylight. *Journal of Optics Society of America* Vol. 68, No. 4 (1978), pp. 437–450.
- [DL86] D’ZMURA M., LENNIE P.: Mechanism of color constancy. *Journal of Optics Society of America A*. Vol. 3, No. 10 (1986), pp. 1162–1672.
- [DM76] D. MARR T. P.: Cooperative computation of stereo disparity. *Science* Vol. 194 (1976), pp. 283–287.
- [DTG\*04] DEBEVEC P., TCHOU C., GARDNER A., HAWKINS T., POUILLIS C., STUMPFEL J., JONES A., YUN N., EINARSSON P., LUNDGREN T., FAJARDO M., MARTINEZ P.: Estimating surface reflectance properties of a complex scene under captured natural illumination. *USC ICT Technical Report ICT-TR-06* (2004).
- [DvGNK97] DANA K. J., VAN GINEKKE B., NAYER S. K., KOENDERINK J. J.: Reflectance and texture of real-world surfaces. In *Proceedings of 1997 IEEE Computer Society Conference on Computer Vision and Pattern Recognition (CVPR’97)* (1997), pp. pp. 151–157.

- [DW80] DEVICH R. N., WEINHAUS F. M.: Image perspective transformations. *Image processing for missile guidance; Proceedings of the Seminar, Society of Photo-Optical Instrumentation Engineers (SPIE)* (1980), pp. 322–332.
- [D'Z92] D'ZMURA M.: Color constancy: surface color from changing illumination. *Journal of Optics Society of America A. Vol. 9, No. 3* (1992), pp. 490–493.
- [FDF94] FINLAYSON G. D., DREW M. S., FUNT B. V.: Spectral sharpening sensor transformations for improved color constancy. *Journal of Optics Society of America A. Vol. 11, No. 10* (1994), pp. 1162–1672.
- [FF94] FINLAYSON G. D., FUNT B. V.: Color constancy using shadows. *Perception Vol. 23* (1994), pp. 89–90.
- [FFB95] FINLAYSON G. D., FUNT B. V., BARNARD K.: Color constancy under varying illumination. In *Proceedings of the IEEE International Conference on Computer Vision* (1995), pp. pp. 720–725.
- [FH01] FINLAYSON G. D., HORDLEY S. D.: Color constancy at a pixel. *Journal of Optics Society of America A. Vol. 18, No. 2* (2001), pp. 253–264.
- [FHH01] FINLAYSON G. D., HORDLEY S. D., HUBEL P.: Color by correlation: a simple, unifying, framework for color constancy. *IEEE Transactions on Pattern Analysis and Machine Intelligence Vol. 23, No. 11* (2001), pp. 1209–1221.
- [FHLD06] FINLAYSON G. D., HORDLEY S. D., LU C., DREW M.: On the removal of shadows from images. *IEEE Transactions on Pattern Analysis and Machine Intelligence Vol. 28, No. 1* (2006), pp. 59–68.
- [FHM05] FINLAYSON G. D., HORDLEY S. D., MOROVIC P.: Colour constancy using the chromagenic constraint. In *Proceedings of 2005 IEEE Computer Society Conference on Computer Vision and Pattern Recognition (CVPR'05)* (2005), pp. pp. 1079–1086.
- [FHT06] FINLAYSON G. D., HORDLEY S. D., TASTL I.: Gamut constrained illuminant estimation. *International Journal of Computer Vision Vol. 67, No. 1* (2006), pp. 93–109.
- [Fin96] FINLAYSON G. D.: Color in perspective. *IEEE Transactions on Pattern Analysis and Machine Intelligence Vol. 18, No. 10* (1996), pp. 1034–1038.

- [For90] FORSYTH D. A.: A novel algorithm for color constancy. *International Journal of Computer Vision* Vol. 5, No. 1 (1990), pp. 5–36.
- [FS01] FINLAYSON G. D., SCHAEFER G.: Solving for color constancy using a constrained dichromatic reflection model. *International Journal of Computer Vision* Vol. 42, No. 3 (2001), pp. 127–144.
- [FT04] FINLAYSON G., TREZZI E.: Shades of gray and colour constancy. In *Proceedings of the Twelfth Color Imaging Conference* (2004), IS & T - The Society for Imaging Science and Technology, pp. pp. 37–41.
- [GBSG02] GEUSEBROEK J. M., BOOMGAARD R., SMEULDERS A., GEVERS T.: A physical basis for color constancy. In *Proceedings of the First European Conference on Colour in Graphics, Image and Vision* (2002), pp. pp. 3–6.
- [GBSG03] GEUSEBROEK J. M., BOOMGAARD R., SMEULDERS A., GEVERS T.: Color constancy from physical principles. *Pattern Recognition Letters* Vol. 24, No. 11 (2003), pp. 1653–1662.
- [GCHS05] GOLDMAN D. B., CURLESS B., HERTZMANN A., SEITZ S. M.: Shape and spatially-varying brdfs from photometric stereo. In *Proceedings of IEEE International Conference on Computer Vision (ICCV '05)* (2005), pp. pp. 341–348.
- [GG07] GIJSENIJ A., GEVERS T.: Color constancy using natural image statistics. In *Proceedings of 2007 IEEE Computer Society Conference on Computer Vision and Pattern Recognition (CVPR'07)* (2007), pp. pp. 1–8.
- [GGSC96] GORTLER S., GRZESZCZUK R., SZELISKI R., COHEN M.: The lumigraph. In *ACM Transactions on Graphics (Proceedings of ACM SIGGRAPH 1996)* (1996), pp. pp. 43–54.
- [Gooa] GOOGLE EARTH: <http://earth.google.com>.
- [Goob] GOOGLE SKETCHUP: <http://sketchup.google.com>.
- [HARN01] HERNANDEZ-ANDRES J., ROMERO J., NIEVES J. L.: Color and spectral analysis of daylight in southern europe. *Journal of Optics Society of America A*. Vol. 18, No. 6 (2001), pp. 1325–1335.

- [Hec86] HECKBERT P. S.: Survey of texture mapping. *IEEE Computer Graphics and Applications Vol. 6*, No. 11 (November 1986), pp. 56–67.
- [Hor86] HORN B. K. P.: *Robot Vision*. New York: McGraw-Hill, 1986.
- [Hor06] HORDLEY S.: Scene illuminant estimation: past, present, and future. *Color Research and Application Vol. 31*, No. 4 (2006), pp. 303–314.
- [HS05] HERTZMANN A., SEITZ S. M.: Example-based photometric stereo: Shape reconstruction with general, varying brdfs. *IEEE Transactions on Pattern Analysis and Machine Intelligence Vol. 27*, No. 8 (2005), pp. 1254–1264.
- [Ike81] IKEUCHI K.: Determining surface orientations of specular surfaces by using the photometric stereo method. *IEEE Transactions on Pattern Analysis and Machine Intelligence Vol. 3*, No. 6 (1981), pp. 661–669.
- [IOT\*07] IKEUCHI K., OISHI T., TAKAMATSU J., SAGAWA R., NAKAZAWA A., KURAZUME R., NISHINO K., KAMAKURA M., OKAMOTO Y.: The great buddha project: Digitally archiving, restoring, and analyzing cultural heritage objects. *International Journal of Computer Vision Vol. 75*, No. 1 (2007), pp. 189–208.
- [JC02] JENSEN H. W., CHRISTENSEN N. J.: *Realistic image synthesis using photon mapping*. A K Peters, Ltd., 2002.
- [JMW64] JUDD D. B., MACADAM D. L., WYSZECKY G.: Spectral distribution of typical daylight as a function of correlated color temperature. *Journal of Optics Society of America Vol. 54*, No. 8 (1964), pp. 1031–1040.
- [Jud33] JUDD D. B.: Sensibility to color-temperature change as a function of temperature. *Journal of Optics Society of America Vol. 23* (1933), pp. 127–134.
- [KBK01] KOUDELKA M. L., BELHUMEUR P. N., KRIEGMAN D. J.: Image-based modeling and rendering of surfaces with arbitrary brdfs. In *Proceedings of 2001 IEEE Computer Society Conference on Computer Vision and Pattern Recognition (CVPR'01)* (2001), pp. pp. 568–575.
- [KS00] KUTULAKOS K. N., SEITZ S.: A theory of shape by space carving. *International Journal of Computer Vision Vol. 38*, No. 3 (2000), pp. 199–218.

- [KSK90] KLINKER G. J., SHAFER S. A., KANADE T.: A physical approach to color image understanding. *International Journal of Computer Vision* Vol. 4 (1990), pp. 7–38.
- [Lad] LADYBUG2, POINT GREY RESEARCH: <http://www.ptgrey.com>.
- [Lan77] LAND E.: The retinex theory of color vision. *Scientific American* Vol. 237, No. 6 (1977), pp. 108–128.
- [Lau94] LAURENTINI A.: The visual hull concept for silhouette-based image understanding. *IEEE Transactions on Pattern Analysis and Machine Intelligence* (February 1994), pp. 150–162.
- [Lee86] LEE H. C.: Method for computing the scene-illuminant from specular highlights. *Journal of Optics Society of America A*. Vol. 3, No. 10 (1986), pp. 1694–1699.
- [Lee90] LEE H.: Illuminant color from shading. In *Physics-based vision: Principles and practice, Color*. Jones and Bartlett Publishers, Inc., 1990, pp. pp. 340–347.
- [LH96] LEVOY M., HANRAHAN P.: Light field rendering. In *ACM Transactions on Graphics (Proceedings of ACM SIGGRAPH 1996)* (1996), pp. pp. 31–42.
- [LHS00] LENSCH H. P. A., HEIDRICH W., SEIDEL H. P.: Automated texture registration and stitching for real world models. In *Proceedings of Pacific Graphics* (2000), pp. pp. 317–326.
- [LL99] LIN S., LEE S. W.: Estimation of diffuse and specular appearance. In *Proceedings of IEEE International Conference on Computer Vision (ICCV '99)* (1999), vol. Vol. 2, pp. pp. 855–860.
- [LM71] LAND E. H., McCANN J. J.: Lightness and retinex theory. *Journal of Optics Society of America* Vol. 61, No. 1 (1971), pp. 1–11.
- [LMHK99] LENZ R., MEER P., HAUTA-KASARI M.: Spectral-based illumination estimation and color correction. *Color Research and Application* Vol. 24, No. 2 (April 1999), pp. 98–111.

- [MBR\*00] MATUSIK W., BUEHLER C., RASKAR R., GORTLER S. J., McMILLAN L.: Image-based visual hulls. In *Proceedings of the 27th annual conference on Computer graphics and interactive techniques* (2000), pp. pp. 369–374.
- [MNIS04] MATSUSHITA Y., NISHINO K., IKEUCHI K., SAKAUCHI M.: Illumination normalization with time-dependent intrinsic images for video surveillance. *IEEE Transactions on Pattern Analysis and Machine Intelligence Vol. 26*, No. 10 (2004), pp. 1336–1347.
- [MO00] MARCHANT J. A., ONYANGO C. M.: Shadow-invariant classification for scenes illuminated by daylight. *Journal of Optics Society of America A. Vol. 17*, No. 11 (2000), pp. 1952–1961.
- [MO01] MARCHANT J. A., ONYANGO C. M.: Color invariant for daylight changes: relaxing the constraints on illuminants. *Journal of Optics Society of America A. Vol. 18*, No. 11 (2001), pp. 2704–2706.
- [MO02] MARCHANT J. A., ONYANGO C. M.: Spectral invariance under daylight illumination changes. *Journal of Optics Society of America A. Vol. 19*, No. 5 (2002), pp. 840–848.
- [MW92] MALONEY L. T., WANDELL B. A.: Color constancy: a method for recovering surface spectral reflectance. In *Physics-based vision: Principles and practice, Color*. Jones and Bartlett Publishers, Inc., 1992, pp. pp. 219–223.
- [MYT03] MACHIDA T., YOKOYA N., TAKEMURA H.: Surface reflectance modeling of real objects with interreflections. In *Proceedings of IEEE International Conference on Computer Vision (ICCV '03)* (2003), vol. Vol. 1, pp. pp. 170–177.
- [NB93] NAYAR S. K., BOLLE R. M.: Reflectance ratio: A photometric invariant for object recognition. In *Proceedings of the IEEE International Conference on Computer Vision (ICCV'93)* (1993), pp. pp. 280–285.
- [NIK91] NAYAR S. K., IKEUCHI K., KANADE T.: Surface reflection: Physical and geometrical perspectives. *IEEE Transactions on Pattern Analysis and Machine Intelligence Vol. 13*, No. 7 (1991), pp. 611–634.

- [NK99] NEUGEBAUER P. J., KLEIN K.: Texturing 3d models of real world objects from multiple unregistrated photographic views. *Computer Graphics Forum Vol. 18*, No. 3 (1999), pp. 245–256.
- [NS92] NOVAK C. L., SHAFER S. A.: Supervised color constancy for machine vision. In *Physics-based vision: Principles and practice, Color*. Jones and Bartlett Publishers, Inc., 1992, pp. pp. 284–299.
- [NW63] NAYATANI Y., WYSZECKI G.: Color of daylight from north sky. *Journal of Optics Society of America Vol. 53*, No. 5 (1963), pp. 626–629.
- [NZI01] NISHINO K., ZHANG Z., IKEUCHI K.: Determining reflectance parameters and illumination distribution from a sparse set of images for view-dependent image synthesis. In *Proceedings of IEEE International Conference on Computer Vision (ICCV '01)* (2001), vol. Vol. 1, pp. pp. 599–606.
- [OH94] OHTA Y., HAYASHI Y.: Recovery of illuminant and surface colors from images based on the cie daylight. In *Proceedings of the Third European Conference on Computer Vision* (1994), pp. pp. 234–246.
- [ON51] OREN M., NAYAR S. K.: Generalization of the labertian model and implications for machine vision. *International Journal of Computer Vision Vol. 14*, No. 2 (1995), pp. 227–251.
- [PCD\*97] PULLI K., COHEN M., DUCHAMP T., HOPPE H., SHAPIRO L., STUETZLE W.: View-based rendering: Visualizing real objects from scanned range and color data. In *Proceedings of EUROGRAPHICS Workshop* (1997), pp. pp. 23–34.
- [PFTV88] PRESS W. H., FLANNERY B. P., TEUKOLSKY S. A., VETTERLING W. T.: *Numerical Recipes in C*. Cambridge University Press, 1988.
- [Rad] RADIANCE, SYNTHETIC IMAGING SYSTEM: <http://radsite.lbl.gov/radiance>.
- [RH02] RAMAMOORTHI R., HANRAHAN P.: Frequency space environment map rendering. *ACM Transactions on Graphics Vol. 21*, No. 3 (July 2002), pp. 517–526.
- [RHT01] ROSENBERG C., HEBERT M., THRUM S.: Color constancy using kl-divergence. In *Proceedings of the Eighth IEEE International Conference on Computer Vision (ICCV '01)* (2001), vol. Vol. 1, pp. pp. 239–246.

- [SD68] SASTURI V. D. P., DAS S. R.: Typical spectral distributions and color for tropical daylight. *Journal of Optics Society of America Vol. 58*, No. 3 (1968), pp. 391–398.
- [SD97] SEITZ S. M., DYER C. R.: Photorealistic scene reconstruction by voxel coloring. In *Proceedings of 1997 IEEE Computer Society Conference on Computer Vision and Pattern Recognition (CVPR'97)* (1997), pp. pp. 1067–1073.
- [Sec] SECOND LIFE: <http://secondlife.com>.
- [SOSI03] SATO I., OKABE T., SATO Y., IKEUCHI K.: Appearance sampling for obtaining a set of basis images for variable illumination. In *Proceedings of IEEE International Conference on Computer Vision (ICCV '03)* (2003), vol. Vol. 2, pp. pp. 800–807.
- [SSI99] SATO I., SATO Y., IKEUCHI K.: Acquiring a radiance distribution to superimpose virtual objects onto a real scene. *IEEE Transactions on Visualization and Computer Graphics Vol. 5*, No. 1 (1999), pp. 1–12.
- [SWI97] SATO Y., WHEELER M. D., IKEUCHI K.: Object shape and reflectance modeling from observation. In *ACM Transactions on Graphics (Proceedings of ACM SIGGRAPH 1997)* (1997), pp. pp. 379–387.
- [TEW01] TOMINAGA S., EBISUI S., WANDELL B. A.: Scene illuminant classification: brighter is better. *Journal of Optics Society of America A. Vol. 18*, No. 1 (2001), pp. 55–64.
- [TNI04] TAN R. T., NISHINO K., IKEUCHI K.: Color constancy through inverse intensity-chromaticity space. *Journal of Optics Society of America A. Vol. 21*, No. 3 (2004), pp. 321–334.
- [TNMM04] TAKAI T., NIIMURA K., MAKI A., MATSUYAMA T.: Difference sphere: An approach to near light source estimation. In *Proceedings of 2004 IEEE Computer Society Conference on Computer Vision and Pattern Recognition (CVPR'04)* (2004), vol. Vol. 1, pp. pp. 98–105.
- [Tsa86] TSAI R. Y.: An efficient and accurate camera calibration technique for 3d machine vision. In *Proceedings of 1986 IEEE Computer Society Conference on Computer Vision and Pattern Recognition (CVPR'86)* (1986), pp. pp. 364–374.

- [TW89a] TOMINAGA S., WANDELL B. A.: Component estimation of surface spectral reflectance. In *Physics-based vision: Principles and practice, Color*. Jones and Bartlett Publishers, Inc., 1989, pp. pp. 235–240.
- [TW89b] TOMINAGA S., WANDELL B. A.: Standard surface-reflectance model and illuminant estimation. *Journal of Optics Society of America A*. Vol. 6, No. 4 (1989), pp. 576–584.
- [TW02] TOMINAGA S., WANDELL B.: Natural scene-illuminant estimation using the sensor correlation. *Proceedings of the IEEE* Vol. 90, No. 1 (2002), pp. 42–56.
- [vdWGG07] VAN DE WEIJER J., GEVERS T., GIJSENIJ A.: Edge-based color constancy. *IEEE Transactions on Image Processing* Vol. 16, No. 9 (2007), pp. 2207–2214.
- [VFTB97] VORA P. L., FARRELL J. E., TIETZ J. D., BRAINARD D. H.: Digital color cameras - 2 - spectral response. *HP Technical Report* (1997).
- [WBKT66] WINCH G. T., BOSHOFF M. C., KOK C. J., TOIT A. G. D.: Spectroradiometric and colorimetric characteristics of daylight in the southern hemisphere : Pretoria, south africa. *Journal of Optics Society of America* Vol. 56, No. 4 (1966), pp. 456–464.
- [Wei01] WEISS Y.: Deriving intrinsic images from image sequences. In *Proceedings of IEEE International Conference on Computer Vision (ICCV '01)* (2001), vol. Vol. 2, pp. pp. 68–75.
- [WKSS01] WANG L., KANG S. B., SZELISKI R., SHUM H. Y.: Optimal texture map reconstruction from multiple views. In *Proceedings of 2001 IEEE Computer Society Conference on Computer Vision and Pattern Recognition (CVPR'01)* (2001), pp. pp. 347–354.
- [WMTG05] WINNEMOLLER H., MOHAN A., TUMBLIN J., GOOCH B.: Light waving: Estimating light positions from photographs alone. *Computer Graphics Forum* Vol. 24 (2005), pp. 433–438.
- [WS00] WYSZECKI G., STILES W. S.: *Color Science*. Wiley-Interscience Publication, JOHN WILEY & SONS, INC., 2000.

- [YM98] YU Y., MALIK J.: Recovering photometric properties of architectural scenes from photographs. In *ACM Transactions on Graphics (Proceedings of ACM SIGGRAPH 1998)* (1998), pp. pp. 207–218.
- [YXA07] YU T., XU N., AHUJA N.: Shape and view independent reflectance map from multiple views. *International Journal of Computer Vision Vol. 73* (2007), pp. 123–138.
- [ZBK02] ZICKLER T., BELHUMEUR P. N., KRIEGMAN D. J.: Helmholtz stereopsis: Exploiting reciprocity for surface reconstruction. *International Journal of Computer Vision Vol. 49, No. 2/3* (2002), pp. 215–227.



# List of Publications

## Book Chapter

1. Rei Kawakami, Robby T. Tan, Katsushi Ikeuchi, "Consistent Surface Color for Texturing Large Objects in Outdoor Scenes," *Digitally Archiving Cultural Objects*, K. Ikeuchi and D. Miyazaki (Eds), Springer, pp. 279-294, Jan, 2008.
2. Akifumi Ikari, Rei Kawakami, Robby T. Tan, Katsushi Ikeuchi, "Separating Illumination and Surface Spectral from Multiple Color Signals," *Digitally Archiving Cultural Objects*, K. Ikeuchi and D. Miyazaki (Eds), Springer, pp. 297-319, Jan, 2008.

## Journal Papers

1. Rei Kawakami, Jun Takamatsu, Katsushi Ikeuchi, "Color Constancy from Black-body Illumination," *Journal of Optics Society of America A*. (JOSA A.), Vol. 24, No. 7, pp. 1886-1893, July, 2007

## International Conferences

1. Rei Kawakami, Katsushi Ikeuchi, "Stabilizing Illumination Chromaticity Estimation using the Illumination Line Segment," *In the Proceeding of the Tenth IAPR Conference on Machine Vision Applications (MVA2007)*, pp.437-440, Tokyo, Japan, May, 2007
2. Daisuke Miyazaki, Mawo Kamakura, Tomoaki Higo, Yasuhide Okamoto, Rei Kawakami, Takaaki Shiratori, Akifumi Ikari, Shintaro Ono, Yoshihiro Sato, Mina Oya, Masayuki Tanaka, Katsushi Ikeuchi, Masanori Aoyagi, "3D Digital Archive of the Burghers of Calais," *In the Proceedings of the International Conference on Virtual Systems and Multimedia (VSMM2006)*, Lecture Notes in Computer Science (LNCS), 2006. 10
3. Rei Kawakami, Robby T. Tan, Katsushi Ikeuchi, "Consistent Surface Color for Texturing Large Objects in Outdoor Scenes," *In Proceedings of the Tenth IEEE International Conference on Computer Vision (ICCV2005)*, Vol. 2, pp. 1200-1207, Beijing, China, 2005

4. Rei Kawakami, Robby T. Tan, Katsushi Ikeuchi, "A Robust Framework to Estimate Surface Color From Changing Illumination," *In Proceedings of the Sixth Asian Conference on Computer Vision (ACCV2004)*, Vol. 2, pp. 1026-1031, Jeju, Korea, Jan. 2004

## Domestic Conferences

1. 川上玲, 池内克史, "光源線分による光源色推定の安定化", 画像の認識・理解シンポジウム (MIRU2007) 論文集ダイジェスト, August, 2007
2. 川上玲, 高松淳, 池内克史, "黒体放射の光源制約を用いた色恒常性", 画像の認識・理解シンポジウム (MIRU2006), 論文集ダイジェスト, pp.309-314, 仙台, July, 2006
3. 川上玲, R.T.Tan, 池内克史, "光源色の違いを利用したロバストな物体色推定", 画像の認識・理解シンポジウム (MIRU2005) 論文集, pp.228-234, 淡路島, July, 2005
4. 川上玲, R.T.Tan, 池内克史, "光源環境の変化を利用した物体色の推定", 画像の認識・理解シンポジウム (MIRU2004) 論文集ダイジェスト, pp.169-174, 函館, July, 2004

## Workshops

1. S. Okura, R. Kawakami, K. Ikeuchi, "Simple Surface Reflectance Estimation of Diffuse Outdoor Object using Spherical Images", *In 8th Asian Conference on Computer Vision, Workshop on Multi-dimensional and Multi-view Image Processing*, Tokyo, Japan, Nov. 2007
2. 川上玲, 高松淳, 池内克史, "黒体放射の仮定を用いた光源制約による色恒常性", 情報処理学会 コンピュータビジョンとイメージメディア研究会 (CVIM 研究会) May, 2006
3. R. Kawakami, K. Ikeuchi, "A Framework to Estimate Consistent Surface Color for Large Scale Outdoor Heritages" *In the Proceeding of International Symposium on the CREST Digital Archiving Project*, pp.100-106, Tokyo, Japan, March, 2005
4. 川上玲, R.T.Tan, 池内克史, "文化遺産のデジタル保存のための光源色の変化を用いた物体表面色推定手法", 第 70 回 3 次元フォーラム (3D Forum 2004) Vol.18, No.4, pp.23-26, 東京, Dec, 2004